OUKA
Osaka University Knowledge Archive

Title	Studies on Miniaturization of Power Converters Using Gallium Compound Semiconductor Power Devices
Author(s)	關, 翔太
Citation	大阪大学, 2024, 博士論文
Version Type	VoR
URL	https://doi.org/10.18910/98761
rights	
Note	

Osaka University Knowledge Archive : OUKA

https://ir.library.osaka-u.ac.jp/

Osaka University

Doctoral Dissertation

Studies on Miniaturization of Power Converters Using Gallium Compound Semiconductor Power Devices

Shota Seki

June, 2024

Division of Electrical, Electronic
and Infocommunications Engineering

Graduate School of Engineering

Osaka University

Abstract

The development of wide bandgap power semiconductor devices has enabled the miniaturization of power conversion circuits. In particular, the implementation of GaN power semiconductor devices has made it possible to significantly increase the operating frequency of power conversion circuits. GaN HEMTs are switching devices that use two-dimensional electron gas to achieve high electron mobility and to enable fast switching. However, GaN SBDs with good characteristics are difficult to obtain. Ga_2O_3 SBDs are expected as alternative to GaN as a fast switching diodes. By applying gallium compound power semiconductors, GaN and Ga_2O_3, it is possible to realize power conversion circuits that are smaller and higher efficiency than conventional ones.

The objective of this study is to develop miniaturization technology for power conversion circuits using gallium compound power semiconductors. Power conversion circuits using gallium compound power semiconductors can operate at frequencies above 10 MHz. This thesis discusses the factors required for power conversion circuits above 10 MHz with gallium compound power semiconductors. Since magnetic components have a significant impact on the operation of high-frequency power conversion circuits, this thesis develops a method to evaluate the characteristics of magnetic components. In addition, the thermal conductivity of gallium compound power semiconductors is lower than that of Si, and the parasitic capacitance of semiconductor devices differs from that of Si. This thesis evaluates the thermal characteristics and models the voltage dependency of parasitic capacitance in gallium compound power semiconductor devices. The equivalent circuit model of magnetic components and the voltage dependency of capacitance model are validated using actual circuits of class-E amplifiers.

This thesis consists of the following six chapters. Chapter 1 is the introduction. Chapter 1 introduces the background and objectives of this study. This chapter de-

scribes the problems preventing the miniaturization of power conversion circuit using gallium compound power semiconductors.

Chapter 2 describes the physical properties of gallium compound power semiconductors, including the structure and properties of GaN HEMTs. Chapter 2 also describes the physical properties and SBD structures of Ga_2O_3.

Chapter 3 evaluates magnetic components applied to a class-E amplifiers using GaN HEMTs. A method for evaluating magnetic characteristics using a 2-port circuit model and a vector network analyzer is developed. An equivalent circuit model of an inductor is proposed based on the 2-port model. The model is verified through circuit simulations and experiments of class-E amplifiers.

Chapter 4 evaluates transient thermal characteristics of Ga_2O_3 SBDs. The forward current characteristics of diodes are used to evaluate the thermal characteristics of power semiconductor devices. However, the ideality of Ga_2O_3 devices is not certified. In this thesis, the quality of Ga_2O_3 Schottky junctions is evaluated based on measured static characteristics. Transient thermal characteristics of Ga_2O_3 SBDs are also evaluated. In addition, a method to reduce transient thermal resistance by grinding the substrate layer of SBDs is discussed.

Chapter 5 models the voltage dependency of the parasitic capacitance for GaN HEMTs using a sigmoid function. Using the sigmoid function model, a circuit analysis of a class-E amplifier is performed to derive the soft-switching conditions. The derived soft-switching condition is verified by circuit simulation and experiment for actual circuits.

Chapter 6 concludes this thesis. This chapter also discusses the industrial impact and future prospects of this study.

Acknowledgement

First of all I would like to express my most gratitude to Professor Tsuyoshi Funaki at Division of Electrical, Electronic and Infocommunications Engineering, Graduate School of Engineering, Osaka University. This work would not be accomplished without his constant support and prominent wisdom. He conferred invaluable and magnificent insight through discussions.

I would like to acknowledge Professor Tomoo Ushio and Professor Shigemasa Takai at Division of Electrical, Electronic and Infocommunications Engineering, Graduate School of Engineering, Osaka University for their careful review and attentive suggestions on this thesis. I also would like to appreciate Professor Masahide Hojo at Department of Electrical and Electronic Engineering, Graduate School of Technology, Industrial and Social Science, Tokushima University for his careful review and attentive suggestions.

I sincerely thank Professor Hideharu Sugihara at Program of Electrical and Electronic Engineering, School of Engineering, Kwansei Gakuin University, Lecturer Takaaki Ibuchi and Assistant Professor Shuhei Fukunaga at Division of Electrical, Electronic and Infocommunications Engineering, Graduate School of Engineering, Osaka University for a lot of their valuable advices and precise suggestions. I also thank Appointed Professor Takashi Nakamura and Guest Professor Shigekazu Sakabe at Division of Electrical, Electronic and Infocommunications Engineering, Graduate School of Engineering, Osaka University for their precious opinions.

I would like to thank Mr. Jun Arima, Mr. Minoru Fujita, Mr. Jun Hirabayashi, and Mr. Kazuyoshi Hanabusa at TDK Corporation for their enthusiastic and polite corporation in the joint research.

I would like to express great appreciation to all members of Funaki Laboratory for

their support and cooperation. I am deeply grateful to Mr. Hiroshi Kinemura for kind instruction and valuable discussion. I specially thank Ms. Fumie Imura secretary in Funaki Laboratory for her kind support to my daily work. I would like to thank my doctoral colleagues Mr. Yuki Nomura and Mr. Kazuki Nishatani for their cooperation.

I would like to express great appreciation to all colleagues of ROHM Corporation for their understanding and supports. I am deeply grateful to Mr. Satoru Nate, Mr. Satoshi Maejima, and Mr. Takumi Fujimaki for their thoughtful cooperations.

This work was partially supported by Waseda University Graduate Program for Power Energy Professionals (PEP). This work was partially supported by Osaka University Support for Pioneering Research Initiated by the Next Generation Project. This work has been partially implemented under a joint research project with TDK Corporation.

Finally, I deeply thank my parents, brothers and friends of mine for their understanding, careful supports, and constant encouragement.

Shota SEKI

Osaka, June 2024

Contents

Chapter 1

Introduction

1.1 Background

Power electronics is the key to solve social problems[1]. There is vigorous controversy on improving the sustainability of human society. Reducing consumption of fossil fuels is one of the urgent problems[2][3]. Fossil fuels lead to global warming and economic disparity between oil-producing and non-oil-producing countries. To reduce fossil fuel consumption, electrification of internal combustion engines and the use of renewable energy sources are necessary[4].

The development of power electronics is essential for these electrification and utilization of renewable energy. Semiconductor power conversion technology has been used in power converters and motor drive circuits, which results in significant improvements in efficiency and controllability. These semiconductor power conversion circuits have mainly used silicon (Si) semiconductors. Low-voltage circuits adopt Si metal oxide semiconductor field effect transistors (MOSFETs) as switches and Si Schottky burrier diodes (SBDs) as rectifiers. High-voltage circuits adopt Si insulated gate bipolar transistors (IGBTs) and Si gate turn-off thyristors (GTOs) as switches. PN diodes and PiN diodes are used as rectifiers[5][6].

Semiconductor power conversion circuits are required to achieve both high power density and high efficiency. Power density is the ratio between volume of the converter to converted power. The small converters which handles large amount of power is required. Increase in operating frequency is effective to reduce the size of power con-

version circuits. By increasing the operating frequency, the inductance and capacitance required for circuit operation can be reduced[7]. This is because the higher operating frequency reduces the amount of energy handled by passive components per cycle.

However, There are some drawback to the higher operating frequency. Power dissipations in power devices can be divided into conduction loss and switching loss. Conduction loss is the product of the current flowing through the power device and the voltage applied during the conduction state. Conduction loss is determined by the characteristics of the power device and amount of flowing current.

Semiconductor power devices require time for the transition between the on-state and off-state. The transient time causes the power device's simultaneous current and voltage application. The losses in the transient time of power devices are called switching loss. Since the switching transition time is a parameter independent of the switching frequency, the switching loss increases proportionally as the operating frequency increases. From the above, the higher power and higher operating frequency increases the losses consumed in the switches.

In order to reduce losses in switches as well as to achieve both miniaturization and high efficiency, faster switching and low on-resistance of power semiconductor devices are needed. Unipolar devices have an advantage for fast switching because they use only majority carrier for conduction. However, unipolar devices have a trade-off between breakdown voltage and on-resistance. Si power semiconductor devices are reaching their performance limit for improving this trade-off[1][8].

Studies on wide bandgap semiconductors such as SiC and GaN are undergoing as semiconductor materials that exceed the performance limits of Si power semiconductor devices. SiC and GaN have wider bandgap than Si, which enables semiconductor device operation at high temperature. Also, the critical electric field strength of wide bandgap semiconductors is higher than that of Si, which can achieve both higher breakdown voltage and lower on-resistance [9][10].

Table 1.1 shows the physical properties of semiconductor materials. Wide bandgap semiconductors have wider bandgap and higher critical electric field strength compared to Si. This feature enables unipolar devices to have high Baliga's Figure-Of-Merits (BFOM), which indicates the trade-off performance between breakdown voltage and

Table 1.1 Physical properties of semiconductor materials[11]-[26]

		Si	4H-SiC	GaN	α-Ga_2O_3	β-Ga_2O_3
Bandgap	E_g (eV)	1.1	3.3	3.4	5.3	4.5-4.9
Critical electric field	E_{crt} (MV/cm)	0.23	2.2	3.3	9.5	8.0
Electron mobility	μ_e (cm^2/V·s)	1450	1000	900	200(est.)	150
Relative permittivity	ϵ	11.9	12.8	10.4	10(est.)	10.2
Thermal conductivity	λ (W/cm·K)	1.5	2.8	1.5	0.09[010] 0.12 [100]	0.13 [010] 0.21 [100]
BFOM	$\epsilon\mu_e {E_g}^3$	1	500	900	3844	3444

on-resistance[27].

SiC power semiconductor devices enable high-speed switching by replacing Si IGBTs with SiC MOSFETs and Si PiN diodes with SiC SBDs in high-voltage, high-current applications. The SiC manufacturing technologies have already reached the commercial level. SiC applications have been implemented in society, for example, in the motor drive system of the Shinkansen high-speed train[28][29].

GaN semiconductor has bandgap almost same as that of SiC. However, GaN is difficult to fabricate as a single crystal. GaN crystals are grown on other materials such as Si, SiC, and sapphire. Currently used commercially available GaN devices are lateral structure power semiconductor devices. Compared to vertical structure devices, lateral devices have lower current capability. On the other hand, the piezoelectric polarization and the spontaneous polarization caused by the boundary of an Al-GaN layer and a GaN layer generates two-dimensional electron gas (2DEG) in lateral structure GaN devices. Two-dimensional electron gas has high mobility and enables power semiconductor device to switch at fast. This feature makes GaN power devices suitable for low-power and compact power conversion circuits[10][11][12][30] and RF power converters[31]-[33].

There are many preceding research on power conversion circuits using GaN power devices. For example, 1 MHz driven power converters have achieved efficiencies of up to 98% or more at around 1kW output power[34][35]. In the MHz band, there are many reports of converters of 100 W or less, with efficiencies of around 90% at best[36][37]. In

addition, converters from tens to 100 MHz have been reported[38][39][40]. These have output powers from a few Watt to several tens-of-Watt. Some use soft-switching and have efficiencies in excess of 90%[41][42]. However, the driving frequency of commercial converters, such as VIPerGaN (STmicro) and EPC9171 (EPC), is 1 MHz or less. This is due to limitations imposed by the magnetic components and thermal characteristics.

Gallium oxide (Ga_2O_3) semiconductors have wider bandgap than SiC and GaN[43]-[46]. Ga_2O_3 also has multiple polymorphs. Among them, α and β Ga_2O_3 is expected as materials for power semiconductor devices[13]-[18]. Especially, β-Ga_2O_3 can be grown from its melt under atmospheric pressure, which is suitable for mass-production[47]-[49]. For this reason, β-Ga_2O_3 is expected to be used as inexpensive, high-voltage, low on-resistance power devices. Because fabrication of GaN SBD is difficult, the combination of GaN semiconductor switching device and SiC or Ga_2O_3 SBDs is expected to realize power conversion circuits that can operate at fast and high frequency[50].

β-Ga_2O_3 power devices are currently in the research and development stage. β-Ga_2O_3 power devices with various structures have been proposed. Generally, it is difficult to dope p-type impurities into Ga_2O_3[51]. Then, n-type SBDs are mainly developed[15][18]. As switching devices, lateral FETs have been developed first[26]. In recent years, vertical FETs, which are suitable for high current, have also been reported[44][52].

1.2 Problems in miniaturization of power converters using gallium compound power semiconductor devices

Although gallium compound power semiconductor devices such as GaN and Ga_2O_3 power semiconductor devices are actively developed, there are many challenges in miniaturization of power conversion circuits using gallium compound power semiconductor devices. This section discusses the problems in miniaturization of power converters using gallium compound power semiconductor devices.

1.2.1 Problems in magnetic components for high frequency power conversion

GaN power semiconductor devices are capable of high-speed switching and high-frequency operation. Despite of high performance of GaN power devices, magnetic components such as inductors are the bottleneck of miniaturization of whole circuits. Magnetic components with air cores do not cause magnetic saturation and do not generate iron loss[53][54]. They can be used in high-frequency converters. On the contrary, air-core inductors tend to be large in volume. In addition, EMI effects are serious due to high leakage magnetic flux[55]. Magnetic components with magnetic cores are desirable for power conversion circuits[37][56][57].

Losses in magnetic components are divided into iron loss and copper loss, which increase as the operating frequency increases. And, iron loss is divided into hysteresis loss and eddy current loss. To reduce these losses, it is effective to reduce area of the magnetic domain and the loop of eddy currents. Magnetic components for high-frequency power conversion are realized by miniaturized magnetic domains and eddy current paths with solidified finely processed magnetic materials[58]-[61].

Those low-loss magnetic components have low permeability due to microscopic gaps in the magnetic path. While such magnetic components can reduce losses, low permeability increases the size of magnetic components to realize enough inductance for circuit operation. Design of magnetic components is important to achieve both low loss at high switching frequency and miniaturization. Evaluation of magnetic material properties is essential for the design of high-frequency magnetic components[62].

However, it is difficult to evaluate the characteristics of low-permeability magnetic components because of inability in accurate measurement of current and phase difference between voltage and current. There is a need to evaluate the characteristics of inductors used in high-frequency power conversion circuits.

1.2.2 Problems in heat dissipation of gallium compound power semiconductor devices

In addition to magnetic components, power semiconductor devices also have problems for miniaturization of power conversion circuits. High-frequency operation of power conversion circuits increases switching losses. However, it is difficult to dissipate heat sufficiently in circuits with a small volume. In addition, the thermal conductivity of GaN is almost the same as that of Si[12]. The thermal conductivity of Ga_2O_3 is much lower than that of Si[19]-[21].

Improving heat dissipation performance is particularly important for the practical application of Ga_2O_3 power semiconductor devices. However, there are few studies in evaluation of thermal characteristics of Ga_2O_3 power semiconductor devices. It is necessary to develop device structures for reducing the thermal resistance of Ga_2O_3 power semiconductor devices[63].

1.2.3 Problems in consideration of output capacitance for soft-switching

Soft-switching technique is used to reduce switching losses. Soft-switching uses resonance to prevent switching losses at switching transition. In soft-switching circuits, capacitors are connected in parallel with the switching devices to form a resonant circuit[64]-[72].

FETs have parasitic capacitance between drain and source, which is called output capacitance. Output capacitance in FETs has voltage dependency. Voltage dependency of output capacitance makes the resonant circuit nonlinear and time-variant. Circuit design must consider the voltage dependency of output capacitance to achieve soft-switching[73]-[79].

GaN high electron mobility transistors (HEMTs) used as switching devices are lateral structure. The parasitic capacitance characteristics of the lateral structure devices differ from those of vertical structure devices. For this reason, the parasitic capacitance of GaN HEMTs cannot be represented by the vertical type Si MOSFET model[80]-[83]. The dedicated model of voltage dependency in GaN output capacitance

is needed for soft-switching analysis.

1.3 Purpose and outline of this thesis

This thesis investigates the technologies to miniaturize power conversion circuits using gallium compound power semiconductor devices. This thesis focuses on magnetic components and semiconductor devices in power conversion circuits operating at frequencies above MHz. In addition, this thesis fabricates power conversion circuit that operates at operating frequencies 10 MHz or higher and verifies the validity of the proposed consideration.

Chapter 2 describes device structures of gallium compound semiconductor devices, GaN and Ga_2O_3. Based on the characteristics of GaN and Ga_2O_3 semiconductor devices, issues for miniaturization of power conversion circuits are also discussed.

Chapter 3 models magnetic components made of iron-based metal composite materials and carbonyl iron materials. Those materials are developed as magnetic components for high-frequency power conversion circuits. This chapter evaluates the losses of the two materials and proposes an equivalent circuit model that can be used for circuit analysis and simulation. The identification of parameters in the proposed equivalent circuit model is described. The identified parameters are validated by circuit simulations and experiments on class-E amplifiers.

Chapter 4 describes a method for evaluating device electrical and transient thermal characteristics of β-Ga_2O_3 power Schottky barrier diodes. The temperature dependency of the diode's forward current characteristics is used to estimate transient thermal resistance. β-Ga_2O_3 is still in the development stage and its crystal has many defects. In this chapter, the possibility of measuring transient thermal resistance is discussed based on the evaluation of the ideal factor of diodes and other properties of β-Ga_2O_3 SBDs. In addition, a method of thinning the substrate layer in the diode is discussed to reduce the thermal resistance of β-Ga_2O_3 SBDs to conquer low thermal conductivity.

Chapter 5 proposes to model the voltage dependency of the output capacitance in GaN power devices using sigmoid function for the circuit analysis of a class-E amplifier.

This chapter derives the conditions for class-E switching with sigmoid function modeled output capacitance of GaN power devices. The results obtained by circuit analysis are verified by simulations and circuit experiments operated above 10 MHz operating frequencies.

Chapter 6 summarizes this thesis and discusses the industrial impact and future prospects of this work.

Chapter 2

Gallium compound semiconductor devices

2.1 Introduction

Wide bandgap power semiconductors are being studied as an alternative to Si semiconductors. This thesis focuses on gallium compound power semiconductor devices. Gallium compound power semiconductor devices have wider bandgap and higher critical electric field strength than Si. However, Gallium compound semiconductors have some problems such as difficulty in fabricating single crystals. To overcome the physical problems and take advantage of the excellent physical properties for semiconductor materials, various device structures are being investigated.

In this chapter, the physical properties of gallium compound semiconductor devices are explained based on semiconductor physics. Then, device structures specified to gallium compound power semiconductors are described. In this thesis, GaN and β-Ga_2O_3 are treated as gallium compound power semiconductor devices. This chapter explains the structures of GaN HEMTs and β-Ga_2O_3 SBDs in detail.

2.2 Physical properties of semiconductor devices

Semiconductors are materials with properties intermediate between those of conductors and insulators. The energy band structures of conductor, semiconductor, and insulator

crystals are shown in Fig. 2.1. ε_G is bandgap and ε_F is Fermi level[11][27][84][85].

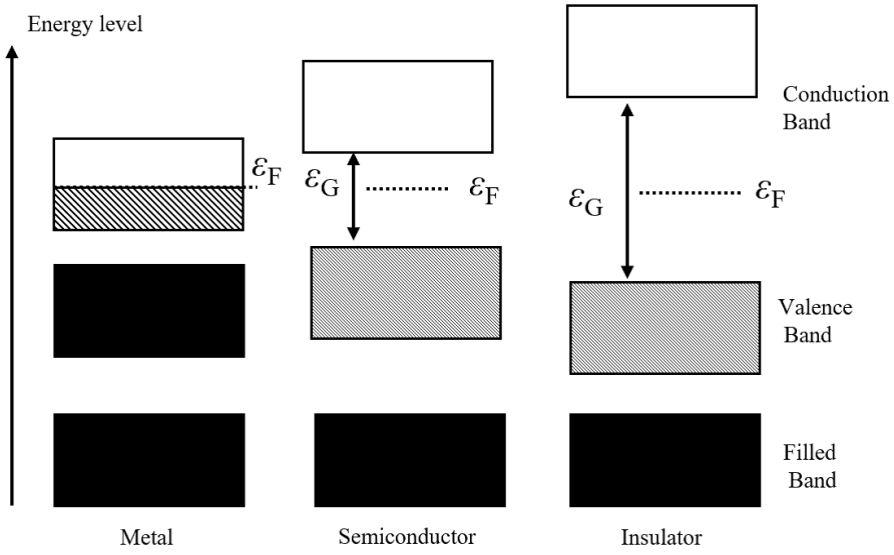

Figure 2.1 Energy bands of conductor, semiconductor, and insulator.

In crystals, the energy of electrons is discrete value. This value is called the energy level. In the case of crystals, there are many electrons with discrete energy levels. The energy level differences among electrons becomes very small, so that each level forms a continuous band. This continuous level is called an energy band. The energy level is divided into an allowed band, in which electrons are allowed to exist, and a forbidden band, in which they are not allowed to exist. In a crystal, electrons are trapped in order from the lowest energy level to the highest. The allowed band in which electrons are completely occupied is called the filled band. The highest energy level in the filled band is called the valence band.

When an electric field is applied to a crystal, electrons receive energy from the electric field and transit to higher energy level. However, all the levels in the filled band are occupied by electrons. Then, the electrons in the filled band cannot transit to another level due to the energy from the electric field. Therefore, electrons in the filled band cannot contribute to electrical conduction.

An empty or partially occupied allowed band is called conduction band. The conduction band is an allowed band just above the valence band. Because the conduction band is vacant, electrons in the conduction band can receive energy from the electric field and transit to another level. The transited electrons contribute to electrical con-

duction. Such electrons are called free electrons. In the case of metals, electrons are occupied up to the middle of the conduction band. The free electrons in the conductor contribute to electrical conduction, which results in very high conductivity. In the case of insulators, electrons are occupied up to the valence band. There are almost no electrons in the conduction band, thus the conductivity is very low.

In semiconductors, electrons occupy the valence band. However, because the forbidden bandgap ε_G, which is the energy difference between the valence band and the conduction band, is relatively low. The transition of electrons from the valence band to the conduction band is possible. Thus, there are a few free electrons in conduction band of semiconductors. In the valence band of semiconductors, an empty level is left after the transition of electrons. This level can be regarded as a positive charge. Electrons can easily transit to this empty level. The left energy level becomes an empty level again. As this process continues, the empty level can be regarded as conductor. This empty level is called hole. In semiconductors, both free electrons and holes contribute to electrical conduction. Electrons and holes are called carriers.

The electron energy ε_e is expressed as Eq. 2.1, where m_e, ε_c, $\hbar$, and k are effective mass of electron, bottom energy of conduction band, Planck constant, and wavenumber of wave function, respectively.

$$\varepsilon_e = \varepsilon_c + \frac{\hbar^2 k^2}{2m_e} \tag{2.1}$$

The electron energy ε_h is expressed as Eq. 2.2, where m_h and ε_v are effective mass of hole and bottom energy of valence band, respectively.

$$\varepsilon_h = \varepsilon_v - \frac{\hbar^2 k^2}{2m_h} \tag{2.2}$$

Bandgap ε_G is expressed as Eq. 2.3 using ε_c and ε_v.

$$\varepsilon_G = \varepsilon_c - \varepsilon_v \tag{2.3}$$

The bandgap depends on the semiconductor materials. The electrical properties of semiconductors depend on the value of the bandgap.

Electron density of states $g_n(\varepsilon)d\varepsilon$ between valence band and conduction band is a function of ε_e as shown in Eq. 2.4. Hole density of states ε_e between valence band and conduction band is a function of ε_h as shown in Eq. 2.5.

$$g_n(\varepsilon_e)d\varepsilon_e = \frac{(2m_e)^{3/2}}{2\pi^2\hbar^3}\sqrt{\varepsilon_e - \varepsilon_c}d\varepsilon_e \tag{2.4}$$

$$g_p(\varepsilon_h)d\varepsilon_h = \frac{(2m_h)^{3/2}}{2\pi^2\hbar^3}\sqrt{\varepsilon_v - \varepsilon_h}d\varepsilon_h \tag{2.5}$$

From Fermi-Dirac statistics, probability of electron occupation $f_n(\varepsilon_e)$ and probability of hole occupation $f_p(\varepsilon_h)$ are expressed as Eq. 2.6 and Eq. 2.7, respectively, where k_B is Boltzmann constant and T is absolute temperature.

$$f_n(\varepsilon_e) = \frac{1}{e^{(\varepsilon_e - \varepsilon_F)k_BT} + 1} \tag{2.6}$$

$$f_p(\varepsilon_h) = 1 - f_n(\varepsilon_e) \tag{2.7}$$

Density of electron n and density of hole p is expressed as Eq. 2.8 and Eq. 2.9 using Eq. 2.6 and Eq. 2.7.

$$n = \int_{\varepsilon_c}^{\infty} g_n(\varepsilon_e)f_n(\varepsilon_e)d\varepsilon_e = \frac{(2m_e)^{3/2}}{2\pi^2\hbar^3}\int_{\varepsilon_c}^{\infty}\frac{(\varepsilon_e - \varepsilon_c)^{1/2}}{1 + e^{(\varepsilon_e - \varepsilon_F)/k_BT}} \tag{2.8}$$

$$p = \int_{-\infty}^{\varepsilon_v} g_p(\varepsilon_h)f_p(\varepsilon_h)d\varepsilon_h = \frac{(2m_h)^{3/2}}{2\pi^2\hbar^3}\int_{-\infty}^{\varepsilon_v}\frac{(\varepsilon_v - \varepsilon_h)^{1/2}}{1 + e^{(\varepsilon_F - \varepsilon_h)/k_BT}} \tag{2.9}$$

In intrinsic semiconductors, the Fermi level ε_F is in the middle of forbidden band, and $f_n(\varepsilon_e) \ll 1$, $f_p(\varepsilon_h) \ll 1$. Thus, Eq. 2.8 and Eq. 2.9 can be approximated by the Boltzmann distribution. Using Boltzmann distribution, Eq. 2.8 and Eq. 2.9 are expressed as Eq. 2.10 and Eq. 2.11.

$$n = N_c \exp\left(-\frac{\varepsilon_c - \varepsilon_F}{k_BT}\right) \approx N_c f_n(\varepsilon_c) \tag{2.10}$$

$$p = N_v \exp\left(-\frac{\varepsilon_F - \varepsilon_v}{k_BT}\right) \approx N_v f_p(\varepsilon_v) \tag{2.11}$$

N_c in Eq. 2.10 is called conduction band effective density of states and expressed as Eq. 2.12. N_v in Eq. 2.11 is called valence band effective density of states and expressed as Eq. 2.13.

$$N_c = 2\left(\frac{2\pi m_e k_BT}{h^2}\right)^{3/2} \tag{2.12}$$

$$N_v = 2\left(\frac{2\pi m_h k_BT}{h^2}\right)^{3/2} \tag{2.13}$$

The product of Eq. 2.10 and Eq. 2.11 is Eq. 2.14.

$$np = N_c N_v \exp\left(-\frac{\varepsilon_c - \varepsilon_v}{k_BT}\right) = N_c N_v \exp\left(-\frac{\varepsilon_G}{k_BT}\right) \tag{2.14}$$

In intrinsic semiconductor, the number of free electrons and that of holes are equal. Then, the electroneutrality condition $n = p = n_i$ is satisfied. Electron density n_i is expressed as Eq. 2.15.

$$n_i = \sqrt{N_c N_v} \exp\left(-\frac{\varepsilon_G}{2k_B T}\right) = 2\left(\frac{2\pi k_B T}{h^2}\right)^{3/2} (m_e m_h)^{3/4} \exp\left(-\frac{\varepsilon_G}{2k_B T}\right) \tag{2.15}$$

Fermi level ε_F is expressed as Eq. 2.16.

$$\varepsilon_F = \frac{\varepsilon_c + \varepsilon_v}{2} + \frac{k_B T}{2} \log\left(\frac{N_v}{N_c}\right) = \frac{\varepsilon_c + \varepsilon_v}{2} + \frac{3k_B T}{4} \log\left(\frac{m_h}{m_e}\right) \tag{2.16}$$

In Eq. 2.16, the first term in the right hand side is sufficiently large compared to the second term. Hence, the Fermi level in a intrinsic semiconductor is approximately at the center of the forbidden band.

From Eq. 2.14, the product of electron density and hole density is a function of temperature T, providing that m_e, m_h and ε_G are given. As temperature increases, the product of electron density and hole density increases exponentially, which indicates that the electrical conductivity increases. This makes it difficult for power semiconductor devices to operate as designed in high temperature. Therefore, the upper limit of the operating temperature for power semiconductor devices depends on the bandgap.

Notably, unipolar devices use the impurity doped layer called the drift layer to ensure breakdown voltage V_B. The on-resistance of ideal drift region R_{on} is expressed as Eq. 2.17, where e is electron elementary charge and μ_e is electron mobility. W_D and N_D are depletion width and doping concentration, respectively.

$$R_{on} = \frac{W_D}{e\mu_e N_D} \tag{2.17}$$

W_D in Eq. 2.17 is expressed as Eq. 2.18 using V_B and critical electric field strength E_c.

$$W_D = \frac{2V_B}{E_c} \tag{2.18}$$

The doping concentration N_D is expressed as Eq. 2.19, where ϵ_s is permittivity.

$$N_D = \frac{\epsilon_s E_c^2}{2eV_B} \tag{2.19}$$

Combing Eq. 2.17 to Eq. 2.19, R_{on} is expressed as Eq. 2.20, where ϵ_s, μ_e, and E_c are material specific values.

$$R_{on} = \frac{4V_B^2}{\epsilon_s \mu_e E_c^3} \tag{2.20}$$

However, there are little differences in ϵ_s between materials as shown in Table 1.1. E_c has a greater impact than μ_e because cubic of E_c is in denominator of Eq. 2.20. The wider E_c gives the better trade-off between on-resistance and breakdown voltage. E_c correlates with bandgap width.

As described above, wide bandgap allows for high temperature operation and improves the trade-off between on-resistance and blocking voltage in unipolar device. Gallium compound power semiconductor devices have wide bandgap and high critical electric field strength, which is expected to improve performance.

2.3 GaN power semiconductor devices

GaN has superior properties due to its wide bandgap and high critical electric field strength as shown in Table 1.1. The majority of GaN power devices currently being investigated are high electron mobility transistor (HEMT) structures using two-dimensional electron gas (2DEG). Figure 2.2 shows the structure of typical normally-on GaN HEMT.

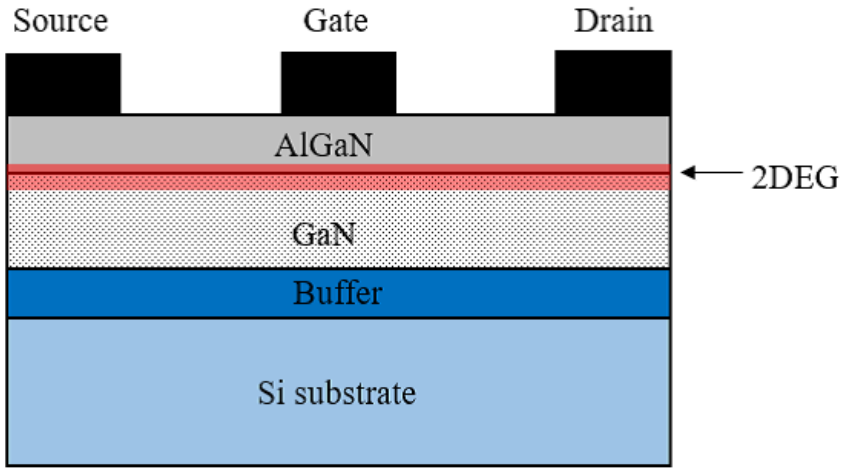

Figure 2.2 Structure of normally-on GaN HEMT.

GaN HEMTs have heterojunctions of GaN and AlGaN in their internal structure. Spontaneous polarization occurs at the interface due to the different lattice constant of GaN and AlGaN. Besides, AlGaN has strain in the layer, which causes piezoelectric

polarization. The sum of those polarization generates 2DEG at the heterojunction boundary, which has very high saturation mobility, resulting in fast switching, and low on-resistance. Heterojunction polarization occurs even when the gate voltage is zero. Therefore, the GaN HEMT in the figure has normally-on characteristics[86].

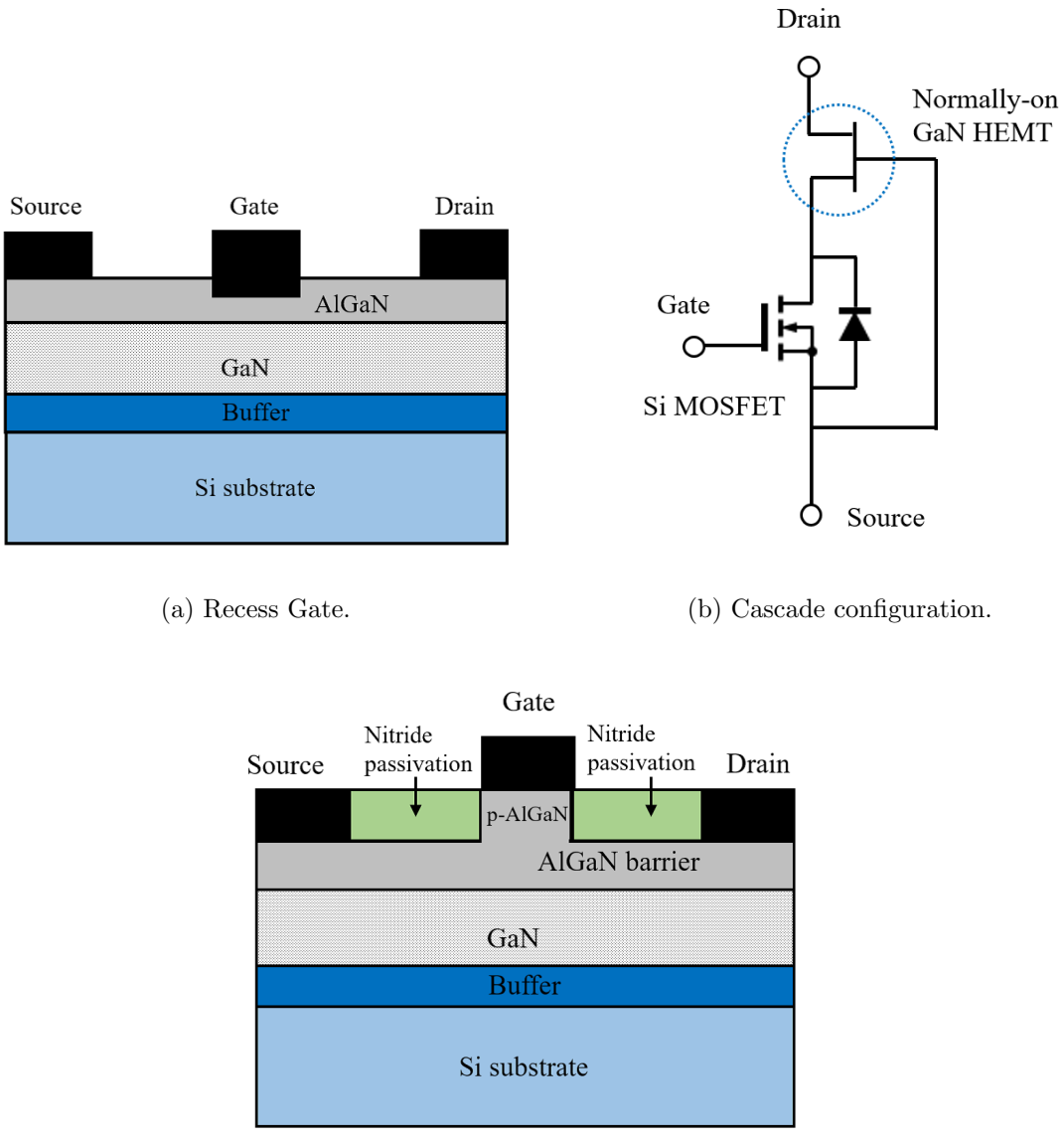

(a) Recess Gate.

(b) Cascade configuration.

(c) *p*-type gate.

Figure 2.3 Structure and configuration of normally-off GaN HEMT.

In the normally-on characteristic, a failure of the peripheral circuit causes short circuit between the drain and source of the power device, which results in high current

flow. Several structures have been proposed to make GaN power semiconductor devices with normally-off characteristics. Figure 2.3 shows several examples of GaN structures with normally-off characteristics[87][88].

Figure 2.3(a) is called recess gate structure. Recess gates can achieve normally-off without increasing on-resistance. On the other hand, the fabrication process requires the plasma-etching. It is difficult to control the depth of gate recess with plasma etching. The ion bombardment of etching plasma causes damage of power device.

Figure 2.3(b) is called cascade connection. Figure 2.3(b) is series connection of normally-on GaN HEMT shown in Fig. 2.2 and low voltage normally-off Si MOSFET. The gate of GaN HEMT is connected to source of Si MOSFET. In this structure, the Si MOSFET provide normally-off and isolated gate, and the GaN HEMT provide high breakdown voltage. However, in the cascade connection, the on-resistance is the sum of that in Si MOSFET and that in GaN HEMT. Therefore, it is difficult to achieve low on-resistance compared to other structures.

Figure 2.3(c) is called *p*-gate structure. The 2DEG is depleted by processing a *p*-type layer below the gate metal. *p*-type doping and nitride passivation are required for the fabrication. The GaN HEMTs treated in this thesis are basically *p*-type gate structure. The actual cross-sectional structure of GaN HEMTs depends on structure designs determined by the parameters as blocking voltage and forward current.

Figure 2.4 shows the band diagram of normally-off GaN HEMT. In normally-off GaN HEMTs, the equilibrium state is the off state and there is no 2DEG under the gate metal. When the gate voltage exceeds the threshold voltage, 2DEG is generated and current can flow between drain and source. Φ_B is work function of metal. $\Delta\varepsilon_c$ is difference of conduction band edge ε_c.

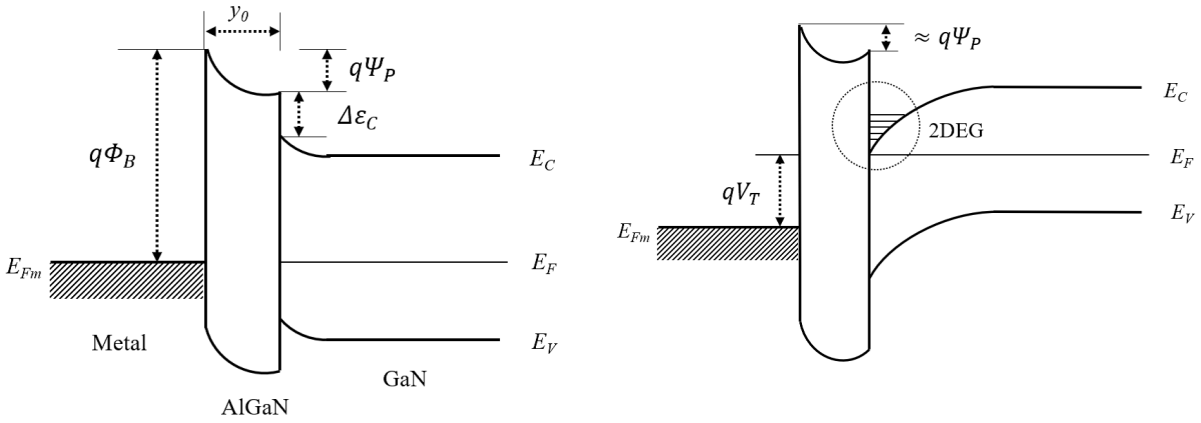

(a) Off state. (b) On state.

Figure 2.4 Band diagram of normally-off GaN HEMT.

The potential variation within the depleted region Ψ_p is expressed in Eq. 2.21, where ϵ_s is permittivity of GaN and y_0 is the thickness of AlGaN layer.

$$\Psi_p = \frac{eN_D y_o^2}{2\epsilon_s} \tag{2.21}$$

By using Ψ_p, threshold voltage V_{th} is expressed as Eq. 2.22.

$$V_{th} \approx \Phi_B - \Psi_p + \frac{\Delta E_c}{e} \tag{2.22}$$

With the condition that gate voltage is higher than the threshold voltage, the charge in the channel Q_n is expressed as Eq. 2.23.

$$Q_n = C_o(V_G - V_{th}) \tag{2.23}$$

In Eq. 2.23, C_o is expressed as Eq. 2.24, where Δy is the channel thickness of the 2DEG.

$$C_o = \frac{\epsilon_s}{y_0 + \Delta y} \tag{2.24}$$

Assuming constant carrier mobility, the drain current I_D is expressed as Eq. 2.25, where Z, L, and V_D is channel width, channel length, and drain-source voltage.

$$I_D = \frac{Z\mu_e C_o}{L}\left[(V_G - V_{th})V_D - \frac{V_D^2}{2}\right] \tag{2.25}$$

In the linear region, where $V_D \ll (V_G - V_{th})$, Eq. 2.25 is expressed as Eq. 2.26, where I_{Dlin} is drain current in linear region.

$$I_{Dlin} = \frac{Z\mu_e C_o (V_G - V_{th}) V_D}{L} \tag{2.26}$$

At high V_D, pinch-off occurs in the channel. The saturated drain voltage V_{Dsat} is expressed as Eq. 2.27.

$$V_{Dsat} = V_G - V_{th} \tag{2.27}$$

The saturation drain current I_{Dsat} is expressed as Eq. 2.28.

$$I_{Dsat} = \frac{Z\mu_e C_o}{2L} (V_G - V_{th})^2 \tag{2.28}$$

From Eq. 2.28, transconductance g_m is expressed as Eq. 2.29.

$$g_m \equiv \frac{dI_{Dsat}}{dV_G} = \frac{Z\mu_e C_o (V_G - V_{th})}{L} \tag{2.29}$$

The on-resistance of GaN HEMT is expressed as Eq. 2.20. Generally, lateral devices have smaller channel cross-sectional area than vertical devices and are not suitable for high current flow. On the contrary, GaN HEMTs can provide lower on-resistance and higher breakdown voltage than Si MOSFETs due to GaN properties.

GaN HEMTs have not only superior characteristics but also drawbacks. Vertical type power MOSFETs have parasitic *pn* junctions that allow reverse conduction between drain and source, which is called body diode. In order to achieve reverse conduction in GaN HEMTs, the drain and source are made asymmetrically with respect to the gate electrode. This causes charge accumulation on the gate when reverse voltage is applied between the source and drain. This charge forms the channel of the 2DEG, achieving reverse conduction. At this time, the voltage drop of V_{th} in the gate and that drop due to the channel resistance are generated between the source and drain. The sum of these voltage drops is generally higher than the forward voltage of the body diode of Si power MOSFETs. Therefore, the power loss due to reverse current is higher than that of Si power MOSFETs.

Low loss reverse conduction can be achieved by such methods as connecting SBDs in parallel. However, commercially available GaN power semiconductor devices currently utilize GaN on Si substrates, which make the vertical GaN devices difficult. There

are few commercially available GaN SBDs. Additionally, lateral structure is difficult to use 2DEG in SBDs. Thus, it is difficult to achieve low resistance, high breakdown voltage, and fast switching as vertical structure. Diodes are essential as components of power conversion circuits. Therefore, wide bandgap semiconductors such as β-Ga_2O_3, for which single crystals can be fabricated, are expected to be used for diodes.

The parasitic capacitance in the lateral GaN power semiconductor device differs from that of vertical power MOSFETs. The gate-drain and drain-source capacitances of GaN HEMTs are lower than those of vertical devices. Therefore, the amount of charge during switching operation is small, which enables high-speed switching. Soft-switching technology is often used in high-frequency power conversion circuits to reduce switching losses. Soft-switching is based on resonance circuits, where the parasitic capacitance of power semiconductor devices can be used as a component of resonance. In circuits using Si power MOSFETs, parasitic capacitance of power semiconductor devices has been modeled to analyze the conditions of soft-switching[73]-[79]. Nevertheless, the model of power MOSFETs is not applicable for lateral GaN HEMTs. Therefore, it is necessary to consider a parasitic capacitance model suitable for GaN HEMTs.

2.4 Ga_2O_3 power semiconductor devices

Ga_2O_3 has multiple polymorphs types. α type and β type are the most expected to be used for power semiconductor devices. α type has wider bandgap than β type. However, α type single crystal is grown using heteroepitaxy on sapphire substrates. This makes it difficult to fabricate devices with vertical structures. In addition, the cost of wafers is high due to the sapphire substrates.

β-Ga_2O_3 is capable of growing single crystals from solution under atmospheric pressure. Therefore, it is expected that wafers can be manufactured at low cost. There are already many reports on SBD of β-Ga_2O_3[15][16][18]. In addition, lateral and vertical structure transistors using β-Ga_2O_3 have already been reported[51]-[52]. Nonetheless, Ga_2O_3 transistors are still in the research and development stage. This thesis uses β-Ga_2O_3 SBDs as Ga_2O_3 power semiconductor devices.

Figure 2.5 shows structure of typical β-Ga_2O_3 SBD. The SBD in Fig. 2.5 consists

of n type β-Ga_2O_3 and a Schottky metal[89][90].

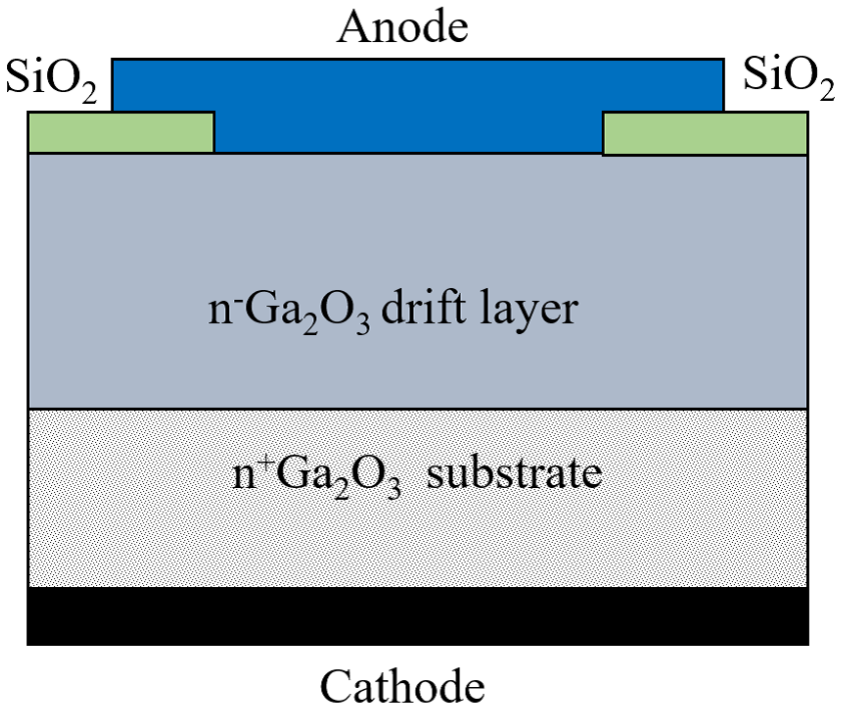

Figure 2.5 Structure of β-Ga_2O_3 SBD.

Figure 2.6 shows the band diagram of β-Ga_2O_3 SBD. The barrier hight Φ_B is expressed as Eq. 2.30, where Φ_m is work function of metal and χ is electron affinity of β-Ga_2O_3, respectively[91].

$$e\Phi_B = e\left(\Phi_m - \chi\right) \tag{2.30}$$

From Eq. 2.30, The Schottky barrier height is determined by the physical properties of the Schottky metal and semiconductor.

When forward voltage is applied to the anode-cathode as shown in Fig. 2.6(b), the forward current density J is expressed as Eq. 2.31.

$$\begin{aligned} J &= \left(\frac{4\pi e m^* k^2}{h^3}\right) T^2 \exp\left(-\frac{e\Phi_B}{kT}\right)\left[\exp\left(\frac{eV}{kT}\right) - 1\right] \\ &= A^* T^2 \exp\left(-\frac{e\Phi_B}{kT}\right)\left[\exp\left(\frac{eV}{kT}\right) - 1\right] \end{aligned} \tag{2.31}$$

A^* is called effective Richardson constant. A^* is expressed as Eq. 2.32.

$$A^* = \frac{4\pi e m^* k^2}{h^3} \tag{2.32}$$

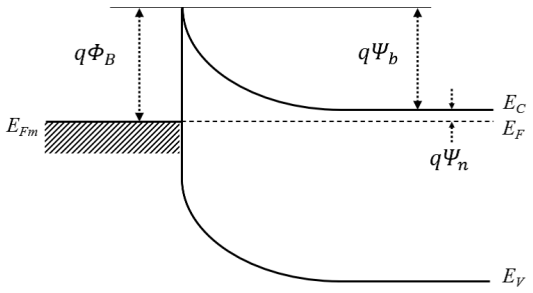

(a) Equilibrium state.

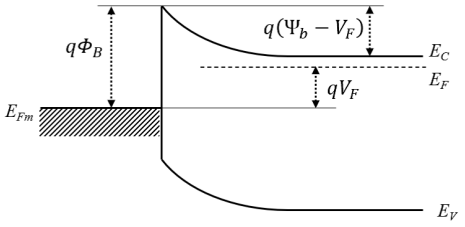

(b) Forward conduction.

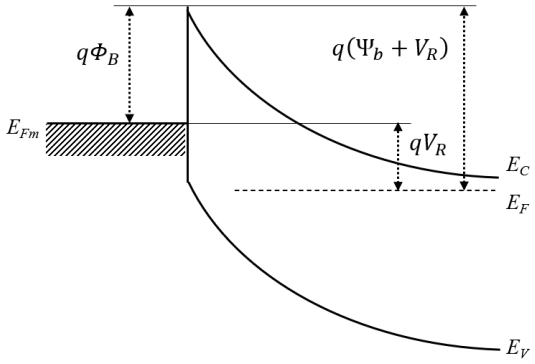

(c) Reverse blocking.

Figure 2.6 Band diagram of β-Ga_2O_3 SBD.

Assuming the cross-sectional area of the Schottky junction is S, the relationship between forward current and voltage is expressed as Eq. 2.33 from Eq. 2.31.

$$\begin{aligned} I_f &= A^* S T^2 \exp\left(-\frac{e\Phi_B}{kT}\right)\left[\exp\left(\frac{eV}{nkT}\right) - 1\right] \\ &= I_s\left[\exp\left(\frac{eV}{nkT}\right) - 1\right] \end{aligned} \tag{2.33}$$

In Eq. 2.33, I_s is called saturation current and expressed as Eq. 2.34.

$$I_s = A^* S T^2 \exp\left(-\frac{e\Phi_B}{kT}\right) \tag{2.34}$$

n in Eq. 2.33 is called ideal factor. In ideal SBD, $n = 1$ and Eq. 2.31 coincide to Eq. 2.33. If the characteristics of the SBD are not ideal, n deviates from 1. The ideal factor is an indicator of the ideality of the SBD[92]-[95].

When reverse voltage is applied to the anode-cathode as shown in Fig. 2.6(c), the depletion width W_D is expressed as Eq. 2.35.

$$W_D = \sqrt{\frac{2\epsilon_s}{eN_D}\left(\Psi_b - V_R - \frac{kT}{e}\right)} \tag{2.35}$$

As the reverse voltage is increased, avalanche breakdown occurs when the critical electric field strength is exceeded. This avalanche voltage is the limit breakdown voltage of the SBD. However, in actual SBDs, leakage current flows at the Schottky junction when reverse voltage is applied. Since the critical electric field strength of Ga_2O_3 is higher than that of other semiconductors, the blocking voltage is often limited by the leakage current. To reduce leakage current when reverse voltage is applied, trench type structure as shown in Fig. 2.7 has been proposed[96]-[98].

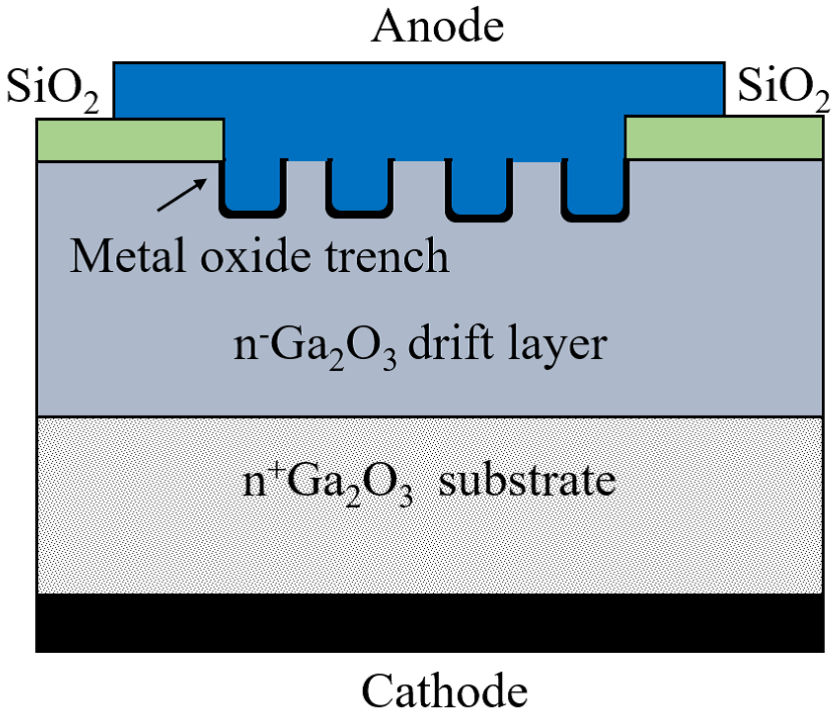

Figure 2.7 Structure of trench type β-Ga_2O_3 SBD.

Trench type SBD has metal oxide grooves into the Schottky junction. This metal oxide groove is located on the cathode side of the Schottky junction. Therefore, strong

electric field is applied to the Schottky metal and the drift layer across the metal oxide. Since the critical electric field strength of Ga_2O_3 is high, the formation of the trench does not cause breakdown voltage reduction. The presence of the trench mitigates the electric field in the Schottky junction when reverse voltage is applied. Therefore, leakage current can be reduced to low level.

Ga_2O_3 is currently difficult to achieve p-type doping. Consequently, trench SBD is an effective method to achieve high blocking voltage. This thesis also evaluates both conventional (planar type) and trench type SBDs.

Ga_2O_3 is expected to be a useful semiconductor material owing to its trench type structure and other innovations. However, it has a serious drawback. Ga_2O_3 has lower thermal conductivity than other semiconductor materials. In vertical SBDs, heat is dissipated from the active area through the die-bonding of the cathode. The heat dissipation performance from this active area to die-bonding is determined by the thermal conducting characteristics of the semiconductor device. Flip mounting has been attempted as a method to reduce the thermal resistance of Ga_2O_3 power semiconductor devices[63]. However, while flip mounting is effective for diodes, it cannot be applied to vertical structure transistors due to wiring problems. Therefore, it is important to develop methods for thermal resistance reduction, such as increasing the area of the dies and making it thinner.

2.5 Summary

In this chapter, the physical properties and structure of gallium compound power semiconductor devices were described. The wide bandgap semiconductor properties improve the characteristics of power semiconductor devices. GaN HEMTs and Ga_2O_3 SBDs considered in this paper were described. GaN HEMTs are capable of high-speed operation with 2DEG. However, they have drawbacks attributable to lateral device structure.

β-Ga_2O_3 is expected as future material for power devices due to its wide bandgap, high critical electric field strength, and ease of single crystal fabrication. Trench structure has been proposed for SBD to reduce leakage current. However, it is essential to

investigate methodologies to reduce thermal resistance for practical use.

Chapter 3

Characterization and modeling of magnetic components for class-E amplifier using GaN HEMT

3.1 Introduction

Compact, lightweight, and highly efficient power conversion circuits are indispensable for the recent trend. Passive components such as inductors and transformers occupy a large volume in power conversion circuits. Higher operating frequency is effective to reduce their size. The application of switching devices using wide bandgap semiconductors such as GaN and Ga_2O_3 is expected to realize high-frequency switching power conversion circuits.

On the other hand, high-frequency operation by hard-switching of power converters leads to increment in switching losses. In order to suppress switching losses, soft-switching is effective. Soft-switching is the technique that the current or voltage becomes zero at the transition of switching.

However, especially in circuit operation above 10 MHz, the loss of magnetic components cannot be ignored. Air-core inductors that do not use magnetic materials are used for high frequency power converters. While air-core inductors do not have iron loss or magnetic saturation caused by magnetic materials, they require a large volume to achieve the inductance necessary for operation. That makes it difficult for

power converters to realize compact and high-density. In addition, the suppression of electromagnetic noise radiated into the space is also an issue. Therefore, there are growing demands for the development of magnetic materials applicable to high-frequency switching power supply circuits.

This section focuses on class-E amplifiers, which can operate with low loss at high frequency by soft-switching. Class-E amplifiers are expected to be a power conversion circuit applicable to wireless power transmission in IoT devices. It is analytically possible to calculate the operation of a class-E amplifier composed of ideal elements. However, actual components do not exhibit ideal characteristics. In particular, magnetic components deviate from ideal electrical characteristics due to the magnetic properties of magnetic cores and parasitic components that depend on the structure of the windings. Magnetic materials with low permeability and low loss that can be used in power supply circuits operating at high frequencies above 10 MHz show particularly large deviations from ideal electrical characteristics. Therefore, in order to design an actual circuits that achieves soft-switching operation, it is necessary to analyze by circuit simulation[99]. Simulation requires the components models that take into account the non-ideal characteristics of magnetic components.

Circuit simulation for the design of 10 MHz band class-E amplifiers requires a circuit element model that can simulate the harmonic characteristics above 10 MHz band. In this section, magnetic characteristics are evaluated by 2-port measurement using a network analyzer for the purpose of evaluation up to high frequency range. Equivalent circuit modeling is performed based on the measurement results. The model parameters are extracted by using the equivalent transformation of the 2-port circuit. In a previous study, an attempt has been made to extract the magnetic properties of magnetic materials such as magnetic thin films from the S-parameters obtained using a network analyzer[22]. There are no examples of magnetic component models used in high-frequency switching power conversion circuits.

In this section, modeling is performed based on S-parameters obtained from 2-port measurements of toroidal cores for inductors used in class-E amplifiers. 2-winding method is a commonly used measurement method for magnetic characteristics such as B-H analyzers. There are no general-purpose measurement equipments for frequency

bands above 10 MHz. For this reason, this section utilizes a 2-port measurement using a network analyzer that measures the reflectance of power, which is different from voltage and current measurements, as a measurement equivalent to the 2-wire method. This method evaluates the magnetic characteristics of inductors and transformers in the frequency band above 10 MHz. This method aims to separately extract equivalent circuit model parameters such as coupling capacitance of windings and leakage inductance, which are problems in the high frequency band. In this section, the validity of the proposed 2-port measurement is verified by comparing with a 1-port measurement. Furthermore, the validity of the circuit simulation using the obtained equivalent circuit model is verified based on the circuit experiment of class-E amplifiers.

3.2 Class-E amplifier

This chapter describes the operation of the class-E amplifier under study and issues related to magnetic components used in class-E amplifiers.

3.2.1 The operation of a class-E amplifier

Class-E amplifiers can significantly reduce switching losses by soft-switching. Soft-switching used in class-E amplifier is zero voltage switching (ZVS). In ZVS, the voltage applied to the switching device is zero during turn-on and turn-off. In addition, class-E switching utilize zero derivative voltage switching (ZDVS) which sets the rate of voltage change at turn-on and turn-off zero.

Figure 3.1 shows the circuit diagram of the class-E amplifier discussed in this section. It consists of a class-E amplifier with output impedance R' and an L-type matching circuit consisting of L_m and C_m to match the load impedance R.

In order to achieve the class-E soft-switching conditions of ZVS and ZDVS, the switching device Tr is driven with a constant operating frequency f and a constant duty ratio of 50%. Soft-switching utilizes the resonance phenomenon of C_{sh}, C_t, and L_t. L_c is a choke inductor. When the L_c is high enough, ripple in power supply current I_{in} is small enough and I_{in} can be regarded as direct current. The circuit parameters that realizes class-E soft-switching with $V_{ds} = 0$ and $dV_{ds}/dt = 0$ at turn-

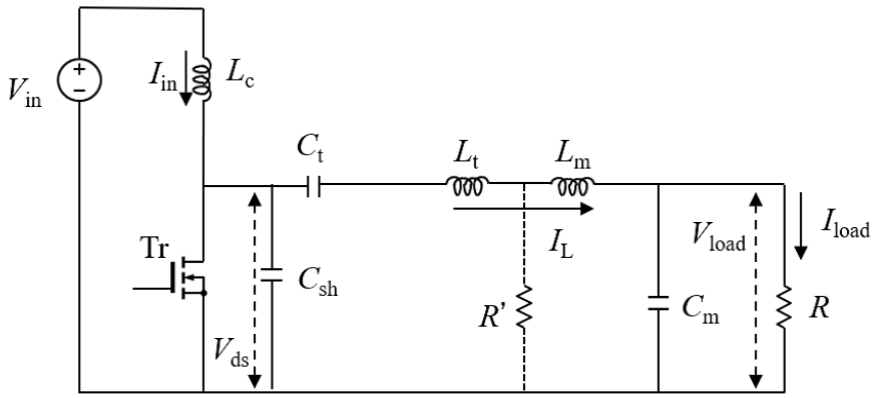

Figure 3.1 Circuit diagram of class-E amplifier with L type matching circuit.

on of switching device Tr, are given by Eq. 3.1 to Eq. 3.4. This section assumes $R' < R$ and $Q_L = (2\pi f L_t)/R' > 1.7879$, where the Q_L is quality factor of L_t and R'. ω is expressed as $\omega = 2\pi f$.

$$C_{sh} = \frac{1}{\omega R' \left(\frac{\pi^2}{4} + 1\right) \frac{\pi}{2}} \left(0.9987 + \frac{0.9142}{Q_L} - \frac{1.0318}{Q_L^2}\right) + \frac{0.6}{\omega^2 L_c} \tag{3.1}$$

$$C_t = \frac{1}{\omega R'} \left(\frac{1}{Q_L - 0.1048}\right) + \left(1.0012 + \frac{1.0147}{Q_L - 1.7879}\right) - \frac{0.2}{\omega^2 L_c} \tag{3.2}$$

$$L_m = \frac{R'}{\omega} \sqrt{\frac{R}{R'} - 1} \tag{3.3}$$

$$C_m = \frac{1}{R\omega} \sqrt{\frac{R}{R'} - 1} \tag{3.4}$$

The drain-source voltage applied to switching device Tr is expressed in Eq. 3.5.

$$V_{ds} = \begin{cases} 0 & 0 < \omega \leq \pi \\ V_{in}\pi \left(\omega t - \frac{3\pi}{2} - \frac{\pi}{2}\cos\omega t - \sin\omega t\right) & \pi < \omega \leq 2\pi \end{cases} \tag{3.5}$$

The drain current conducting in switching device is expressed in Eq. 3.6, where $\phi = 2.575$ rad.

$$I_d = \begin{cases} I_{in}\left(1 - \frac{\sqrt{\pi^2+4}}{2}\sin\left(\omega t + \phi\right)\right) & 0 < \omega \leq \pi \\ 0 & \pi < \omega \leq 2\pi \end{cases} \tag{3.6}$$

Equation 3.5 indicates that the maximum value of V_{ds} is 3.562 times V_{in}. Equation 3.6 indicates that the maximum value of I_d is 2.575 times I_{in}. Circuit topologies such as class-E/F and class-Φ_2 have been proposed to suppress the maximum value.

3.2.2 Issues in the design of class-E amplifiers

Equations 3.1 to 3.3 give the soft-switching conditions for a class-E amplifier. They are for ideal elements and not for actual elements and circuits with parasitic components. In the design of a class-E amplifier, it is necessary not only to design circuit components but also to analyze the behavior in actual circuits with parasitic components. For this purpose, circuit simulation is used, which requires a detailed model to simulate the characteristics of components.

In the circuit of Fig. 3.1, the output impedance R' of the class-E amplifier is not directly implemented in the circuit, but it is connected to the load R via a matching circuit. Therefore, the characteristics of the inductor affect not only the soft-switching operation, but also the impedance matching between the output and the load.

In the high-frequency switching operation at 10 MHz in this study, the inductor deviates significantly from ideal characteristics due to losses and parasitic components in the cores and windings. It cannot be considered as an ideal components like other passive devices.

Losses in magnetic components are mainly caused by iron and copper losses. The model used in circuit simulation must be able to account for these losses in detail. Section 3.3 describes how to evaluate the magnetic properties of an inductor used in a class-E soft-switching circuit and how to extract the model parameters for the electrical characteristics.

3.3 Evaluation and modeling of magnetic properties for power inductors

This section discusses a method for evaluating the magnetic characteristics of inductors used in class-E amplifiers for switching operation at 10 MHz and a model for circuit

simulation.

3.3.1 Magnetic materials considered in this chapter

This chapter considers iron-based metal composite material and carbonyl iron composite material as low-loss magnetic materials for use in class-E amplifiers with switching operation at 10 MHz. The iron-based metal composite material is a composite of iron-based amorphous alloy with an average grain size of 2.56 μm, which is solidified with epoxy resin. The ratio of magnetic material is 91.5 wt.%. The core is molded into a toroidal shape and annealed at 300 °C for 3 hours. The iron-based metal composite material is Sample 1. The carbonyl iron powder material is toroidal core T106-2 (Micrometals), which is Sample 2. The magnetic path of a toroidal core is isotropic with respect to the windings. This makes it a suitable for the evaluation of magnetic properties. However, toroidal cores have the problem of increasing volume compared to other types of cores.

Table 3.1 shows the core specifications. Relative permeability (Typ) is the datasheet value of the specific magnetic permeability of each core. Both sample 1 and sample 2 have saturation flux densities of 1.2 T or higher[100].

Table 3.1 Specifications of magnetic cores.

	Sample 1	Sample 2
Outer diameter (mm)	30.0	26.9
Inner diameter (mm)	10.0	14.5
Height (mm)	8.87	11.1
Mass (g)	27.1	21.0
Magnetic pass length (mm)	62.8	64.9
Magnetic cross section (mm^2)	88.7	65.9
Volume (mm^3)	5570	4280
Relative Permeability (Typ.)	9.6	10
Saturation magnetization (T)	1.26	1.48

Figure 3.2 shows the magnetic properties at 10 MHz measured with a B-H analyzer (SY-8218, Iwatsu). Both the excitation and detection windings are 6 turns of 0.8 mm

diameter single copper enameled wire. They are the same as the inductors for class-E amplifier designed in Sect. 3.4. A power amplifier (HSA 4101-IW, NF Corporation) is used for excitation. Magnetic saturation is not observed at the maximum possible magnetic flux density of 0.6 mT. Hysteresis loss is very low and difficult to measure.

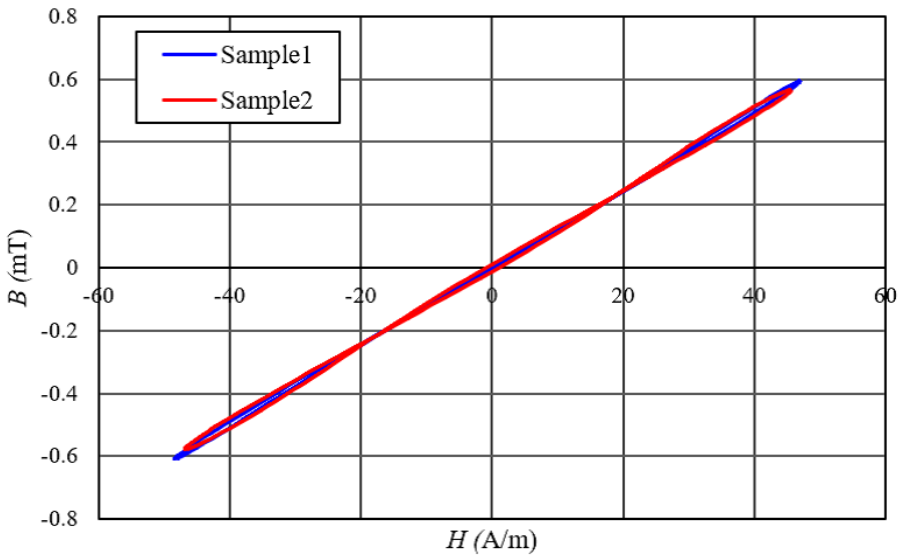

Figure 3.2 Magnetization characteristics measured with B-H analyzer.

Figure 3.3 shows the permeability measured by the B-H analyzer (solid line). Dash-dot lines are the THD of the current at the time of measurement. The permeabilities measured by the network analyzer are shown in Fig. 3.3, which are described in Sect. 3.3.2. The excitation current is set to 600 mA during the measurement.

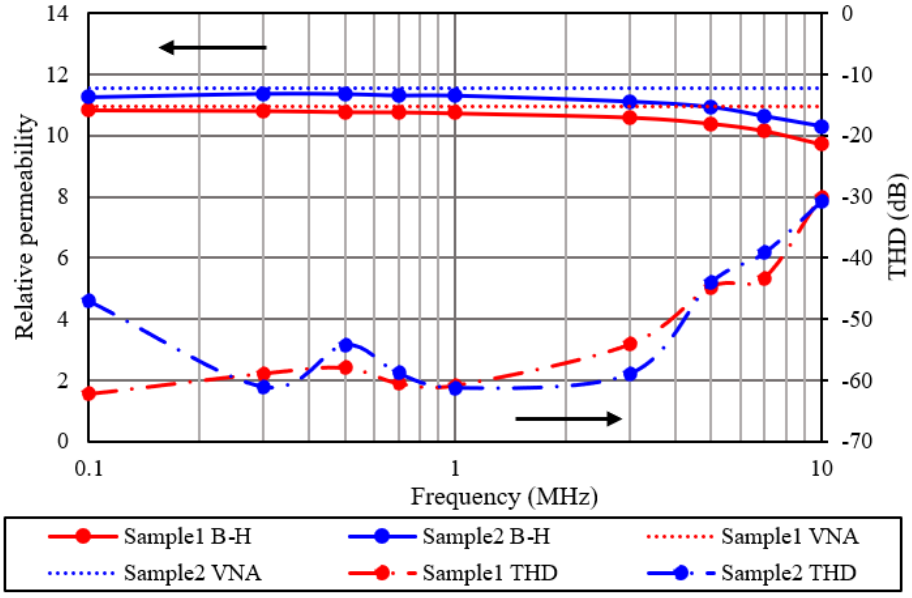

Figure 3.3 Permeability measured with B-H analyzer and vector network analyzer.

In the measurement with the B-H analyzer, the total harmonic distortion (THD) is −30 dB or higher at 5 MHz and above. The accuracy of the measurement is degraded, and magnetic characteristics can not be measured precisely. Therefore, this section attempts to measure the magnetic characteristics using other methods.

3.3.2 Evaluation of magnetic components using 2-port equivalent circuit model

This study considers a configuration equivalent to the 2-winding method of the B-H analyzer. In B-H analyzer measurements, excitation and detection are performed in individual windings. This thesis attempts to evaluate magnetic characteristics by 2-port S-parameter measurement using a network analyzer. Although the measurement signal from the network analyzer is small, the saturation flux density of the target magnetic material is 1.2 T or higher. The flux density applied to the magnetic components in the circuit considered in this thesis is 5 mT or lower. Under the conditions in this thesis, it is considered possible to evaluate magnetic properties even with measurements using a network analyzer.

Figure 3.4 shows the winding and connector of the toroidal core used for the 2-port

measurement of the network analyzer. The windings are 6:6 turns bifilar windings of 0.8 mm diameter single copper enameled wire. The terminals are SMA connectors, which are the reference plane connected to a network analyzer.

(a) Sample 1.

(b) Sample 2.

Figure 3.4 Overview of magnetic components under evaluation.

In this thesis, the magnetic properties are evaluated based on the 2-port S-parameter measurement using a network analyzer (E5061B, Agilent Technologies). The magnetic components are modeled with 2-port equivalent circuit. Figure 3.5 shows the 2-port equivalent circuit model considered in this thesis.

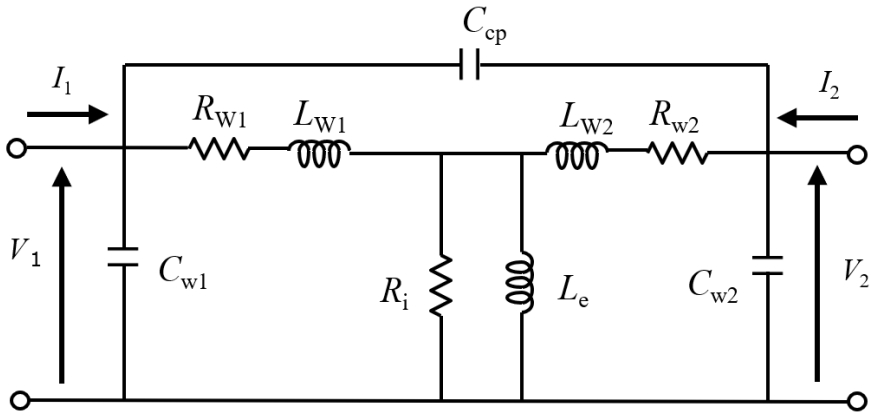

Figure 3.5 2-port equivalent circuit model of magnetic component.

In Fig. 3.5, C_{W1} and C_{W2} are the parasitic capacitances of each winding. R_{W1} and R_{W2} are the resistances of each winding. L_{W1} and L_{W2} are the leakage inductances.

R_i is the iron loss resistance. L_e is the excitation inductance. C_{cp} is the coupling capacitance. The equivalent circuit model of a transformer in the low-frequency range consists only of inductance and resistance[101]. However, in the high-frequency range, the capacitance of the windings cannot be ignored[102]. Therefore, this thesis uses a model including capacitance as Fig. 3.5. The relationship between the impedance and S-parameters of a 2-port circuit is expressed by Eq. 3.7, where Z_0 is the reference impedance connected to each port.

$$\begin{aligned}\begin{bmatrix} V_1 \\ V_2 \end{bmatrix} &= \begin{bmatrix} \frac{(1+S_{11})(1-S_{22})+S_{12}S_{21}}{(1-S_{11})(1-S_{22})-S_{12}S_{21}}Z_0 & \frac{2S_{12}}{(1-S_{11})(1-S_{22})-S_{12}S_{21}}Z_0 \\ \frac{2S_{21}}{(1-S_{11})(1-S_{22})-S_{12}S_{21}}Z_0 & \frac{(1-S_{11})(1+S_{22})+S_{12}S_{21}}{(1-S_{11})(1-S_{22})-S_{12}S_{21}}Z_0 \end{bmatrix} \begin{bmatrix} I_1 \\ I_2 \end{bmatrix} \\ &= \begin{bmatrix} Z_{11} & Z_{12} \\ Z_{21} & Z_{22} \end{bmatrix} \begin{bmatrix} I_1 \\ I_2 \end{bmatrix} \end{aligned} \tag{3.7}$$

The relationships between the component parameters in Fig. 3.5 and the Z parameters are expressed by the following equations.

$$Z_{11} = \frac{Z_\beta(Z_\alpha + Z_\gamma)}{Z_\alpha + Z_\beta + Z_\gamma} \tag{3.8}$$

$$Z_{12} = \left(\frac{Z_\beta}{Z_\beta + Z_\alpha}\right)\left(\frac{Z_\gamma\,(Z_\alpha + Z_\beta)}{Z_\alpha + Z_\beta + Z_\gamma}\right) \tag{3.9}$$

$$Z_{21} = \left(\frac{Z_\gamma}{Z_\gamma + Z_\alpha}\right)\left(\frac{Z_\beta\,(Z_\alpha + Z_\gamma)}{Z_\alpha + Z_\beta + Z_\gamma}\right) \tag{3.10}$$

$$Z_{22} = \frac{Z_\gamma(Z_\alpha + Z_\beta)}{Z_\alpha + Z_\beta + Z_\gamma} \tag{3.11}$$

Z_α, Z_β, and Z_γ are expressed by the following equations.

$$Z_\alpha = \frac{Z_f(Z_cZ_d + Z_eZ_c + Z_dZ_e)}{Z_eZ_f + Z_cZ_d + Z_eZ_c + Z_dZ_e} \tag{3.12}$$

$$Z_\beta = \frac{Z_a(Z_cZ_d + Z_eZ_c + Z_dZ_e)}{Z_dZ_a + Z_cZ_d + Z_eZ_c + Z_dZ_e} \tag{3.13}$$

$$Z_\gamma = \frac{Z_b(Z_cZ_d + Z_eZ_c + Z_dZ_e)}{Z_cZ_b + Z_cZ_d + Z_eZ_c + Z_dZ_e} \tag{3.14}$$

Z_a, Z_b, Z_c, Z_d, Z_e, and Z_f in Eq. 3.12 to Eq. 3.14 are expressed by the following

equations.

$$Z_a = -j\frac{1}{\omega C_{W1}} \tag{3.15}$$

$$Z_b = -j\frac{1}{\omega C_{W2}} \tag{3.16}$$

$$Z_c = R_{W1} + j\omega\ L_{W1} \tag{3.17}$$

$$Z_d = R_{W2} + j\omega\ L_{W2} \tag{3.18}$$

$$Z_e = \frac{j\omega R_i L_e}{R_i + j\omega L_e} \tag{3.19}$$

$$Z_f = -j\frac{1}{\omega C_{cp}} \tag{3.20}$$

The (Measure) in Fig. 3.6 and Fig. 3.7 show the frequency responses of the impedance in the 2-port circuit calculated from the measurement results. The frequency responses of Z_{12} and Z_{21} are almost identical for both Sample 1 and Sample 2. This indicates that duality is established, and the 2-port circuit can be treated as a linear time-invariant circuit.

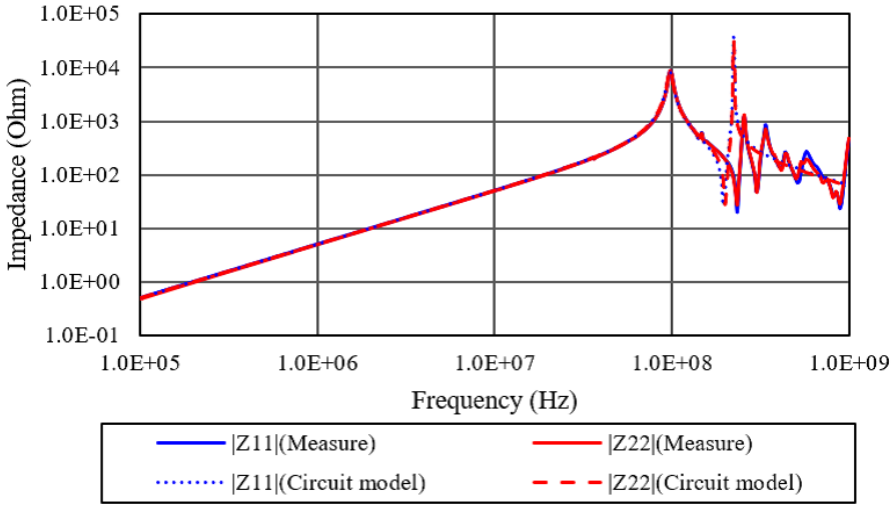

(a) Z_{11} and Z_{22}.

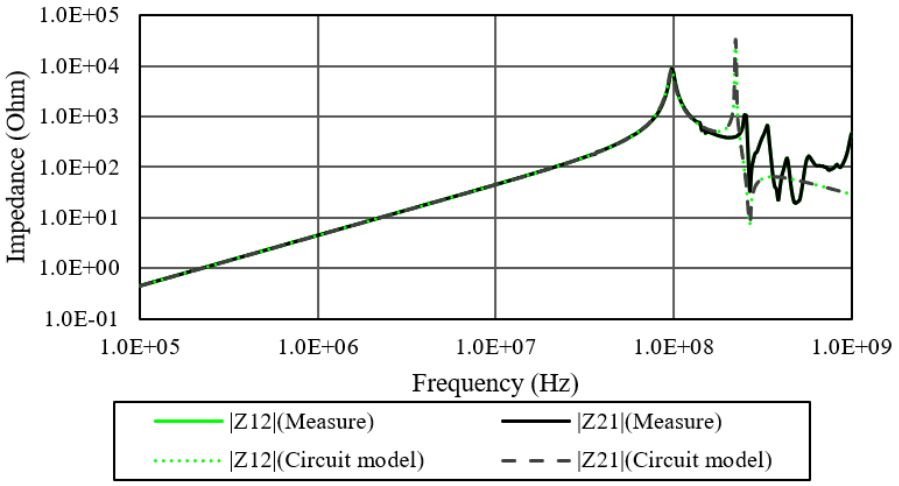

(b) Z_{12} and Z_{21}.

Figure 3.6 Measured and circuit modeled time response of Z-parameter for Sample 1.

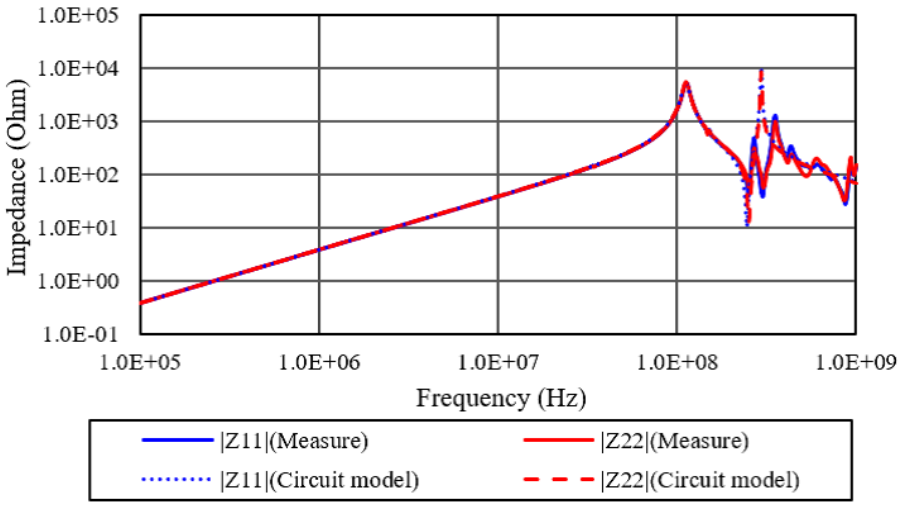

(a) Z_{11} and Z_{22}.

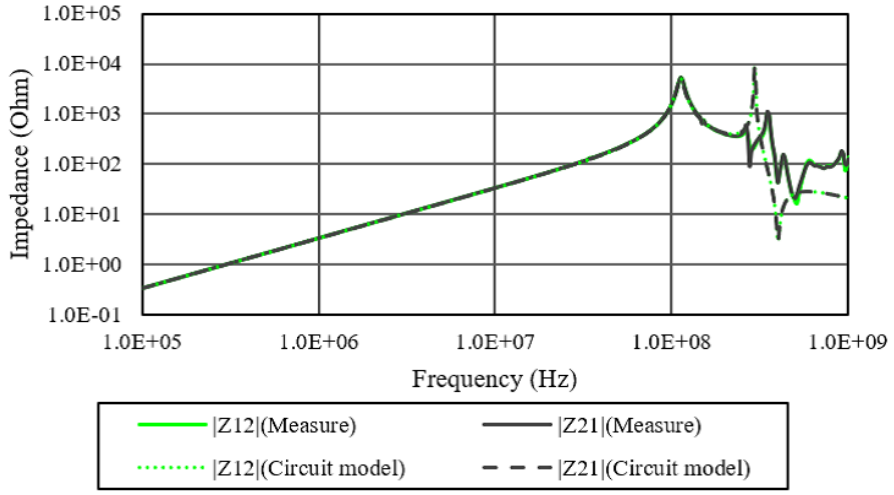

(b) Z_{12} and Z_{21}.

Figure 3.7 Measured and circuit modeled time response of Z-parameter for Sample 2.

The (Circuit model) in Fig. 3.6 and Fig. 3.7 show the frequency characteristics of the Z-parameters obtained using the equivalent circuit model shown in Fig. 3.5. The circuit parameters are obtained by the extraction method described below.

The 2-port circuit is represented by the π-type circuit in Fig. 3.8(a). Each element is expressed using the Z parameter as Eq. 3.21 to Eq. 3.23.

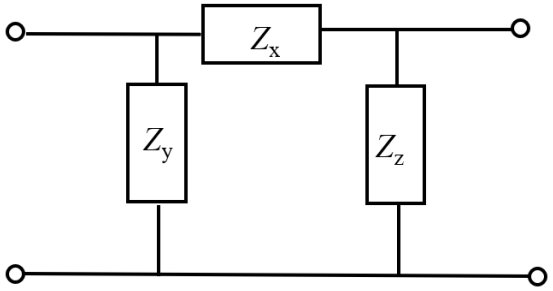

(a) π-type circuit of 2-port model.

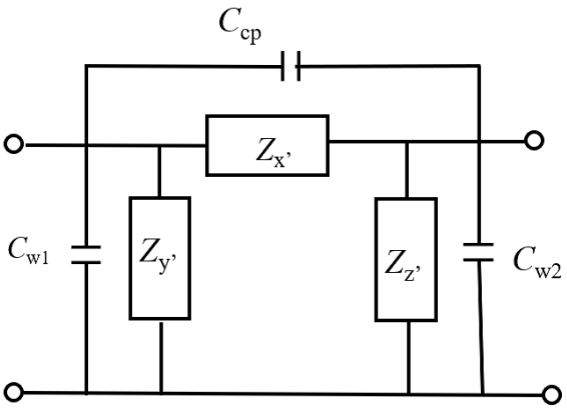

(b) π-type circuit with capacitance and residual impedance.

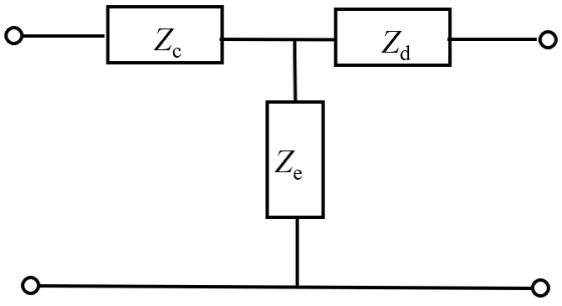

(c) T-type circuit without capacitance.

Figure 3.8 Equivalent circuits of 2-port circuit model.

$$Z_x = \frac{Z_{11}Z_{22} - Z_{12}^2}{Z_{12}} \tag{3.21}$$

$$Z_y = \frac{Z_{11}Z_{22} - Z_{12}^2}{Z_{22} - Z_{12}} \tag{3.22}$$

$$Z_z = \frac{Z_{11}Z_{22} - Z_{12}^2}{Z_{11} - Z_{12}} \tag{3.23}$$

Figure 3.9(a) and Figure 3.10(a) show the frequency response of Z_x, Z_y, and Z_z for Sample 1 and 2. The inductance and resistance that constitute the T-type circuit in Fig. 3.5 are converted to the π-type circuit. As shown in Fig. 3.8(b), Z_x is a parallel circuit of Z'_x and C_{cp}. Z_y is a parallel circuit of Z'_y and C_{W1}. Z_z is a parallel circuit of Z'_z and C_{W2}.

As shown in Fig. 3.9(a) and Fig. 3.10(a), the frequency characteristics of Z_x, Z_y, and Z_z vary by 20 dB/dec in the low frequency range respectively. The frequency characteristics of Z_x, Z_y, and Z_z vary by -20 dB/dec in the region above the self-resonant frequency. Therefore, it can be regarded as an LC parallel circuit. The capacitive elements are low and the impedance can be considered inductive below 10 MHz. The inductive elements of Z'_x, Z'_y, and, Z'_z are obtained by the least-squares approximation of the double logarithmic function for the frequency characteristics of each Z-f characteristics.

In the Z-f characteristics shown in Fig. 3.9(a) and Fig. 3.10(a), the capacitances C_{cp}, C_{W1}, and C_{W2} are obtained from the self-resonance frequency $f = 1/2\pi\sqrt{LC}$ at which the value of $|Z|$ is maximum. The self-resonant frequencies of Sample 1 and 2 are shown in Table 3.2.

Table 3.2 Self-resonant frequencies of Z_x, Z_y, and Z_z.

Sample 1	Z_x	269 MHz
	Z_y	97.7 MHz
	Z_z	97.7 MHz
Sample 2	Z_x	398 MHz
	Z_y	112 MHz
	Z_z	112 MHz

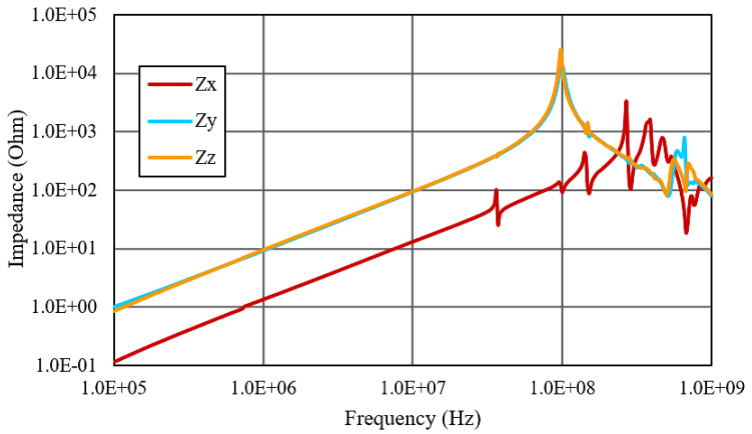

(a) Z-f characteristics of Z_x, Z_y, and Z_z.

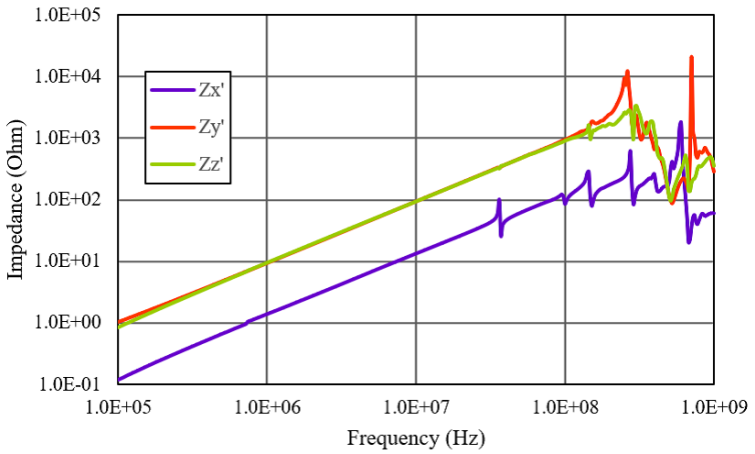

(b) Z-f characteristics of Z'_x, Z'_y, and Z'_z.

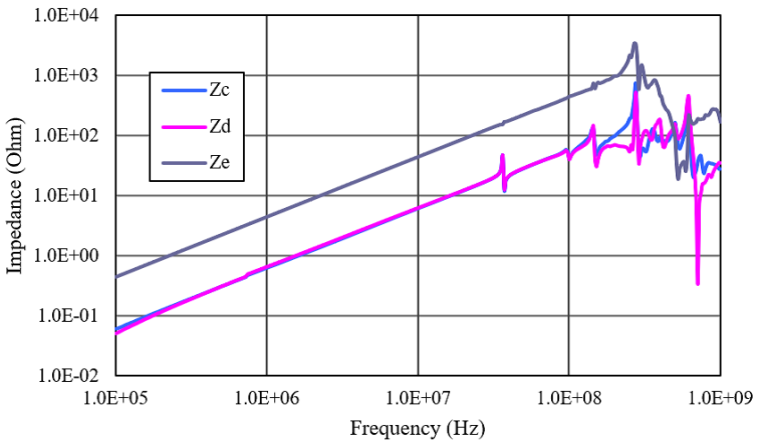

(c) Z-f characteristics of Z_c, Z_d, and Z_e.

Figure 3.9 Z-f characteristics of 2-port circuit model elements for Sample 1.

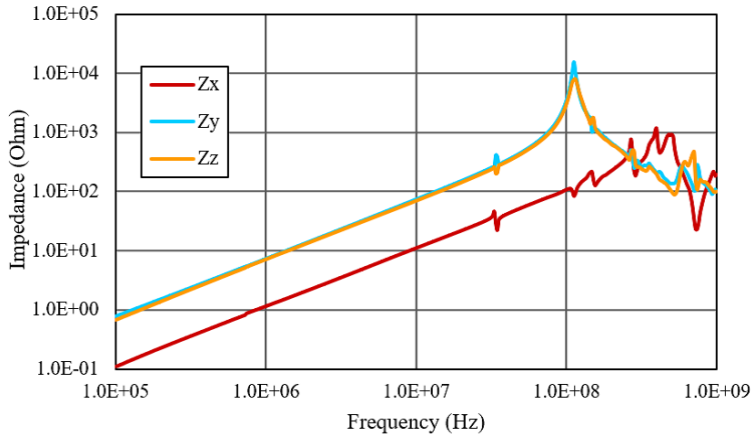

(a) Z-f characteristics of Z_x, Z_y, and Z_z.

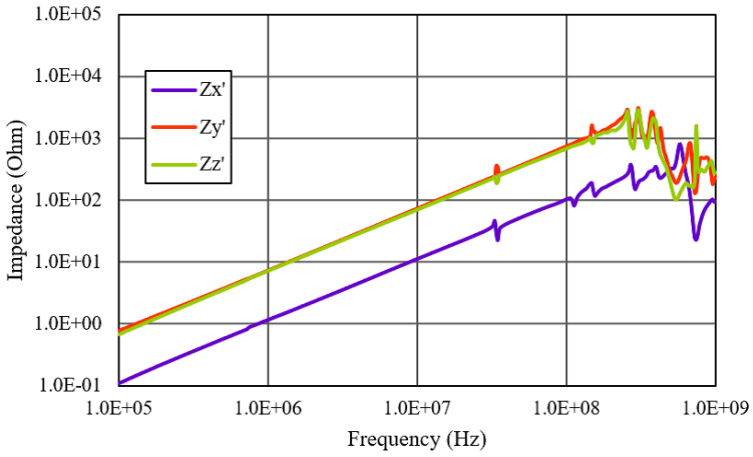

(b) Z-f characteristics of Z'_x, Z'_y, and Z'_z.

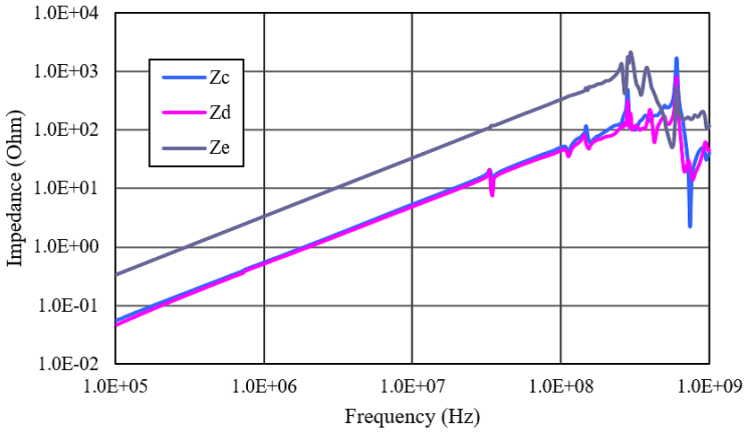

(c) Z-f characteristics of Z_c, Z_d, and Z_e.

Figure 3.10 Z-f characteristics of 2-port circuit model elements for Sample 2.

Figure 3.9(b) and Figure 3.10(b) show the frequency characteristics of Z'_x, Z'_y, and Z'_z. By using $\Delta - \mathrm{Y}$ transformation, π type circuit composed with Z'_x, Z'_y, and Z'_z is transformed into T type circuit shown in Fig. 3.8(c). Z_c, Z_d, Z_e are expressed as Eq. 3.24 to Eq. 3.26.

$$Z_c = \frac{Z_{x'} Z_{y'}}{Z_{x'} + Z_{y'} + Z_{z'}} \tag{3.24}$$

$$Z_d = \frac{Z_{x'} Z_{z'}}{Z_{x'} + Z_{y'} + Z_{z'}} \tag{3.25}$$

$$Z_e = \frac{Z_{y'} Z_{z'}}{Z_{x'} + Z_{y'} + Z_{z'}} \tag{3.26}$$

Figure 3.9(c) and Figure 3.10(c) show the frequency response of Z_c, Z_d, and Z_e for Sample 1 and 2. L_{W1}, L_{W2}, and L_e are obtained from the least-squares approximation of Z_c, Z_d, and Z_e below 10 MHz. The winding resistances are $R_{W1} \ll \omega L_{W1}$ and $R_{W2} \ll \omega L_{W2}$ in the range of measured frequencies, which make parameter extraction difficult. Thus, R_{W1} and R_{W2} are regarded as the DC resistances measured using a micro-resistance meter (6221&2182A, Keithley).

C_{W1}, C_{W2}, C_{cp}, L_{W1}, L_{W2}, L_e, R_{W1}, R_{W2}, and the self-resonant frequency are substituted into Eq. 3.8 to obtain the iron loss resistance R_i. R_i is the resistance that the value of $|Z11|$ at the self-resonant frequency is consistent with Eq. 3.8. Table 3.3 shows the extracted parameters.

The Z parameters obtained using the 2-port circuit parameters in Table 3.3 are shown for the dashed line (Circuit model) in Fig. 3.6 and Fig. 3.7. The frequency responses for impedance of the 2-port equivalent circuit model almost coincide with the measured values in the frequency below 200 MHz. The proposed methodology and extracted parameters are considered applicable as a model for 10 MHz switching circuits. The inconsistency in the frequency above 200 MHz is due to the influence of parasitic components that cannot be represented by the equivalent circuit shown in Fig. 3.5.

From the core specifications shown in Table 3.1 and the equivalent circuit parameters shown in Table 3.3, the Al value is given as Eq. 3.27. The complex relative permeability μ' and μ'' is given by Eq. 3.28, where l is the magnetic path length and S is the magnetic path cross-sectional area.

Table 3.3 Extracted component parameters of 2-port circuit.

	Sample 1	Sample 2
R_{W1} (mΩ)	10.4	8.8
R_{W2} (mΩ)	10.4	8.8
L_{W1} (nH)	98.3	85.0
L_{W2} (nH)	99.1	80.3
C_{W1} (pF)	1.70	1.68
C_{W2} (pF)	1.85	1.86
R_i (Ω)	7600	4570
L_e (nH)	700	530
C_{cp} (pF)	1.68	0.895

$$\mathrm{Al} = \frac{L_e}{N^2} \tag{3.27}$$

$$\mu' - j\mu'' = \frac{Z_e\, l}{j\omega N^2 S \mu_0} \tag{3.28}$$

The frequency characteristics of μ', μ'' and dissipation factor $\tan\delta = \mu''/\mu\prime$ for Sample 1 and 2 obtained from Eq. 3.28 are shown in Fig. 3.11. Table 3.4 shows the Al value, μ', μ'', and $\tan\delta$ of each core at 10 MHz.

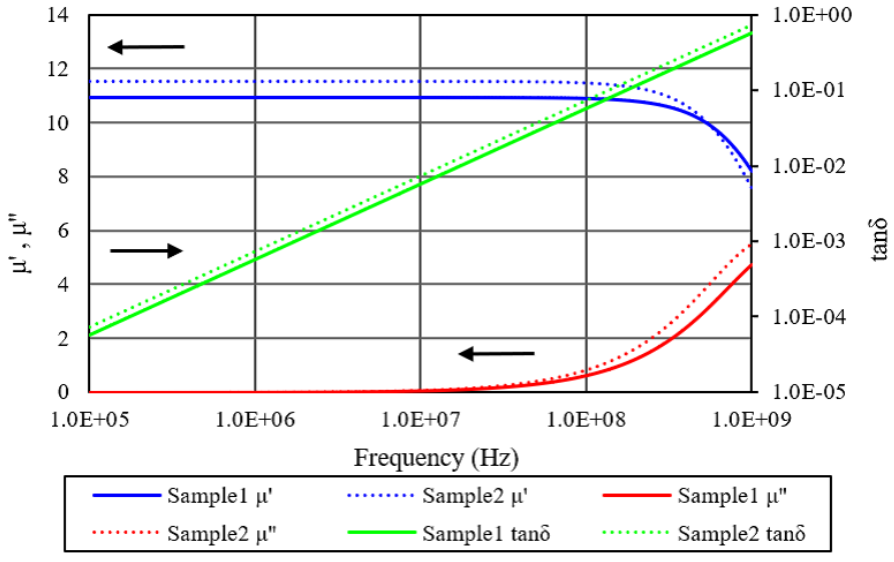

Figure 3.11 Magnetic characteristics of Sample 1 and 2.

Table 3.4 Relative permeability and dissipation factor of Sample 1 and 2.

	Sample 1	Sample 2
Al value ($\mathrm{nH/N^2}$)	19.44	14.72
μ'	10.95	11.54
μ''	0.0634	0.0840
$\tan\delta$	0.00579	0.00729

Sample 2 has higher μ' at low frequencies than Sample 1. However, at frequencies above 500 MHz, μ' in Sample 1 is lower than that in Sample 2. Also, $\tan\delta$ in Sample 1 is lower than that in Sample 2 in the frequency below 1 GHz. For magnetic components of the same inductance, the iron loss of Sample 1 can be lower than that of Sample 2. Since the values of μ' are similar for Sample 1 and Sample 2, it is possible to make Q_L almost the same for both sample with the same dimensions.

However, as Table 3.1 shows, the size of Sample 1 is larger than that of Sample 2. The Al value of Sample 1 is higher than that of Sample 2 as shown in Table 3.4. The number of turns N is an integer value and the inductance value obtained from Eq. 3.27 $L_e = \mathrm{Al} \times N^2$ is a discrete value. Therefore, arbitrary inductance cannot be designed. The actual circuits are fabricated with an approximation of the design values required for class-E operation.

3.3.3 Equivalent circuit model for inductors

From the 2-port circuit model, the equivalent circuit model of a 1-port inductor for a class-E amplifier is obtainable. In order to make class-E amplifier same as designed in Sect. 3.4, the wire for both Sample 1 and 2 is a single copper enameled wire of 0.8 mm diameter. The number of turns is set to 6.

The inductor has single winding. It can be regarded as a 1-port circuit with removing the secondary winding in the equivalent circuit model of Fig. 3.5. Figure 3.12 shows the equivalent circuit model of an inductor.

(Circuit model) in Fig. 3.13 shows the frequency response of the impedance obtained by substituting the parameters in Table 3.3 into the equivalent circuit model in Fig. 3.12. (Measured) in Fig. 3.13 shows the frequency response of the impedance

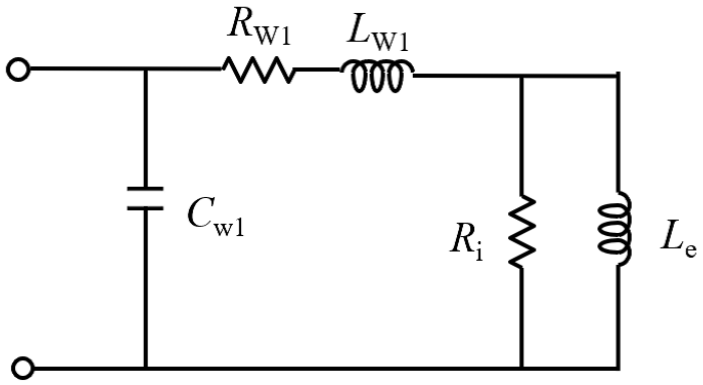

Figure 3.12 1-port equivalent circuit of inductor.

obtained from the S-parameter for the inductor measured by the 1-port measurement with a network analyzer.

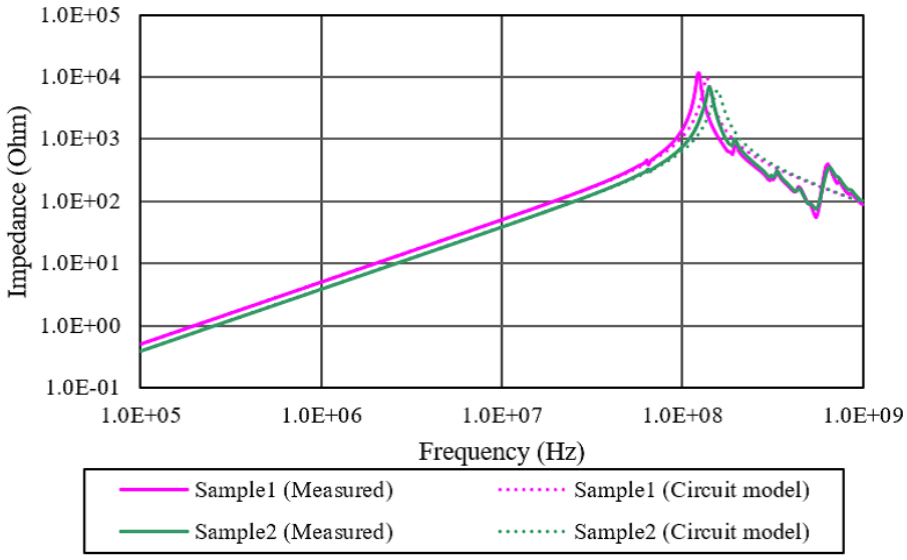

Figure 3.13 Z-f characteristics of inductors.

However, the parameters of the equivalent circuit model in Fig. 3.12 cannot be identified from the 1-port measurement using a method of circuit transformation as proposed in this thesis. In a class-E amplifier, harmonics above the 10th order have little effect on circuit operation[111]. The operating frequency in this thesis is 10 MHz. The model shown in Fig. 3.12 and parameters extracted from the 2-port measurements are considered sufficiently applicable to circuit simulation.

When the driving frequency is higher than 10MHz, the model used in this thesis is insufficient. A more precise model is necessary to simulate the characteristics in the region of 100 MHz or higher. It is important to study a more detailed model configuration that can simulate multiple resonance characteristics that exist above 100 MHz, and a method for extracting model parameters.

3.4 Verification of inductor model with class-E amplifiers

In this thesis, class-E amplifiers are operated with frequency of 10 MHz and output power of 20 W. The circuit parameters of the class-E amplifiers are determined from Eq. 3.1 to Eq. 3.4 and the equivalent circuit model parameters shown in Table 3.3. In this thesis, $L_t + L_m = L_{W1} + L_e$, and the constraint on the inductor is set to be $2 \leq Q_L \leq 4$. Table 3.5 shows the element constants of the class-E amplifiers. GaN HEMTs (PGA26E19BA, Panasonic) are used as switching devices.

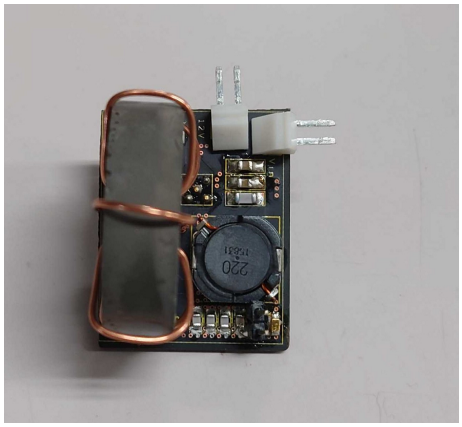

(a) Sample 1.

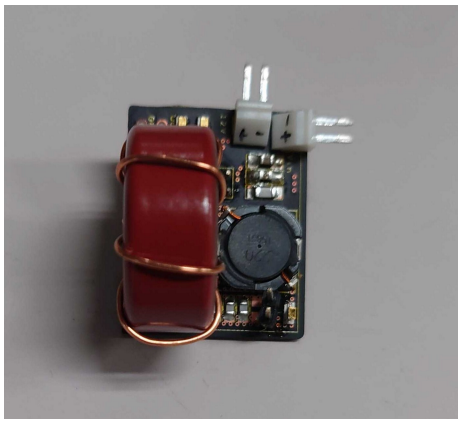

(b) Sample 2.

Figure 3.14 Overview of class-E amplifiers.

Figure 3.14 shows the overview of class-E amplifiers fabricated in this chapter. The class-E amplifier with Sample 1 is 27 mm in width, 34 mm in length, and 45 mm in height. The class-E amplifier with Sample 2 is 27 mm in width, 34 mm in length, and 41 mm in height. The class-E amplifiers fabricated in this chapter use inductors

with toroidal cores. This is because class-E amplifiers use the same cores as the ones used for the magnetic property evaluation in Sect 3.3. However, the toroidal core is not suitable for miniaturization due to its large volume. The design of the shape for magnetic components is necessary to miniaturize the power conversion circuits.

Table 3.5 Circuit parameters of class-E amplifiers.

	Sample 1	Sample 2
Q_L	4.0	2.5
L_c (μH)	22	22
C_{sh} (pF)	431	441
C_t (pF)	734	2013
$L_t + L_m$ (nH)	805	610
C_m (pF)	729	729
R' (Ω)	8	8
R (Ω)	50	50

Figure 3.15 shows the circuit diagram used in the circuit simulation. A modified nodal analysis method by Advanced Design System (Keysight) is used for the simulation.

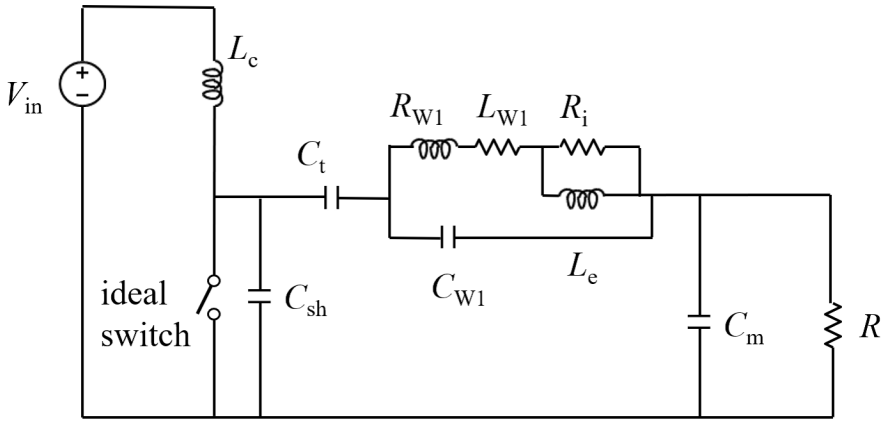

Figure 3.15 Circuit diagram used in the simulation.

Figure 3.16 and Figure 3.17 show the experimental and simulation results of the time response of the voltage and current in each part of the class-E amplifier. As shown in Fig. 3.1, V_{ds} is the drain-source voltage of the switching device, V_{load} and I_{load}

are the load resistance voltage and current, and I_L is the current flowing through the inductor. Output power is measured using a feed-through power meter (SX-1100, DIAMOND ANTENNA). V_{ds} and V_{load} are measured using optical isolated probe (TIVH08, Tektronix) and passive probe (TPP1000, Tektronix), respectively. I_L and I_{load} are measured using Rogowskii coil (SS-282, Iwatsu) and current transformer (model2877, Pearson), respectively.

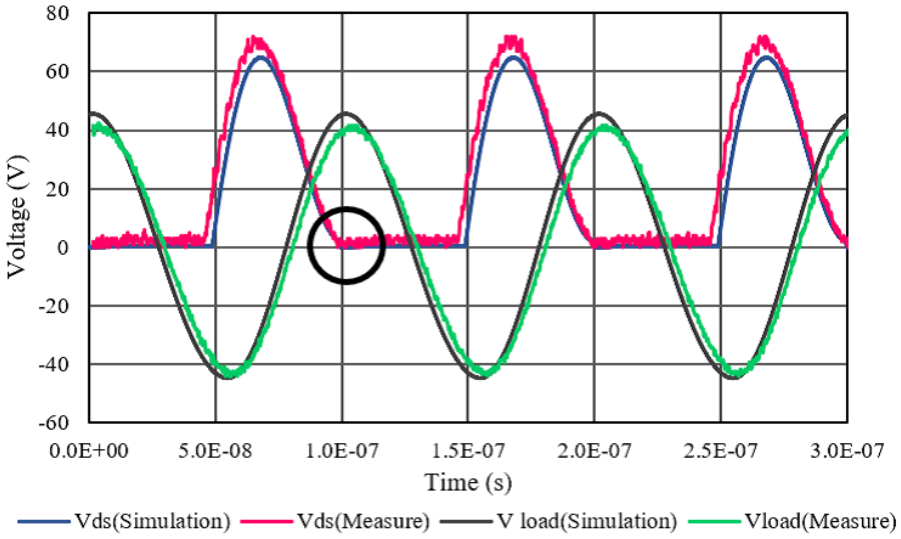

(a) Voltage time responses of class-E amplifier.

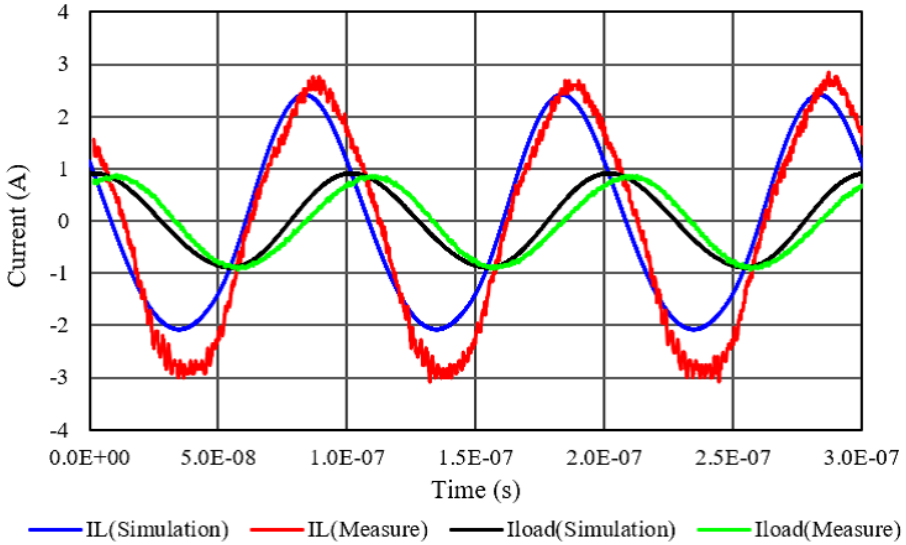

(b) Current time responses of class-E amplifier.

Figure 3.16 Measured and simulated time responses of class-E amplifier with Sample 1.

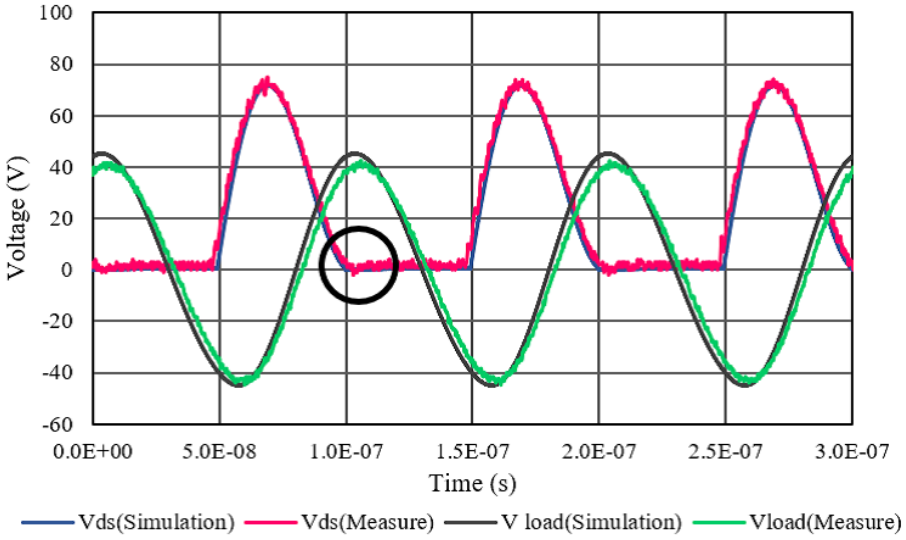

(a) Voltage time responses of class-E amplifier.

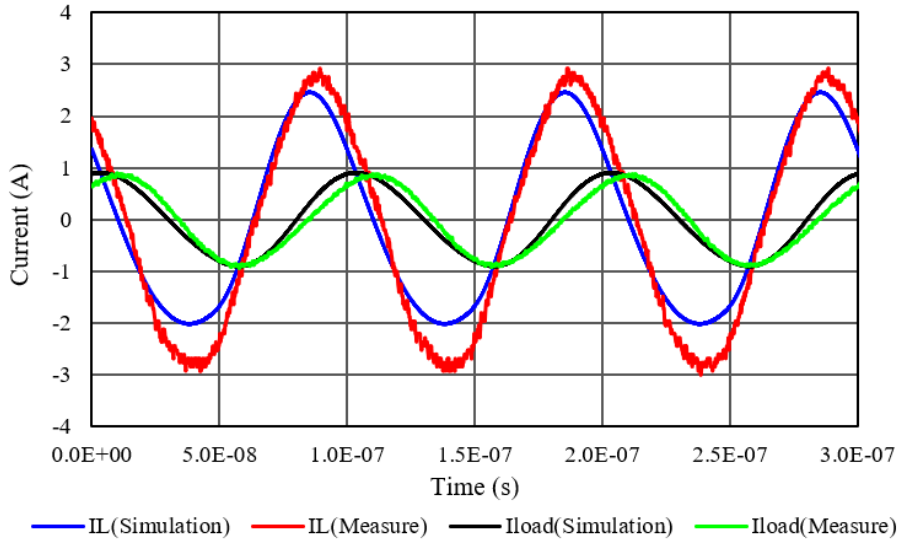

(b) Current time responses of class-E amplifier.

Figure 3.17 Measured and simulated time responses of class-E amplifier with Sample 2.

Figure 3.18 shows a magnified view of the time response of the switching device at turn-on, indicated by the black circles in Fig. 3.16(a) and Fig. 3.17(a). As shown in Fig. 3.18, when the switching device is turn-on, $V_{ds} = 0$ and $dV_{ds}/dt \approx 0$. Class-E operating conditions (ZVS and ZDVS) are almost achieved. In the simulation, ZVS and ZDVS are simulated as well as the measured time responses. It is confirmed that

the inductor model and extracted parameters with the method studied in this thesis can be used to simulate the operation of a class-E amplifiers.

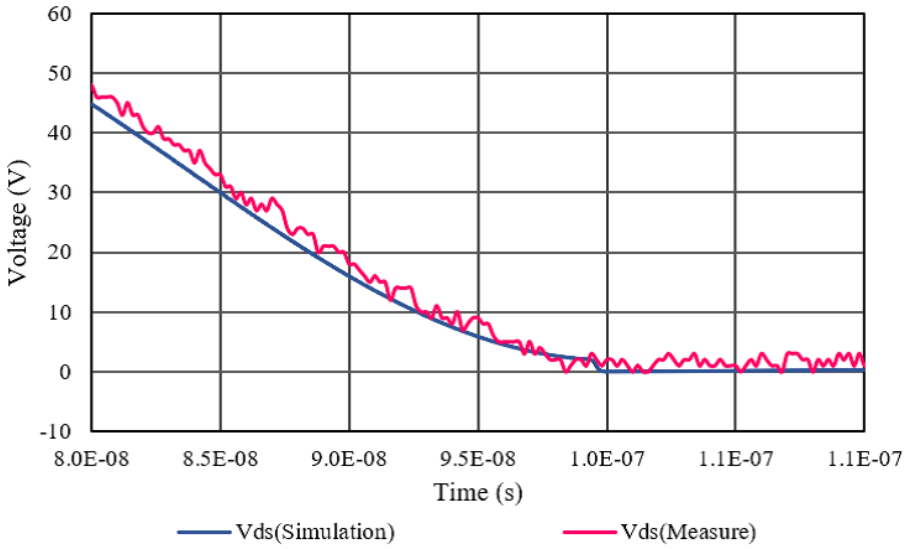

(a) Voltage time response of amplifier with Sample 1 at turn-on.

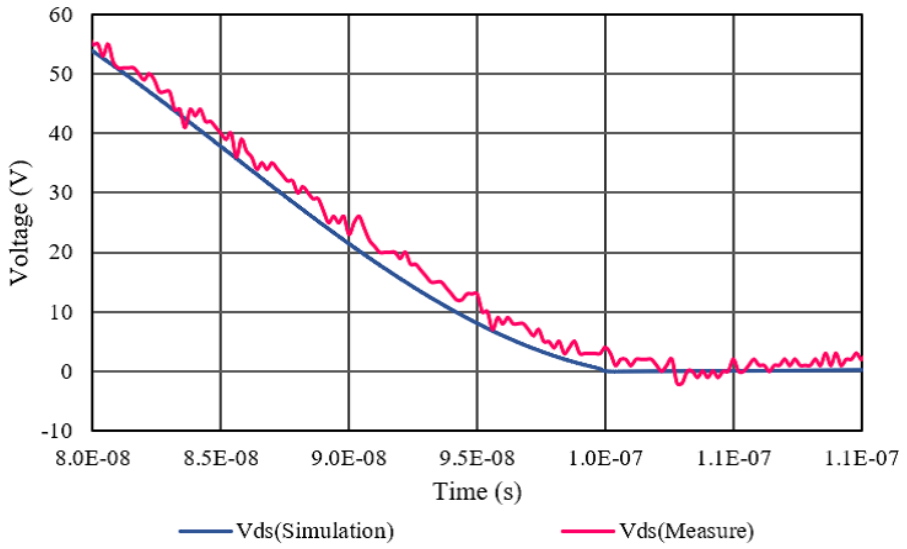

(b) Voltage time response of amplifier with Sample 2 at turn-on.

Figure 3.18 Voltage time responses at turn-on.

However, the peak value of the measured inductor current is higher than the simulation results for both Sample 1 and 2. In the simulations in this thesis, the switching device is assumed to be an ideal switch without parasitic capacitance. Actual switching devices have parasitic capacitances between drain-source and gate-drain[103][104].

This parasitic capacitance has a nonlinear characteristic with voltage dependency. In order to take these effects into account, a detailed device model is necessary to simulate the voltage dependency of the parasitic capacitance of the switching devices. In addition to the above, the duty ratio of the class-E amplifiers may not be exactly 50% in actual operation[105]. The switching transient time affects the drain-source voltage and drain current[106]. These factors cause the differences in time response between experiments and simulations.

3.5 Summary

This chapter evaluated and modeled the magnetic characteristics of inductors used in class-E amplifiers operating at frequencies above 10 MHz. The evaluation of magnetic characteristics by 2-port measurement of network analyzer was proposed. The modeling of magnetic components based on S-parameters and the extraction method of model parameters were shown. It was confirmed that the circuit analysis using the proposed model can simulate the soft-switching operation of class-E amplifiers in the circuit simulation. It was shown that the model is useful for application to the actual circuit design of high-frequency switching power converters.

However, some measured and simulated voltage time responses did not coincide. To simulate the operation of a class-E amplifier by circuit simulation, it was necessary to consider the characteristics of the power devices. The voltage dependency of power devices is considered in Chapter 5.

In addition, this chapter used toroidal cores for the evaluation. Toroidal cores are large in volume. Planar inductors and other types of inductors have been studied to achieve high power density in inductors for power conversion circuits[107][108]. These inductors were made of windings molded with a thin magnetic material. Planar inductors have problems of current unevenness in windings and magnetic flux concentration due to their shape. The method proposed in this study can be applied to the evaluation of magnetic properties and equivalent circuit modeling of planar inductors for high frequency power conversion.

Chapter 4

Evaluation and reduction of transient thermal resistance for β-Ga_2O_3 SBD

4.1 Introduction

β-Ga_2O_3 is expected for high voltage and high current power semiconductor devices due to wider bandgap than SiC and GaN. However, β-Ga_2O_3 has disadvantages compared to other wide bandgap semiconductors. High thermal resistance from junction to case limits forward current and power dissipation in the device. Hence, it is important to reduce the thermal resistance of gallium oxide. Nevertheless, there are few reports on the thermal properties of gallium oxide. For example, the thermal conductivity of β-Ga_2O_3 SBD with planar anode has been reported[82]. In spite that, the validity of estimated temperature with the device characteristics has not been evaluated.

This chapter measures transient thermal characteristics of β-Ga_2O_3 in accordance with JEDEC51-14[109]. This method extracts transient thermal resistance by time response of junction temperature in cooling operation from the self-heated thermal equilibrium of device[110][111]. Junction temperature is estimated from temperature dependency in forward conduction I-V characteristics in the low current range, where self-heating is negligible. This thesis shows transient thermal characteristics of β-Ga_2O_3 SBDs are measurable with good reproductively. This thesis evaluates the ideality of

processed Schottky junction with extracted ideal factor for two different anode type β-Ga_2O_3 SBDs.

This chapter considers the method to reduce transient thermal resistance of β-Ga_2O_3 SBDs. Enlargement of die size in β-Ga_2O_3 SBDs is difficult due to defect density in crystal. This chapter attempts to reduce thermal resistance by thinning SBD die. Thermal resistance is in proportion to length of heat dissipation path. This chapter compares β-Ga_2O_3 SBDs with different substrate thickness, and evaluated the effect of thinned substrate in reducing thermal resistance.

4.2 β-Ga_2O_3 SBDs under evaluation

This thesis adopts two different anode types for β-Ga_2O_3 SBDs. Planar type has flat Schottky junction at anode with molybdenum metal on n^- Ga_2O_3 drift layer as shown in Fig. 2.5. The molybdenum Schottky anode of MOS trench type is dielectrically isolated trench with hafnium oxide into n^- Ga_2O_3 drift layer as shown in Fig. 2.7.

Figure 4.1 shows a overview of β-Ga_2O_3 SBD. The die size is 1.80 mm $\times$ 1.34 mm with 0.25 mm thickness. The anode pad for wire-bonding on the SiO_2 layer is sided to the Schottky junction area. Planar and MOS trench types also have the same electrode design of chip surface. The developed SBDs are molded in the TO-220 package.

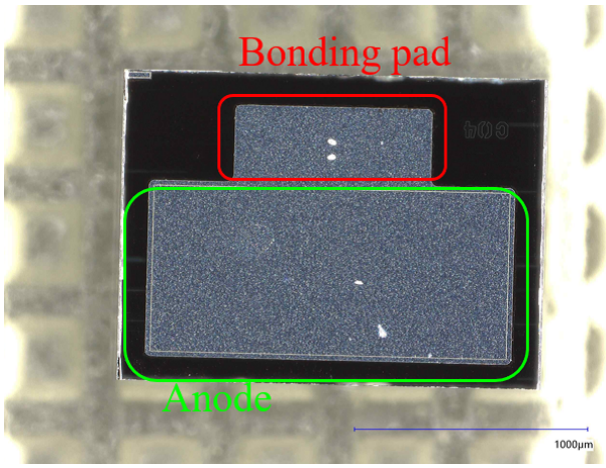

Figure 4.1 Overview of β-Ga_2O_3 SBD die.

4.3 Static characteristics of β-Ga_2O_3 SBDs

This section evaluates static characteristics and extracts parameters for β-Ga_2O_3 SBDs. Figure 4.2 shows forward conduction I-V characteristics at 25°C and 150°C measured with curve tracer(B1505A, Keysight technologies).

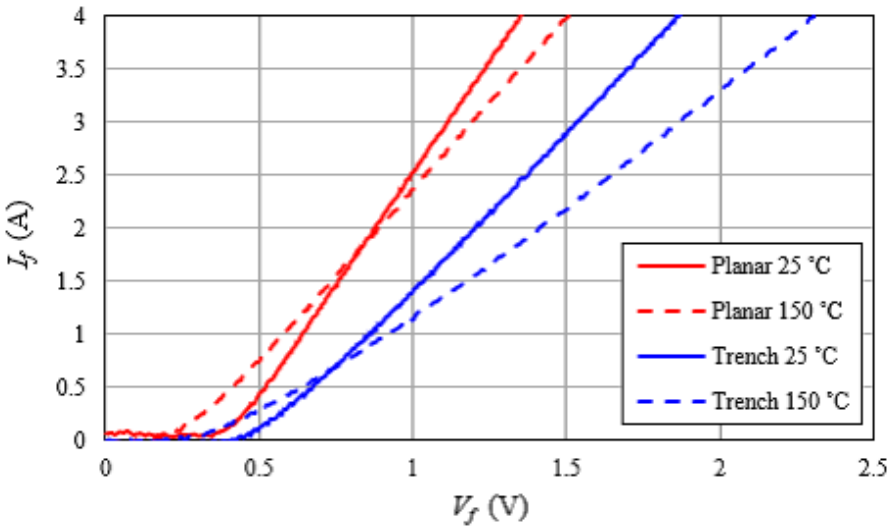

Figure 4.2 I_f-V_f characteristics of β-Ga_2O_3 SBDs in high current region.

The forward voltage drop of planar type is less than that of trench type. In high temperatures, the forward voltage drop in the high current region is higher than that in lower temperatures because of increased voltage drop on resistance.

This section evaluates Schottky junction aspects from forward conduction I-V characteristics in the low current region, where voltage drop at drift layer resistance is negligible. Figure 4.3 shows I_f-V_f characteristics of β-Ga_2O_3 SBDs in the low current region.

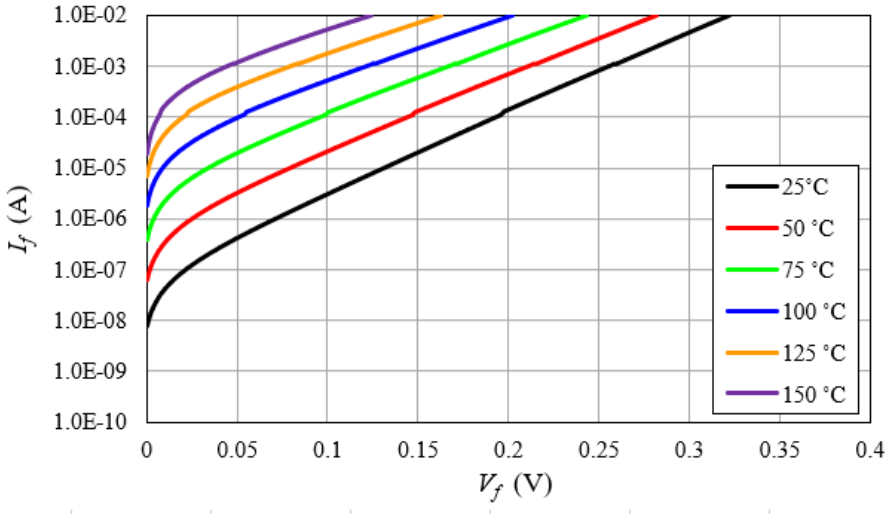

(a) I_f-V_f characteristics of planar type SBD.

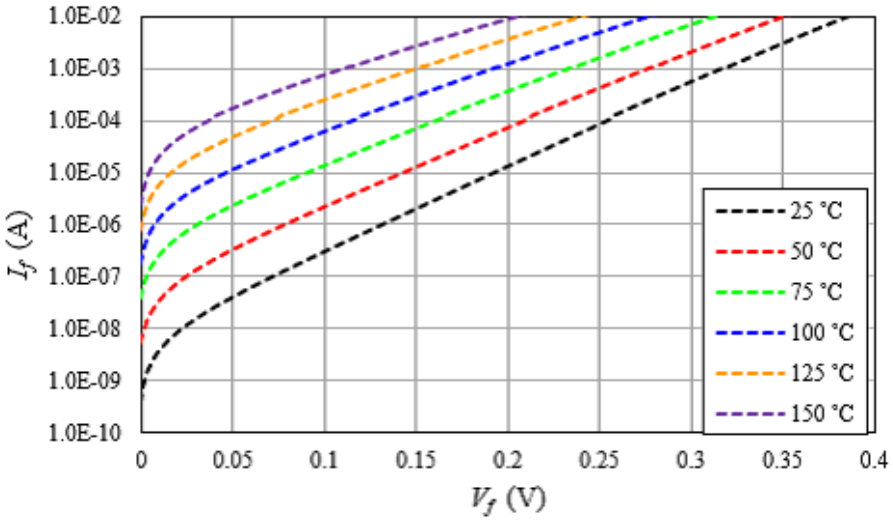

(b) I_f-V_f characteristics of trench type SBD.

Figure 4.3 I_f-V_f characteristics of β-Ga_2O_3 SBDs in low current region.

The relation between V_f and I_f in the low current region is expressed as Eq. 2.33 and Eq. 2.34.

This section evaluates the ideality of developed SBDs based on n and I_s. Error function E is defined as Eq. 4.1 to extract I_s and n. V_i, I_i are measured values shown in Fig. 4.3 and steepest descent method is applied for parameter extraction.

$$E = \sum_{i=1}^{l} \left[\log I_s + \log \left\{ \exp\left(\frac{eV_i}{nk_BT} \right) - 1 \right\} - \log I_i \right]^2 \tag{4.1}$$

This section uses $|\nabla E|$ in Eq. 4.2 to evaluate the convergence, and $10^{-6} < |\nabla E|$ is used for the convergence judgment.

$$|\nabla E| = \sqrt{\left(\frac{\partial E}{\partial m}\right)^2 + \left(\frac{\partial E}{\partial(\log I_s)}\right)^2} \tag{4.2}$$

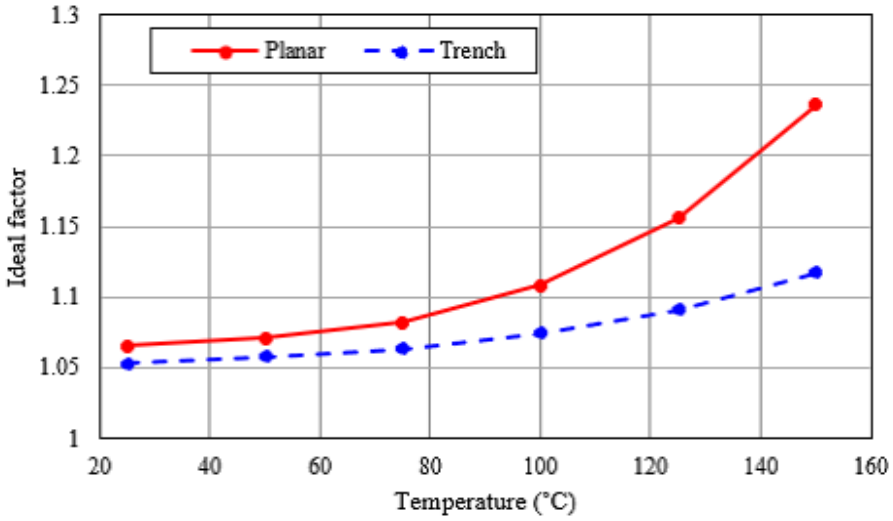

Figure 4.4 Extracted ideal factor n of β-Ga_2O_3 SBDs.

Figure 4.4 shows extracted ideal factors of each sample. The extracted ideal factors in Fig. 4.4 are lower than 1.1 in the temperature range below 80°C for each sample. However, the ideal factor is higher than 1.1 in the temperature range above 100°C. The deviation of the ideal factor from 1 indicates non-ideality of SBD characteristics. The extracted saturated currents are shown in Fig. 4.5.

Schottky barrier height in Eq. 2.34 is extracted from I_s in Fig. 4.5. Schottky barrier height of planar and trench type are 0.715 eV and 0.737 eV, respectively. The Schottky barrier height is expressed in Eq. 4.3, where Φ_m is the work function of Schottky metal, and χ_s is the electron affinity of semiconductors.

$$\Phi_B = \Phi_m - \chi_s \tag{4.3}$$

Electron affinity of β-Ga_2O_3 is reported at 3.5-4.0 eV[16][91]. The work function of molybdenum is 4.6 eV. Planar and trench type use the same Schottky metal. However, the Schottky barrier height of the planar type is lower than the trench type. This difference is estimated as the difference in the state of Schottky junction surface stemming from the MOS trench process.

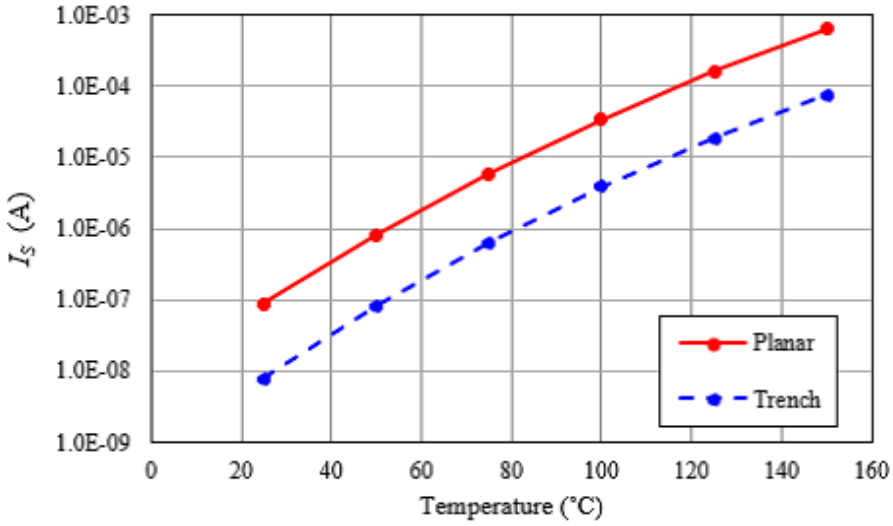

Figure 4.5 Extracted saturated current I_s of β-Ga_2O_3 SBDs.

Junction temperature is estimated from temperature dependency of forward voltage for low constant forward current. Eq. 4.4 is obtained from Eq. 2.33 providing that the variation of I_f for I_s is negligible.

$$\log\left(\frac{I_f}{I_s}+1\right)=\frac{eV_f}{nk_BT}=const \tag{4.4}$$

The relation between T and V_f is given as Eq. 4.5 from Eq. 4.4.

$$T=\frac{eV_f}{nk_B}\frac{1}{\frac{I_f}{I_s}} \tag{4.5}$$

In Eq. 4.5, the slope of T for V_f is called K factor. Junction temperature in cooling term for transient thermal characterization is estimated from V_f with K factor.

4.4 Extraction of transient thermal resistance for β-Ga_2O_3 SBDs

Section 4.3 shows that the quality of β-Ga_2O_3 SBD characteristics is secured. K factor is measured with temperature-controlled chamber. Measured temperature dependency of V_f for constant low current $I_f = 10$ mA is shown in Fig. 4.6. Figure 4.6 shows that temperature dependency of V_f is linear, and valid to estimate temperature from 25 to 125°C.

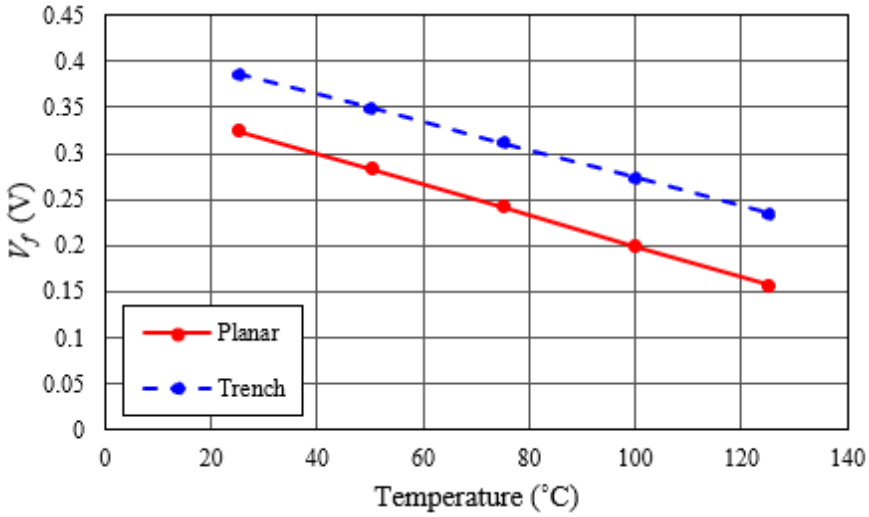

Figure 4.6 Temperature dependency of V_f(I_f =10 mA).

SBDs are self-heated with 1.0 A forward current for 60 seconds to achieve thermal equilibrium in heating conditions, then cooled by heat-sink for 200 seconds with shutting forward heating current. Junction temperature is measured with V_f for 10 mA forward current. Transient thermal characteristics are evaluated with and without thermal grease on the heat spreader of TO-220. Thermal resistance and thermal capacitance from junction to heat-sink are extracted from the difference of these two measurements. Figure 4.7 shows measured time responses of junction temperature for planar and trench type.

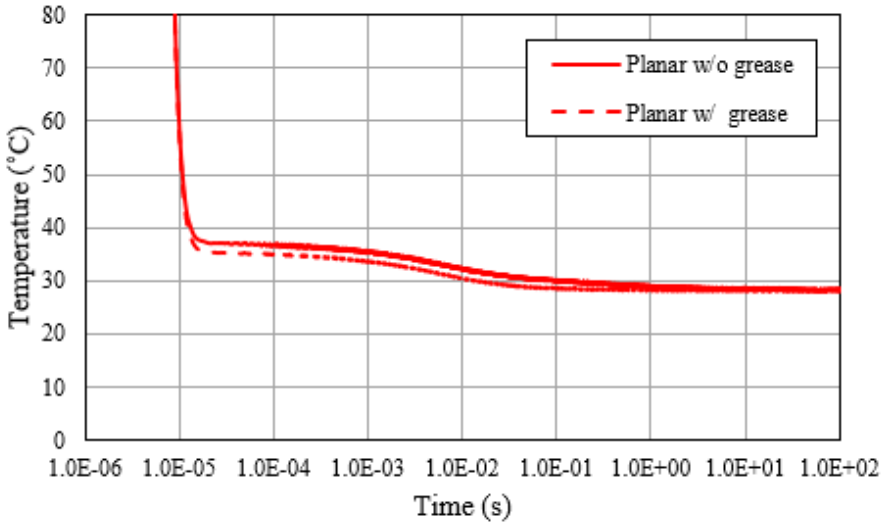

(a) Planar type.

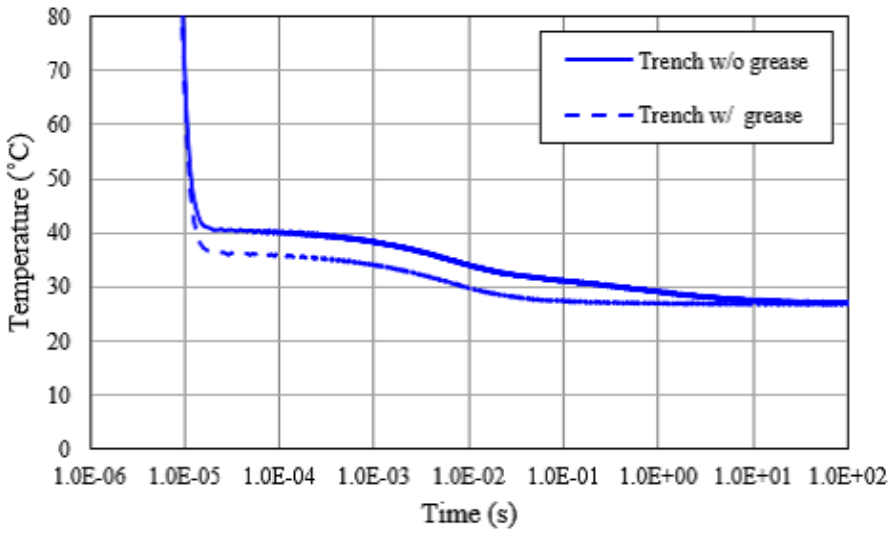

(b) Trench type.

Figure 4.7 Junction temperature time responses of β-Ga_2O_3 SBDs.

The measured temperature is uncertain for $t < 20$ μs, which stems from transient behavior in switching from heating to measuring current. Structure-functions are extracted from time response of junction temperatures for $t > 20$ μs in Fig. 4.7. Initial temperature is estimated by extrapolation with temperature for $t > 20$ μs.

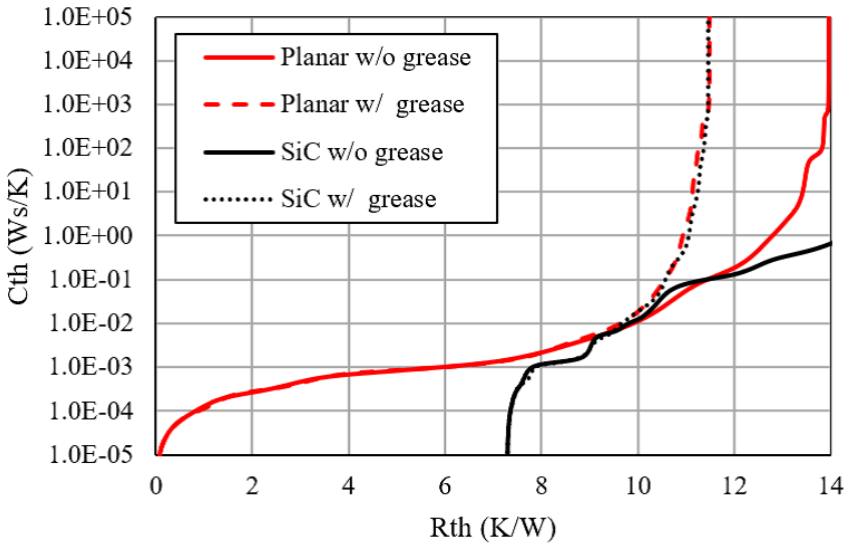

(a) Planar type.

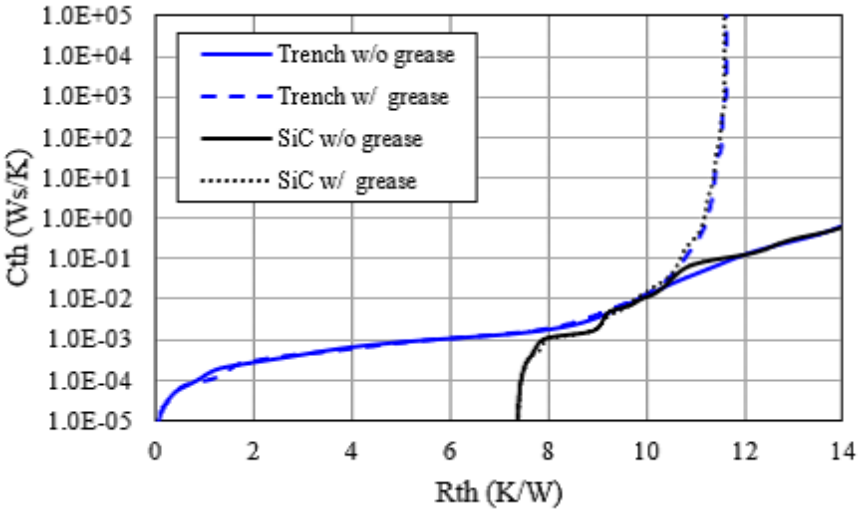

(b) Trench type.

Figure 4.8 Structure-function of β-Ga_2O_3 and SiC SBDs.

Structure-function in Fig. 4.8 shows thermal resistance and thermal capacitance from junction to heat-sink. The structure-function of SiC SBD(CPW3-0650-S004B, Cree) packaged in the same lead frame as β-Ga_2O_3 SBDs is plotted in Fig. 4.8 as reference. The consistent region with and without grease represents the heat spreading path from junction to heat spreader. The grease layer between heat spreader and heat-sink is located in the bifurcation point of w/ and w/o plots. The structure-functions

from die-attach to heat-sink of β-Ga_2O_3 SBDs with thermal grease almost coincide with that of SiC SBD. However, structure-functions of junction to die-attach make difference between β-Ga_2O_3 SBDs and SiC SBD. The bifurcation point of β-Ga_2O_3 SBD and SiC SBD with grease represent the difference of the thermal resistance form junction to die-attach. This difference is caused by the difference in thermal conductivity between β-Ga_2O_3 and SiC. Table 4.1 shows extracted thermal resistance and capacitance from junction to case with structure-function in Fig. 4.8.

Table 4.1 Extracted thermal resistance and capacitance.

R_{th}(junction to die-attach) (K/W)	Planar β-Ga_2O_3	9.0
	Trench β-Ga_2O_3	9.1
	SiC	1.7
R_{th}(junction to case) (K/W)	Planar β-Ga_2O_3	9.8
	Trench β-Ga_2O_3	10.0
	SiC	3.2
C_{th}(junction to case) (Ws/K)	Planar β-Ga_2O_3	1.3×10^{-2}
	Trench β-Ga_2O_3	1.5×10^{-2}
	SiC	4.0×10^{-2}

The die size of SiC SBD is 1.13 mm $\times$ 1.13 mm with 0.377 mm thickness. The thermal conductivity of SiC and β-Ga_2O_3 are 280 W/m·K and 13 to 21 W/m·K. The die area of β-Ga_2O_3 SBDs are 1.9 times larger than that of SiC SBD. The thickness of β-Ga_2O_3 is 34% thinner than that of SiC SBD. Considering thermal conductivity and geometric size, the thermal conductivity of β-Ga_2O_3 SBD is estimated to be 4.7 to 7.6 times higher than that of SiC SBD. Identified thermal resistances of junction to die-attach in Table 4.1 are in that range.

The preceding research estimated the thermal resistance of 2.3mm $\times$ 2.3mm planar β-Ga_2O_3 SBD is 5.9 K/W[63]. The size of tested β-Ga_2O_3 SBD dies are 1.80 mm $\times$ 1.34 mm, and the difference of the die size is considered to make the difference of thermal resistance. The thermal resistance of β-Ga_2O_3 is several times higher than SiC SBD, though the Ga_2O_3 dies have large net areas for side bonding pad. Heat radiation of β-Ga_2O_3 device is inferior to SiC or other wide bandgap semiconductor devices

due to high thermal resistance. Thermal resistance from junction to heat spreader is designed to be reduced for higher heat dissipation with high current density operation. Section 4.5 attempts to thin the thickness of β-Ga_2O_3 SBD to reduce thermal resistance.

4.5 Transient thermal resistance reduction by thinning substrate of a β-Ga_2O_3 SBD

This section evaluates transient thermal resistance of two β-Ga_2O_3 SBDs, whose thickness is different. They have 100 μm and 250 μm thickness n^+ β-Ga_2O_3 substrate layer as shown in Fig. 4.9.

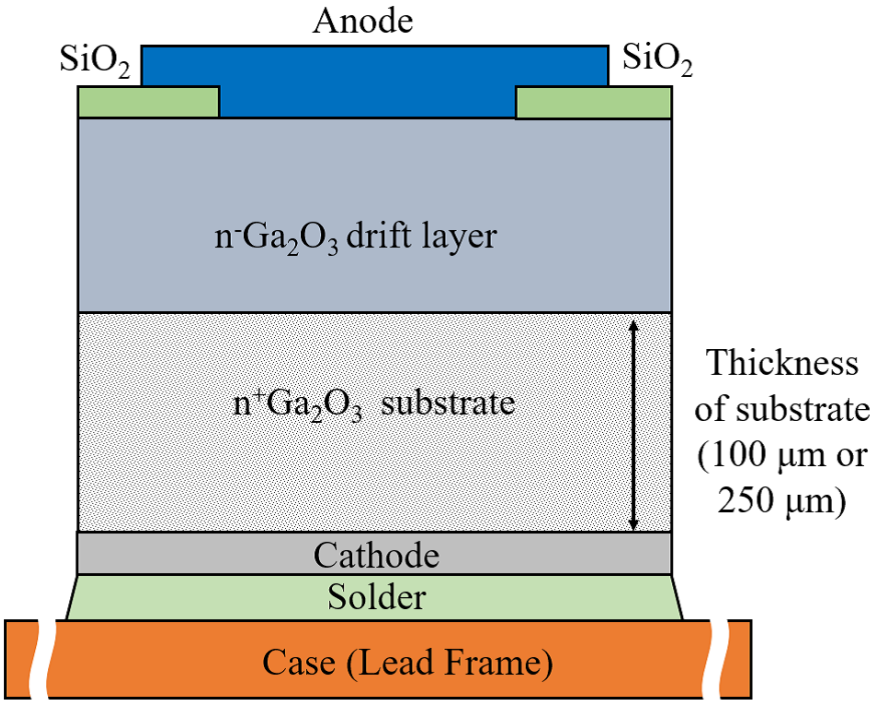

Figure 4.9 Cross section of β-Ga_2O_3 SBDs with different substrate thickness.

The die size is 1.80 mm × 1.34 mm. The total thicknesses of dies are 257 μm and 107 μm respectively for 250 μm and 100 μm substrate thickness diodes. Both SBDs have bonding pad beside anode electrode shown in Fig. 4.1. SBD dies are attached on lead frame and molded in TO-220 package.

The temperature dependency in forward voltage drop of two samples for 10 mA are

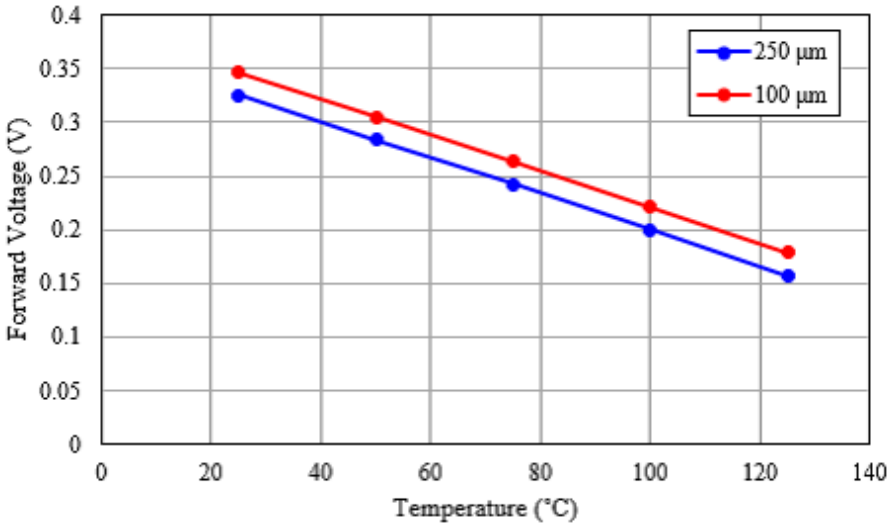

Figure 4.10 Temperature dependency in forward voltage drop of β-Ga_2O_3 with different thickness.

shown in Fig. 4.10. Measured results have almost linear characteristics. The difference between two devices is estimated to occur by the deviation from ideality of Schottky junction.

SBDs are self-heated with 1.5 A forward current for 60 s, then cooled by 25°C heat-sink for 200 s in transient thermal resistance characterization. 10 mA forward current is flowed to estimate junction temperature during cooling time. Structure-functions with and without thermal grease are extracted as shown in Fig. 4.11.

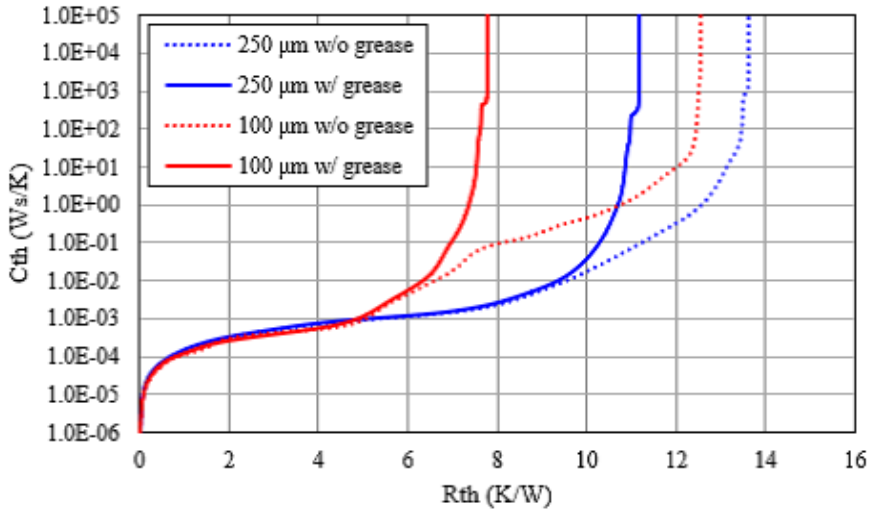

Figure 4.11 Structure-function of β-Ga_2O_3 with different thickness.

The bifurcation point at 5.0 K/W for 100 μm and 250 μm in Fig. 4.11 is estimated as the boundary of substrate layer and cathode electrode of SBD with 100 μm substrate. The grease layer between the heat spreader and the heat-sink corresponds to the bifurcation point of the structural function with and without grease. Transient thermal resistance of SBDs between junction to case are 6.1 K/W and 9.0 K/W respectively for 100 μm and 250 μm substrate layer thickness.

The difference in measured thermal resistance of β-Ga_2O_3 SBD with 100 μm and 250 μm substrate layer thickness is 2.9 K/W. Two samples are equivalent except for the thickness of substrate layer. The thermal resistance of 150 μm substrate layer is expected 2.9 K/W. This indicates that the thermal resistance of the100 μm and 250 μm substrate layers are 1.9 and 4.8 K/W, respectively. The thermal resistance of both samples, except for the substrate layer is 4.2 K/W. This thermal resistance includes the thermal resistance between junction to the drift layer, solder, lead frame, and interfacial thermal resistance of each layers.

Figure 4.11 shows the thermal resistance between junction to cathode electrode in SBD with 100 μm substrate layer is 5.0 K/W. Thus, thermal resistance between drift layer and substrate layer is 3.1 K/W. That is higher than thermal resistance between junction to the die-attach with equivalent size commercial SiC SBD. This result indicates that 100 μm substrate layer is not thin enough to dissipate heat. In addition to the substrate layer, the thermal resistance of the drift layer is also high even though the drift layer is less than 7 μm. Further reduction methodology of thermal resistance is needed for practical application of β-Ga_2O_3 SBDs.

4.6 Summary

This chapter extracted electrical and thermal parameters of β-Ga_2O_3 SBDs. The processed β-Ga_2O_3 SBDs showed almost ideal characteristics below 80°C. However, ideal factors of β-Ga_2O_3 SBDs in high temperature deteriorated. Improvement of the Schottky junction was key to improving SBD characteristics. Thermal resistance for the junction to heat spreader of β-Ga_2O_3 was higher than that of SiC and other semiconductors. The improvement of completeness of Schottky junction was needed for

practical β-Ga_2O_3 SBD performance.

The thermal resistance from junction to die-attach could be reduced to 2/3 by reducing the substrate thickness from 250 μm to 100 μm. However, thermal resistance of β-Ga_2O_3 SBD with 100 μm was higher than commercial SiC SBD. Not only substrate layer but also drift layer had high thermal resistance. Development of thermal resistance reduction structure is needed for practical application of β-Ga_2O_3 SBDs.

Chapter 5

Analysis and Design of class-E amplifier with nonlinear output capacitance model using sigmoid function for GaN HEMT

5.1 Introduction

The soft-switching technique is effective in reducing switching loss. Class-E amplifiers utilize soft-switching and are useful to suppress switching loss in MHz operation. Class-E amplifier operates with zero voltage switching(ZVS) and zero voltage derivative switching(ZVDS). The circuit operation of class-E amplifier with ideal components is analytically expressed in preceding researches[71]-[73].

The electrical characteristics of actual circuit components differ from the ideal. The output capacitance of power devices has nonlinear characteristics with respect to the applied bias voltage. Output capacitance of the transistor constitutes the resonant circuit of a class-E amplifier. Then, the nonlinearity of output capacitance of power devices affects class-E switching conditions. Higher frequency operation reduces the inductance and capacitance required for resonance, which increases the influence of device parasitic capacitance characteristics. Preceding researches analyzed the class-E

amplifiers taking the voltage dependency of output capacitance into consideration. The researches analyzed class-E amplifiers whose resonant capacitor consists only nonlinear capacitance of output capacitor in transistor[74]-[79]. Class-E amplifiers with linear and nonlinear capacitors were also analyzed[77]. Analyses of a class-DE amplifiers with nonlinear capacitance in the upper and lower arms for the half-bridge leg were reported in preceding researches[78][79].

However, these researches utilized vertical type power Si MOSFETs as switches and the abrupt junction model is utilized to express voltage dependency of output capacitance in vertical type power Si MOSFETs. The abrupt junction capacitance model cannot be directly applied to class-E amplifiers with GaN power devices. The lateral type GaN power devices require a dedicated model to simulate their output capacitance characteristics. Preceding research proposed physical model based on surface potential[80][81] and equivalent circuit models[82][83]. Physical models consist of a lot of parameters such as dimensional and process information. The complexity of the physical model makes circuit analysis and SPICE simulation difficult. Equivalent circuit models contain a current source and many circuit elements. It is difficult to use equivalent circuit models in circuit analysis for an analytical approach.

This thesis utilizes the sigmoid function as the voltage dependent output capacitance model for GaN power devices to analyze class-E amplifier with GaN power device. The sigmoid function capacitance model is used to simulate the behavior of GaN power devices[112][113]. Its parameters are expected to be easy to extract and accurately simulate GaN power device behavior. Preceding research with a sigmoid function model targeted to simulate static characteristics and switching behavior for hard-switching double pulse test in SPICE simulation[112]. There is no analysis of class-E soft-switching amplifiers with sigmoid function output capacitance model. The purpose of this thesis is to provide a circuit analysis and design methodology for class-E amplifiers with GaN HEMT whose output capacitance has nonlinear characteristics and is modeled by sigmoid function.

This chapter shows a circuit analysis of the class-E amplifier with the sigmoid function model. The design procedure of class-E amplifiers with the sigmoid function model is also discussed based on the circuit analysis. A class-E amplifier with the proposed

model is designed for above 10 MHz operation. The designed class-E amplifiers with GaN power devices are fabricated and experimented. The analytical results are validated with simulation and experiment. The proposed model would be helpful to the design of class-E amplifiers with GaN power devices.

5.2 Output capacitance model with sigmoid function

In preceding researches[74]-[79], voltage dependency of drain-source capacitance C_o was modeled with abrupt junction as Eq. 5.1, where C_{j0} is drain-source capacitance when drain-source voltage V_{ds} is zero. V_{bi} is built-in voltage.

$$C_o \approx \frac{C_{j0}}{\sqrt{1+\frac{V_{ds}}{V_{bi}}}} \tag{5.1}$$

And output charge Q_o is shown in Eq. 5.2.

$$Q_o \approx 2C_{j0}V_{bi}\left(\frac{V_{bi}+v_{ds}}{V_{bi}}-1\right) \tag{5.2}$$

This chapter adopts EPC8002 as a GaN power device. Output capacitance is a sum of drain-source capacitance and drain-gate capacitance. The drain-gate capacitance of EPC8002 is negligibly low compared to drain-source capacitance. The extracted C_{j0} and V_{bi} by the least mean square (LMS) are shown in Table 5.1.

The solid line in Fig. 5.1 shows drain-source voltage dependency of output capacitance in the datasheet. The abrupt junction model (dash-dotted line) does not match with datasheet value. V_{bi} of Si power MOSFET in preceding research is less than 1 V[74][76], which is determined by doping densities and bandgap. However, extracted V_{bi} in EPC8002 was significantly higher than Si MOSFET.

The model formulas based on device potential in preceding research consist of a lot of parameters. For example, Eq. 11 and Eq. 13 in [81] give the gate charge Q_g and drain charge Q_d. The sum of Q_g and Q_d is Q_o. The complexity of model formula makes parameter extraction and circuit analysis difficult. The simple formula for output capacitance is needed for designing class-E amplifiers.

Table 5.1 Extracted parameters of abrupt junction model and sigmoid function model.

Abrupt junction model	C_{j0}	1.5890×10^{-11}
	V_{bi}	9.1770
Sigmoid function model	a	17.466
	b	0.14949
	c	8.4122×10^{-12}
	d	1.4287×10^{-11}

Modified sigmoid function as Eq. 5.3 is adopted voltage dependent nonlinear output capacitance model of a GaN power device[112]. The parameters a, b, c and d in Eq. 5.3 are determined to fit C-V characteristics. They are easy to extract from the datasheet. This model consists of an empirical formula, then the precise knowledge of process parameters and geometry is not needed for modeling. Equation 5.3 can be differentiated and integrated analytically. The simplicity facilitates mathematical circuit analysis compared with physical based models composed with a lot of parameters.

$$C_o(v_{ds}) = \frac{-c}{1 + e^{-b(v_{ds}-a)}} + d \tag{5.3}$$

The dotted line in Fig. 5.1 shows the sigmoid model with extracted parameters in Eq. 5.3. The parameters a, b, c and d in Table 5.1 are extracted from datasheet value in Fig. 5.1 by the generalized reduced gradient method with minimizing the square error for Eq. 5.3.

The voltage dependency of output capacitance in EPC8002 is suitably expressed with the sigmoid function model as shown in Fig. 5.1. However, the sigmoid function model does not apply to all GaN power devices. The voltage dependency of output capacitance depends on device structure[114]-[117]. Preceding research has developed a variety of structures for GaN power device[118]-[120]. Some GaN power devices do not have inflection point ($d^2C_o(v_{ds})/dv_{ds}^2 = 0$) in the voltage dependency of output capacitance due to the device structures.

The sigmoid function model in Eq. 5.3 has an inflection point at $v_{ds} = a$ shown in Fig. 5.1. The sigmoid function model is not suitable for GaN power devices that have no inflection points in the voltage dependency of output capacitance as PGA26E19BA[121]

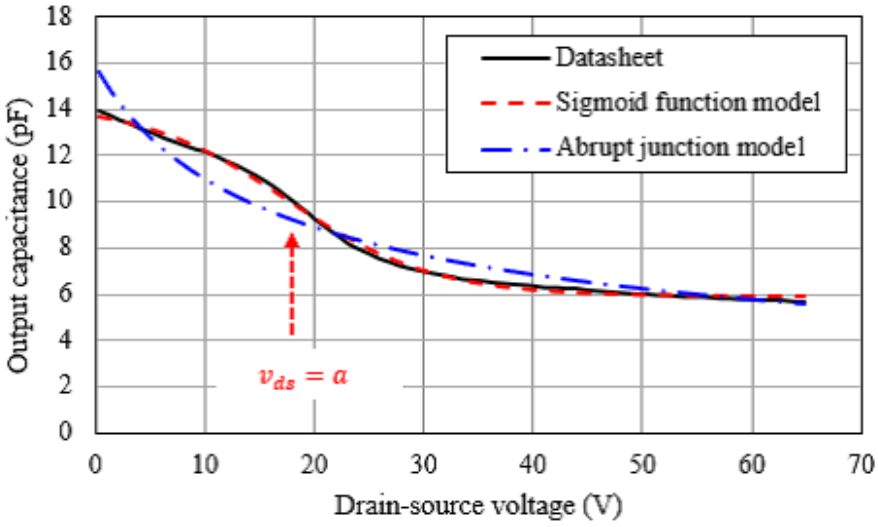

Figure 5.1 C-V characteristics of output capacitance for EPC8002.

and others[122].

5.3 Circuit analysis of a class-E amplifier using sigmoid function model

Figure 5.2 shows the circuit diagram of the class-E amplifier. C_o is the output capacitance of the power device. C_e is external capacitance to compensate for the lack of the capacitance required for resonance. Lumped elements except the power device are ideal. Circuit analysis for class-E operation is performed under the following assumption.

- It is assumed that the resonant circuit has ideal inductance L_t and capacitance C_t, whose Q factor is infinite. The output current i can be considered as a sinusoidal wave in the operating frequency.
- The inductance of choke inductor L_c is high enough to neglect current ripple in input current I_i and voltage drop for the equivalent series resistance is neglected.
- The forward and reverse I-V characteristics of the power device is neglected.

- Turn-on and turn-off of the power device is fast enough to neglect the transition time.
- In a periodic steady state, the power device is on when $0 < \theta \leq \pi$ and off when $\pi < \theta \leq 2\pi$. Note that θ is the phase angle of the switching period 2π.
- The C-V characteristics of output capacitance in power device is expressed as Eq. 5.3
- Switching (operating) frequency is the series resonant frequency of C_t and L_t.

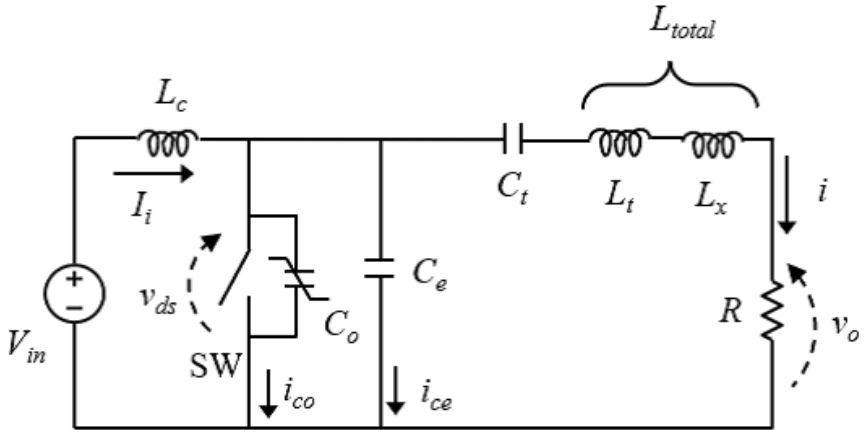

Figure 5.2 Circuit diagram of class-E amplifier.

The output current i is expressed as Eq. 5.4 with the amplitude of output current I_m and phase angle difference from θ is ϕ.

$$i = I_m \sin(\theta + \phi) \tag{5.4}$$

The current flowing into C_e and C_o is induced from Kirchhoff's current law as shown in Eq. 5.5.

$$i_{co} + i_{ce} = I_i - I_m \sin(\theta + \phi) \tag{5.5}$$

i_{co} and i_{ce} respectively charge C_e and C_o when the SW is off. Charge conservation during off period induces Eq. 5.6.

$$\int_{\pi}^{2\pi} i_{co} + i_{ce}\ d\theta = \omega \int_{v_{ds}(\pi)}^{v_{ds}(2\pi)} C_e + C_o\left(v_{ds}(\theta)\right)\ dv_{ds}(\theta) \tag{5.6}$$

The output charge Q_o is obtained from the integration of Eq. 5.3 by drain-source voltage as Eq. 5.7.

$$\begin{aligned} Q_o &= \int_0^{v_{ds}(\theta)} C_o \, dv_{ds}(\theta) \\ &= (d-c)\, v_{ds}(\theta) - \omega \frac{c}{b} \log\left(e^{b(a-v_{ds}(\theta))}+1\right) \\ &+ \omega \frac{c}{b} \log\left(e^{ab}+1\right) \end{aligned} \tag{5.7}$$

Substituting Eq. 5.7 and Eq. 5.5 into Eq. 5.6 yields Eq. 5.8.

$$\begin{aligned} &\omega\left(d+C_e-c\right) v_{ds}(\theta) - \omega\tfrac{c}{b} \log\left(e^{b(a-v_{ds}(\theta))}+1\right) \\ &\qquad +\omega\tfrac{c}{b} \log\left(e^{ab}+1\right) \\ &= I_i(\theta-\pi) + I_m\left[\cos(\theta+\phi)+\cos\phi\right] \end{aligned} \tag{5.8}$$

Equation 5.8 is not analytically solvable for $v_{ds}(\theta)$. Then, Equation 5.8 is approximated with second order polynomial equation as Eq. 5.9 by Maclaurin expansion.

$$\begin{aligned} &\omega\left(d+C_e-c\right) v_{ds}(\theta) + \omega\tfrac{c}{b} \log\left(e^{ab}+1\right) \\ &-\omega\tfrac{c}{b}\left\{\log\left(e^{ab}+1\right) - \tfrac{be^{ab}}{e^{ab}+1} v_{ds}(\theta) + \tfrac{b^2 e^{ab}}{2(e^{ab}+1)^2} v_{ds}^2(\theta)\right\} \\ &= \omega\left\{(d+C_e-c) + \tfrac{ce^{ab}}{e^{ab}+1}\right\} v_{ds}(\theta) - \tfrac{\omega bce^{ab}}{2(e^{ab}+1)^2} v_{ds}^2(\theta) \\ &\approx I_i(\theta-\pi) + I_m\left[\cos(\theta+\phi)+\cos\phi\right] \end{aligned} \tag{5.9}$$

Equation 5.9 is approximated as Eq. 5.10.

$$\alpha v_{ds}^2(\theta) + \beta v_{ds}(\theta) - g(\theta) = 0 \tag{5.10}$$

α, β, and $g(\theta)$ are expressed as the following equations.

$$\begin{aligned} \alpha &= -\frac{\omega bce^{ab}}{2(e^{ab}+1)^2} \\ \beta &= \omega\left\{(d+C_e-c) + \frac{ce^{ab}}{e^{ab}+1}\right\} \\ g(\theta) &= I_i(\theta-\pi) + I_m\left[\cos(\theta+\phi)+\cos\phi\right] \end{aligned}$$

v_{ds} is obtained as Eq. 5.11 by solving Eq. 5.10 for the constrain $v_{ds} \geq 0$.

$$v_{ds}(\theta) = \frac{-\beta + \sqrt{\beta^2 + 4\alpha g(\theta)}}{2\alpha} \tag{5.11}$$

5.3.1 ZVS condition

The zero voltage switching condition is given as $v_{ds}(2\pi) = 0$. Then, Eq. 5.11 yields Eq. 5.12.

$$g(2\pi) = I_i(2\pi - \pi) + I_m\left[\cos(2\pi + \phi) + \cos\phi\right] = 0 \tag{5.12}$$

Finally, ZVS condition is given as Eq. 5.13.

$$I_i = -I_m\frac{2cos\phi}{\pi} \tag{5.13}$$

5.3.2 ZVDS condition

The condition of zero voltage derivative switching is $dv_{ds}(2\pi)/d\theta = 0$. The derivative of Eq. 5.11 yields ZVDS condition as shown in Eq. 5.14.

$$\frac{d}{d\theta}v_{ds}(\theta)\bigg|_{\theta=2\pi} = \frac{1}{2\sqrt{4\alpha g(\theta) + \beta^2}}g'(\theta)\bigg|_{\theta=2\pi} = 0 \tag{5.14}$$

ZVDS condition is obtained from Eq. 5.14 and Eq. 5.13 as Eq. 5.15.

$$\begin{aligned} g'(2\pi) &= -I_m\frac{2\cos\phi}{\pi} - I_m\sin(2\pi + \phi) \\ &= 0 \end{aligned} \tag{5.15}$$

Solving Eq. 5.15 yields ZVDS condition shown in Eq. 5.16.

$$\tan\phi = -\frac{2}{\pi} \tag{5.16}$$

5.3.3 Derivation of passive component parameters

Input power to class-E amplifier is equal to output power in the load resistance$R$ when conversion loss is zero.

$$I_iV_{in} = \frac{I_m^2R}{2} \tag{5.17}$$

Solving Eq. 5.13 and Eq. 5.17 yields I_m and I_i shown in Eq. 5.18 and Eq. 5.19.

$$I_m = -\frac{4\cos\phi}{\pi R}V_{in} \tag{5.18}$$

$$I_i = \frac{8\cos^2\phi}{\pi^2 R}V_{in} \tag{5.19}$$

The averaged drain-source voltage in one switching period corresponds with input DC voltage. The relation between V_{in} and $v_{ds}(\theta)$ is shown in Eq. 5.20.

$$\begin{aligned} V_{in} &= \frac{1}{2\pi}\int_0^{2\pi} v_{ds}(\theta)\ d\theta \\ &= \frac{1}{4\pi\alpha}\left[-\beta\pi + \int_\pi^{2\pi} \sqrt{\beta^2 + 4\alpha g(\theta)}\ d\theta\right] \end{aligned} \tag{5.20}$$

The right hand side of Eq. 5.20 is not analytically obtainable. Then, numerical integration and iterative calculation find C_e satisfying Eq. 5.20. This means that V_{in}, f, R and extracted a, b, c, d determine C_e.

Drain-source voltage $v_{ds}(\theta)$ is the sum of voltage in series resonant L-C filter and output voltage $v_o(\theta)$ in load resistance. The synthesized impedance of the series connected C_t and L_t at the resonant frequency is zero. Then, the sum of voltage across L_x and output voltage $v_o(\theta)$ at operating frequency is expressed as $v_{s1}(\theta)$ in Eq. 5.21, where $v_{Lx1}(\theta)$ is operating frequency component of voltage across L_x and V_o is amplitude of output voltage.

$$\begin{aligned} v_{s1}(\theta) &= v_o(\theta) + v_{Lx1}(\theta) \\ &= V_o\sin(\theta+\phi) + \frac{V_o\omega L_x}{R}\cos(\theta+\phi) \\ &= V_1\sin(\theta+\phi+\psi) \end{aligned} \tag{5.21}$$

V_1 is expressed in Eq. 5.22 by using V_o.

$$V_1 = V_o\sqrt{1+\left(\frac{\omega L_x}{R}\right)^2} \tag{5.22}$$

$v_{s1}(\theta)$ is expressed as sinusoidal wave and its phase difference from θ is $\phi+\psi$. $v_{s1}(\theta)$ is the fundamental component of $v_{ds}(\theta)$ at operating frequency. This thesis assumes that Q factor of C_t and L_t filter is infinite. Though drain-source voltage contains harmonic components, harmonic voltage applied to L-C filter does not flow harmonic current.

$v_{s1}(\theta)$ dose not have cosine component as shown in Eq. 5.23.

$$\begin{aligned} & \frac{1}{\pi}\int_0^{2\pi} v_{ds}(\theta)\cos(\theta+\phi+\psi)\ d\theta \\ = & \frac{1}{\pi}\int_0^{2\pi} v_{ds}(\theta)\cos(\theta)\cos(\phi+\psi)d\theta - \frac{1}{\pi}\int_0^{2\pi} v_{ds}(\theta)\sin(\theta)\sin(\phi+\psi)d\theta \\ = & \ 0 \end{aligned} \tag{5.23}$$

Transformation of Eq. 5.23 for constant $\phi + \psi$ yields Eq. 5.24.

$$\frac{\sin(\phi+\psi)}{\cos(\phi+\psi)} = \tan(\phi+\psi) = \frac{\int_{\pi}^{2\pi} v_{ds}(\theta)\cos(\theta)\ d\theta}{\int_{\pi}^{2\pi} v_{ds}(\theta)\sin(\theta)\ d\theta} \tag{5.24}$$

$v_{ds}(\theta)$ is obtainable when C_e is determined from Eq. 5.20. Equation 5.11 and Equation 5.24 yields $\tan(\phi+\psi)$. $\tan\psi$ is obtained by Eq. 5.24 and Eq. 5.16. L_x is obtained as Eq. 5.25.

$$L_x = \frac{R\tan\psi}{\omega} \tag{5.25}$$

The total Q factor for class-E amplifier is given in Eq. 5.26 as the design parameter.

$$Q = \frac{\omega(L_t + L_x)}{R} \tag{5.26}$$

L_x in Eq. 5.26 is given by Eq. 5.25. C_t is obtained from Eq. 5.27 with operating frequency.

$$C_t = \frac{1}{\omega(RQ - \omega L_x)} \tag{5.27}$$

Preceding research[73] shows that the inductance L_c to obtain the peak-to-peak current ripple less than 10% of input DC current I_i is given as Eq. 5.28.

$$L_c > 2\left(\frac{\pi^2}{4} + 1\right)\frac{R}{f} \simeq \frac{7R}{f} \tag{5.28}$$

5.4 Class-E amplifier designs to verify the analysis using sigmoid function model

5.4.1 Class-E amplifier design procedure using sigmoid function model

Section 5.3 presents circuit analysis of class-E amplifier with the sigmoid function output capacitance model for GaN power device. The design procedure of class-E amplifiers can be simplified by giving design parameters. The design flowchart of determining circuit parameters in Fig. 5.2 is shown in Fig. 5.3.

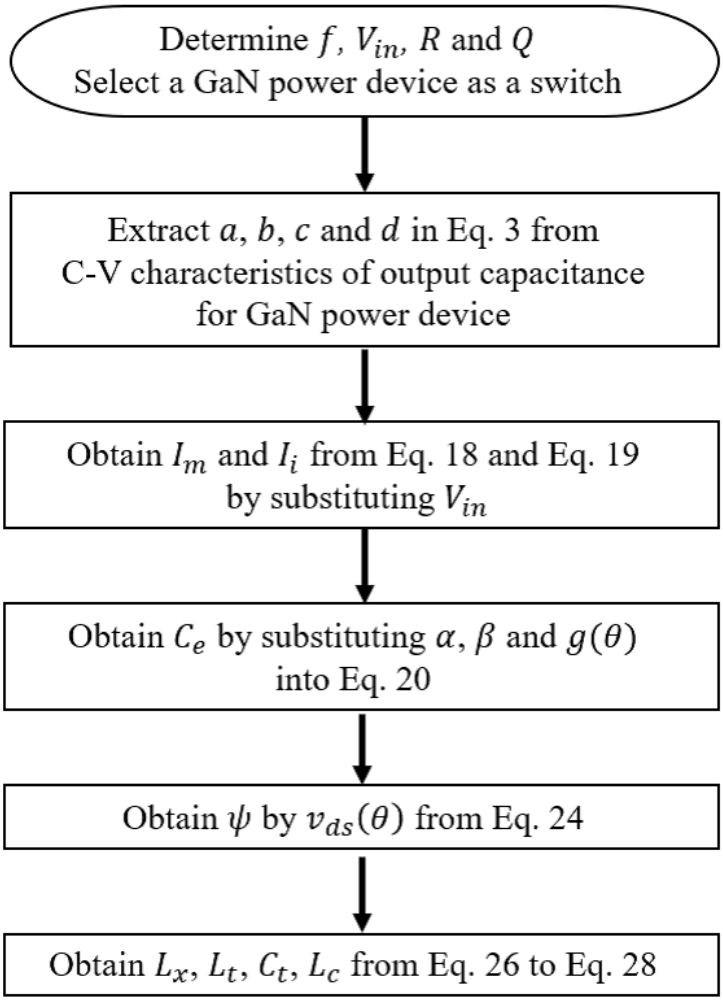

Figure 5.3 Design flowchart of a class-E amplifier with the sigmoid function model.

The next section shows the designed circuit parameters for experiments in this thesis.

5.4.2 The designed class-E amplifiers with proposed method

This section presents two design examples whose operating frequencies are different. They were set as 27.12 MHz and 40.68MHz to verify the circuit operation and to compare simulation results in different operating frequencies.

Each parameter is calculated with the design procedure in Sect. 5.4.1. EPC8002 shown in Sect. 5.2 is adopted as a switch. Trapezoidal rule integration is utilized to solve Eq. 5.20. The input voltage is set to 5 V. Load resistance R and Q are set to

12.5 Ω and 10 respectively. The design parameters derived from these assumptions are shown in Table 5.2. Series connected inductors L_t and L_x are consolidated into one component as L_{total}.

Table 5.2 Designed parameters of class-E amplifiers.

Frequency (MHz)	27.12		40.68	
	designed	fabricated	designed	fabricated
$L_c(\mu\text{H})$	3.2	15	2.2	10
L_t (nH)	649	680	433	475
L_x (nH)	85	88	56	58
L_{total} (nH)	649	768	489	533
r_L(series) (Ω)		0.42		0.40
R_L(parallel) (kΩ)		79		41
c_L (Ω)		1.15		1.22
C_t (pF)	53	50	35	32
C_e(total) (pF)	73	72	44	42
C_e(chip) (pF)		60		30
C_e(board) (pF)		12		12
R (Ω)	12.5	12.5	12.5	12.5
P_{out} (W)	1.15	1.12	1.15	1.12

Preceding research[74] shows circuit analysis of class-E amplifier with abrupt junction nonlinear capacitance of power device C_o and linear external capacitance C_e. $v_{ds}(\theta)$ is expressed as Eq. 5.29 in preceding research.

$$v_{ds}(\theta) = 2gV_{bi}\left[g + h(\theta) - \sqrt{g^2 + 2gh(\theta) + 1}\right] \tag{5.29}$$

$h(\theta)$ and g are expressed as the following equations.

$$\begin{aligned} h(\theta) &= \frac{I_i\theta + I_m\left[\cos(\theta+\phi) - \cos\phi\right]}{2\omega C_{j0}V_{bi}} + 1 \\ g &= \frac{C_{j0}}{C_e} \end{aligned}$$

Calculated $v_{ds}(2\pi)$ from Eq. 5.29 are $-32.83 - j6.49$ V for 27.12 MHz and $-20.26 - j4.31$ V for 40.68 MHz. Circuit analysis with abrupt junction model yields complex $v_{ds}(\theta)$.

This is caused by the difference of V_{bi} between Si MOSFET and GaN HEMT. Class-E switching condition derivation procedure in preceding research is not adaptable with EPC8002 abrupt junction model.

The voltage and current time responses are calculated with parameters in Table 5.2 and equations in Sect. 5.3. The calculated results are verified in Sect. 5.5.

5.5 Simulation and experimental results

5.5.1 Fabrication of actual circuits

This section fabricates the circuits based on the design of Table 5.2. L_{total} in two designs are air-core toroidal inductors to prevent core loss. Air-core inductors are larger in volume but easier to model. The main focus of this section is on the verification of the circuit analysis in Sect. 5.3. Inductance L_{total}, equivalent series resistance r_L, equivalent parallel resistance R_L and wiring capacitance c_L are shown in Table 5.2. L_{total} and r_L are measured at their operating frequency with impedance analyzer(E4991B, Keysight Technologies). c_L is obtained from self-resonant frequency of the toroidal inductor. R_L is the impedance of the toroidal inductor at self-resonant frequency. r_L is connected in series with load R and L_{total}. This thesis consolidates R and r_L into one resistor. As the effective R increases, the Q factors change to the value in Table 5.2. However, analysis in Sect. 5.3 neglects c_L and R_L. The effect of c_L and R_L is considered later in this section.

C_e and C_t in Table 5.2 are multilayer ceramic capacitor(ATC 600F series, KYOCERA AVX). This series of capacitor has NP0 characteristic and can be used as linear capacitors. ESR and voltage dependency in the capacitors are negligibly small.

Passive components are mounted on a printed circuit board. The printed circuit board has thin copper film as the wiring conductor. EPC8002 has a ball grid allay package, which radiates heat to the copper pattern of the print circuit board. The drain and source electrode face top side to bottom side and are considered as a parallel plate capacitor. The drain and source areas are large and their capacitance affects circuit operation. This thesis regards drain-source board parasitic capacitance as linear capacitance parallel to the output capacitance of EPC8002. The drain-source parasitic

capacitance of wiring is 12 pF measured with an impedance analyzer(E4991B, Keysight Technologies).

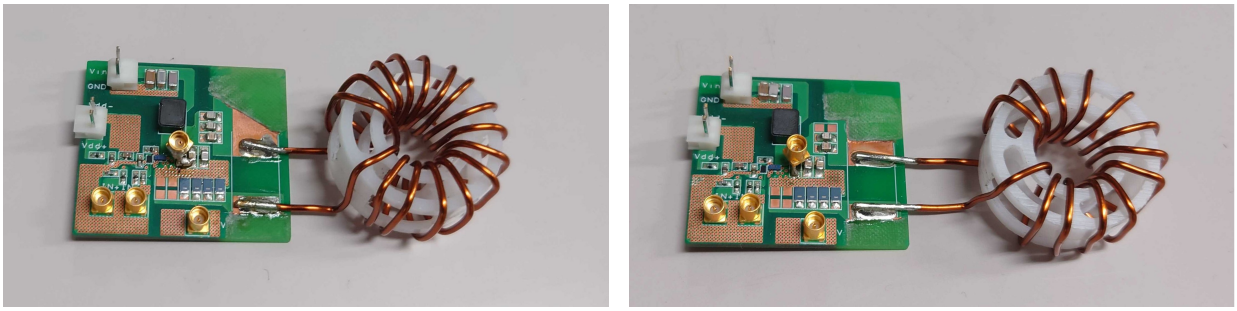

(a) 27.12 MHz operation. (b) 40.68 MHz operation.

Figure 5.4 Overview of class-E amplifiers for output capacitance model verification.

Figure 5.4 shows a fabricated class-E amplifier whose switching operating frequency is 27.12 MHz and 40.68 MHz. Both class-E amplifiers use the same printed circuit board. The class-E amplifier driven 27.12 MHz is 34 mm in width, 72 mm in length, and 20 mm in height. The class-E amplifier driven 40.68 MHz is 34 mm in width, 80 mm in length, and 20 mm in height. These have a higher driven frequency but larger dimensions than those shown in Fig 3.14. This is due to the larger volume of the air-core inductors used. Hence, the use of magnetic materials is effective for miniaturization of circuits.

This thesis verifies the mathematical analysis results by simulation and experiments with actual circuits.

5.5.2 Simulation and experimental results

Spice simulation is conducted with LTspice (Analog Devices). The passive components in LTspice are modeled as linear time-invariant elements including parasitic components in Table 5.2. The EPC8002 model is modified from the one provided by the device manufacturer (EPC). In the modification, the gate-drain capacitance is neglected. Two models of voltage dependency for drain-source capacitance are utilized, which are Sim(Sigmoid) with Eq. 5.7 and Sim(Abrupt) with Eq. 5.2. This chapter conducts circuit simulations with and without considering c_L and R_L.

Oscilloscope (MSO58, Tektronix) is used for experimental measurement. Drain-source voltage is measured with an optically isolated probe (TIVH08, Tektronix). Output voltage is measured with a passive probe (TPP1000, Tektronix).

Circuit analysis shown in Sect. 5.3 does not consider c_L and R_L. Figure 5.5(a) to Figure 5.6(b) shows experimental results and LTspice simulation without c_L and R_L. LTspice simulations with abrupt junction models for both operating frequencies do not converge due to the limitation of variable time step in LTspice. The abrupt junction model is not suitable for GaN HEMT used in this study. Circuit simulations with the sigmoid function model converge and simulated results of V_{ds} coincide with calculated and experimental results.

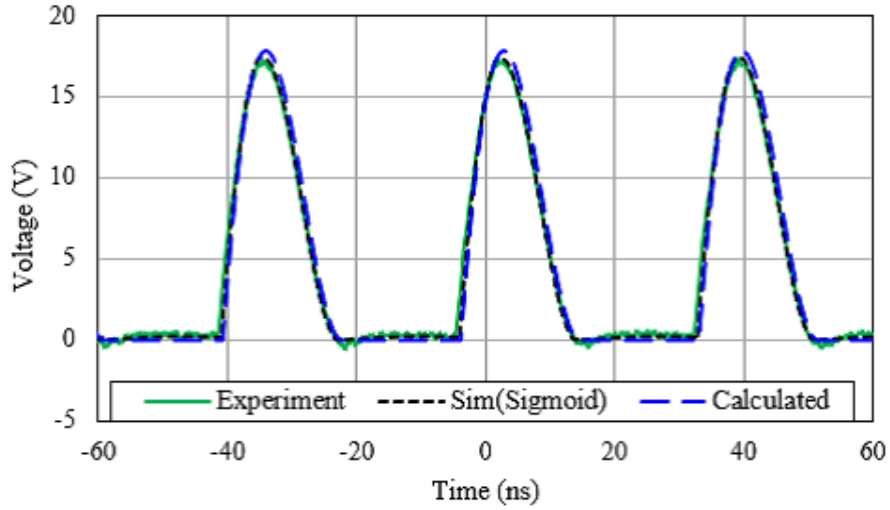

(a) Drain-source voltage.

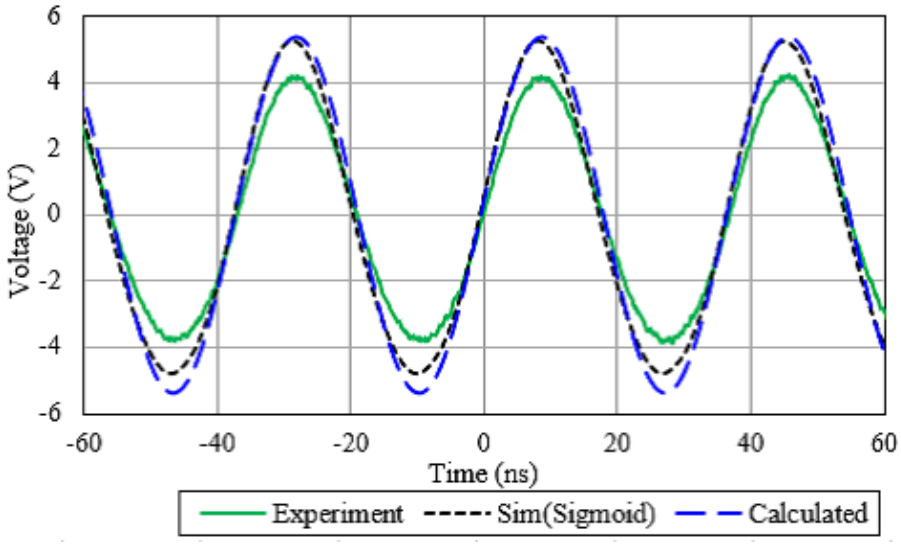

(b) Output voltage.

Figure 5.5 Experimental, simulated and calculated time response in 27.12 MHz class-E amplifier without considering c_L and R_L.

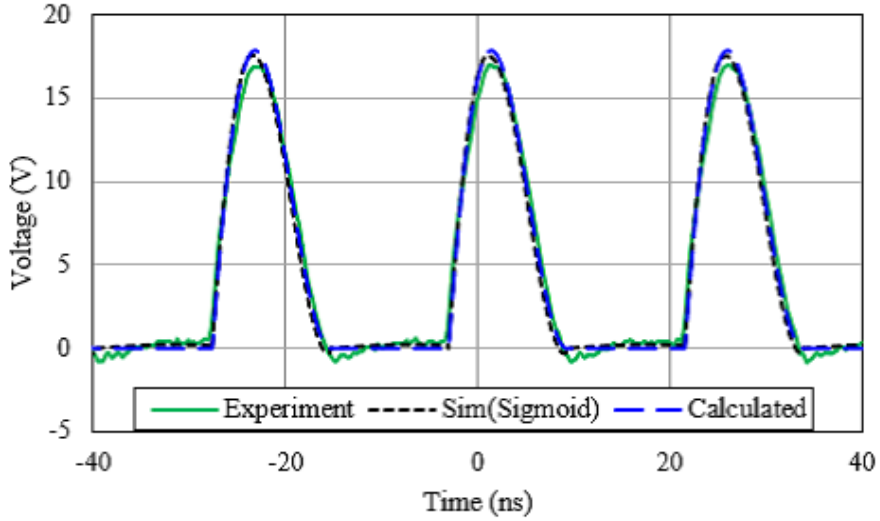

(a) Drain-source voltage.

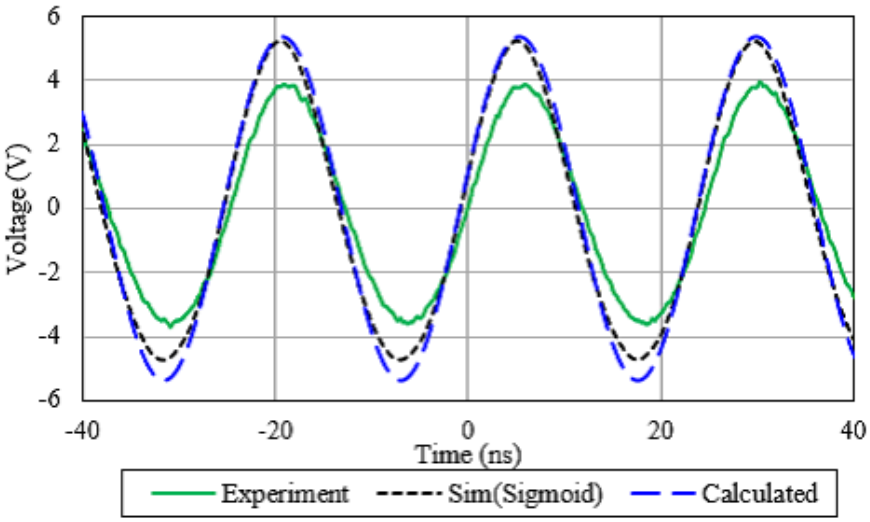

(b) Output voltage.

Figure 5.6 Experimental, simulated and calculated time response in 40.68 MHz class-E amplifier without considering c_L and R_L.

Drain-source voltage of experiment, simulation and calculation in Fig. 5.5(a) and Fig. 5.6(a) coincide. Simulated V_{ds} time response in 27.12 and 40.68 MHz achieves class-E switching regardless of considering c_L and R_L. The calculated time responses with proposed method match to simulated and experimental results. Then, the analysis in Sect. 5.3 is able to derive class-E the switching conditions.

Figure 5.5(b) and Figure 5.6(b) show the output voltage of class-E power am-

plifiers with 27.12 MHz and 40.68 MHz operation. Sim(Sigmoid) and Calculated in Fig. 5.5(b) and Fig. 5.6(b) coincide in positive voltage range. In the negative voltage range, Sim(Sigmoid) and Calculated do not coincide because the proposed circuit analysis assumes the power device without on-resistance. The actual power device has forward and reverse I-V characteristics. Voltage drop at the power device causes the differences between Sim(Sigmoid) and Calculated. The output voltage amplitude of Experiment in Fig. 5.5(b) and Fig. 5.6(b) is small compared to Sim(Sigmoid) and Calculated. The positive peak voltage of the Experiment is 20% lower than Sim(Sigmoid) and Calculated in Fig. 5.5(b). The difference of peak voltage in Fig. 5.6(b) is 25%. That difference is caused by the c_L and R_L in the actual circuit. The higher the operating frequency becomes, the more significant the parasitic component affects. Consideration of c_L and R_L is needed for accurate simulation of output voltage as considered in Chapter 3.

This thesis conducts simulations taking parasitic components into consideration. c_L and R_L in Table 5.2 are contained in Fig. 5.7(a) to Fig. 5.8(b). Experimental time response in Fig. 5.7(a) to Fig. 5.8(b) is the same as Fig. 5.5(a) to Fig. 5.6(b).

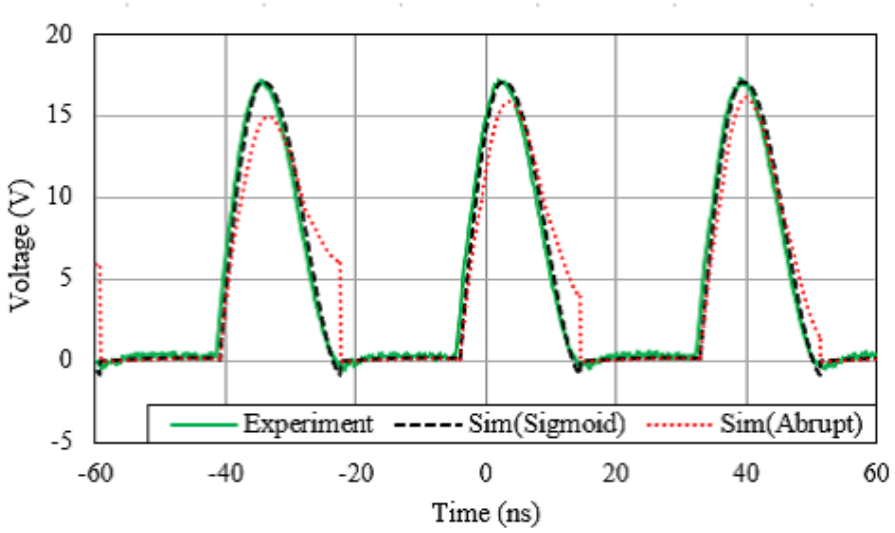

(a) Drain-source voltage.

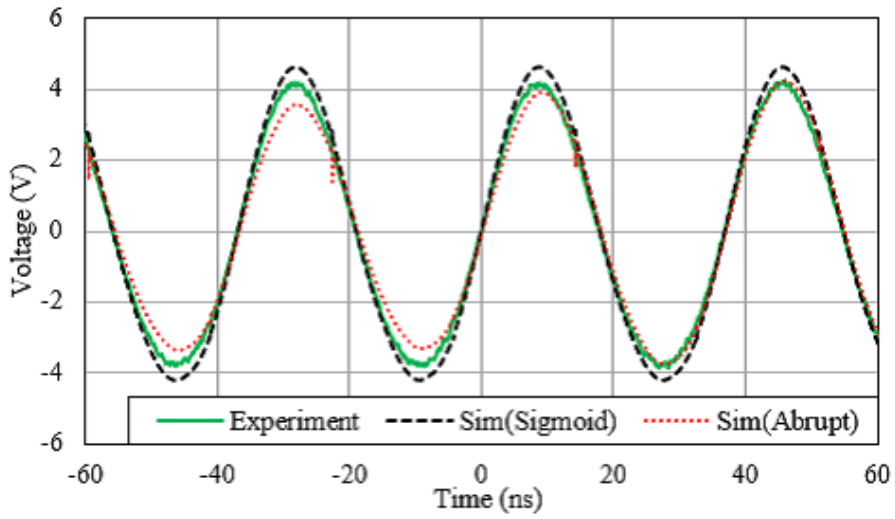

(b) Output voltage.

Figure 5.7 Experimental, simulated and calculated time response in 27.12 MHz class-E amplifier with considering c_L and R_L.

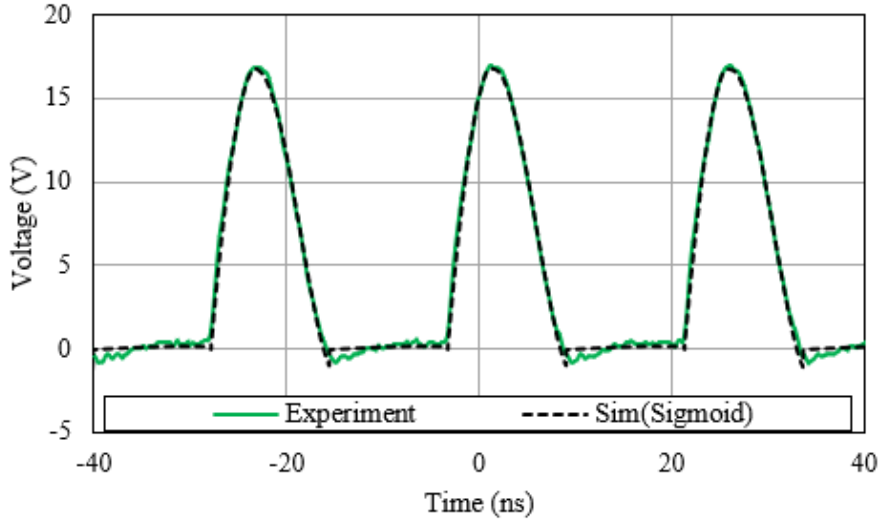

(a) Drain-source voltage.

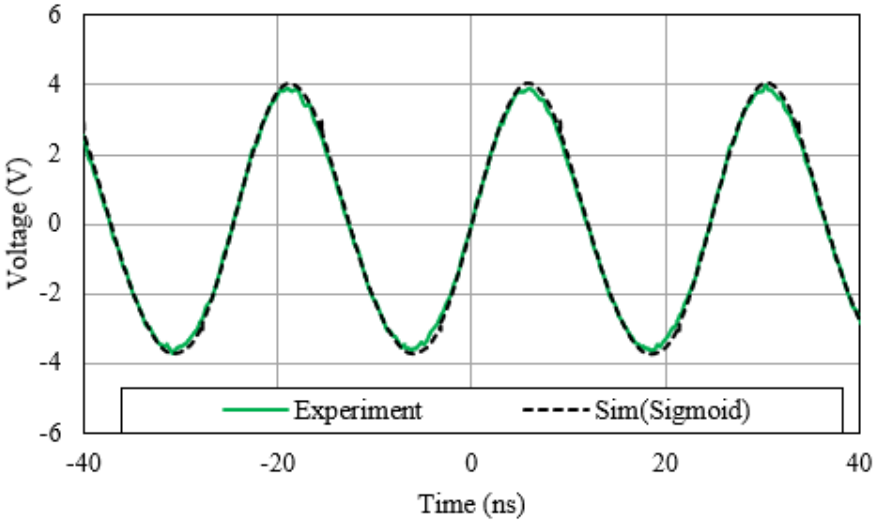

(b) Output voltage.

Figure 5.8 Experimental, simulated and calculated time response in 40.68 MHz class-E amplifier with considering c_L and R_L.

Simulation with abrupt junction model in Fig. 5.7(a) and Fig. 5.7(b) converge. However, the simulated drain-source voltage with abrupt junction model in Fig. 5.7(a) is not in a periodic steady state for switching frequency. The voltage at turn-on differs by the cycle. The calculated charge in abrupt junction model capacitance is not accurate. The shortage of accuracy in the off period is considered to cause the voltage hunting in simulation.

Simulation with the abrupt junction model in Fig. 5.8(a) and Fig. 5.8(b) do not converge. However, the accuracy of simulation with the abrupt junction model is impractical for GaN HEMT considered in this study. Drain-source voltages of Experiment and Sim(Sigmoid) in Fig. 5.7(a) and Fig. 5.7(b) coincide in the case that c_L and R_L are considered in the simulation. The effect of c_L and R_L on drain-source voltage in the off period is not significant because the drain-source voltage is determined by the charge of C_e and C_o shown in Eq. 5.6. The class-E switching condition is obtainable by the analysis in Sect. 5.3.

The simulated results of output voltage with the sigmoid function model in Fig. 5.7(b) and Fig. 5.8(b) are similar to experimental results compared to Fig. 5.5(b) and Fig. 5.6(b). The positive peak voltage of the Experiment is 8.3% lower than Sim(Sigmoid) and Calculated in Fig. 5.7(a). The difference of peak voltage in Fig. 5.8(b) is 3.2%. Output voltage with abrupt junction model is also similar to experimental output voltage. However, the simulated output voltage with the abrupt junction model varies cycle by cycle. The simulated output voltage with the abrupt junction model is not in a periodic steady state even in the case that the simulation result is obtained.

Output current i flows through a series resonant circuit composed with C_t, L_t and L_x. Parasitic components in series resonant circuit affect output current i and output voltage V_o. Circuit simulation with sigmoid function, c_L, and R_L coincide with experiment results. The consideration of c_L and R_L improves the accuracy of output voltage.

5.6 Summary

This chapter presented the circuit analysis and design of a class-E amplifier with the sigmoid function output capacitance model. The circuit analysis and designs were verified by simulation and experiment for class-E amplifiers. The conventional abrupt junction output capacitance model was not suitable for some lateral type GaN power device. The proposed model and analysis enabled circuit design of class-E amplifiers taking the nonlinear characteristics of GaN power devices into account. The characteristics of GaN power device need to be considered to design class-E amplifiers, then

the proposed methodology is useful.

The output voltage could be accurately simulated with consideration of parasitic components in inductors. In this chapter, since the main focus was on modeling the output capacitance of GaN, air-core inductors was used. However, as discussed in Chapter 3, practical power conversion circuits require inductors using magnetic materials. The circuits used in this chapter are expected to be miniaturized by using magnetic components.

Chapter 6

Conclusions

6.1 Conclusions

In this thesis, technologies for high frequency power conversion circuits using gallium compound semiconductor devices were developed. Each technology is necessary for miniaturization of power conversion circuit development. This chapter concludes the results obtained in this thesis.

This thesis described the structure of gallium compound power semiconductor devices. GaN HEMTs utilize two-dimensional electron gas to improve the trade-off between fast switching, low resistance, and high breakdown voltage. This structure contributes to the realization of power conversion circuits with high-frequency operation above 10 MHz. However, it is difficult to realize GaN diode with good characteristics. Ga_2O_3 is expected as alternative material for power devices as diodes. Ga_2O_3 not only has wider bandgap than GaN, but is also easier to mass produce. In addition, the trench-type SBD structure greatly improves reverse blocking characteristics. Gallium compound power semiconductor devices are expected to increase the operating frequency of power conversion circuits and to make the circuits smaller.

This thesis evaluated the magnetic properties of magnetic components for high-frequency power conversion using a 2-port circuit model. This thesis explained that conventional B-H analyzers had difficulty in characterizing magnetic components in the frequency range above 10 MHz. Based on 2-port measurement with a vector network analyzer, this thesis proposed a method to evaluate the magnetic properties of high-

frequency magnetic components. The circuit models of inductor were devised based on 2-port equivalent circuit models. Circuit simulations of class-E power amplifiers based on the inductor model accurately coincided with the drain-source voltage in actual circuits. The proposed magnetic component model simulated the behavior of the class-E switching operations at 10 MHz. However, it was found necessary to simulate the characteristics of power semiconductor devices to simulate the output voltage and current.

This thesis evaluated the thermal properties of gallium compound power semiconductor devices. Ga_2O_3 semiconductor devices have lower thermal conductivity than Si and GaN. Nevertheless, Ga_2O_3 is still in the development stage, and the ideality of the devices had not been certified. From the static characteristics of β-Ga_2O_3, this thesis confirmed that the ideality of the Schottky junction of SBDs can be used for the evaluation of transient thermal characteristics. This thesis evaluated the transient thermal characteristics of planar and trench type β-Ga_2O_3 SBDs using the static method. The measured transient thermal resistance was high compared to commercially available SiC, and the transient thermal resistance needs to be reduced for realization of high power density in power converters.

This thesis attempted to reduce the thermal resistance of β-Ga_2O_3 SBDs by grinding the substrate layer. This thesis fabricated two SBDs with substrate layer thicknesses of 250um and 100um. The thermal resistance from the junction to the drift layer was identified to be 3.1 K/W from the comparison of thermal resistances in two β-Ga_2O_3 SBDs. The $R_{th(j-c)}$ in thinned β-Ga_2O_3 SBD was higher than that in SiC SBD with the same size. This result indicated that thinning the β-Ga_2O_3 SBD was not sufficient to reduce the thermal resistance.

The class-E amplifiers fabricated in Chapter 3 did not take the output capacitance of the power semiconductor device into account. This thesis utilized a sigmoid function to model the voltage dependency of the output capacitance of GaN power semiconductor devices. The analysis for the circuit of a class-E amplifier using the sigmoid function to derive the class-E switching conditions was presented in this thesis. The soft-switching conditions using the sigmoid function were verified by simulation and experiment. Furthermore, it was shown that each voltage time response of the class-E

amplifier can be accurately simulated by applying the equivalent circuit model of the inductor and the sigmoid function model.

The technology developed in this thesis enabled the design and evaluation of high-frequency power conversion circuits above 10 MHz using gallium compound power semiconductor devices. In this thesis, class-E power amplifiers were used as the high-frequency power conversion circuit. The model used in this thesis can be applied to power conversion circuits other than class-E power amplifiers. This thesis will help the analysis of power conversion circuits using GaN power semiconductor devices.

β-Ga_2O_3 SBDs were only evaluated for device characteristics. β-Ga_2O_3 power semiconductors are still in the development stage. β-Ga_2O_3 power semiconductor devices used in this thesis could be evaluated for static electrical and thermal characteristics. However, they had not reached the stage where they are implemented and operated in high-frequency power conversion circuits. Further reduction of thermal resistance was required for practical use in power conversion circuits.

6.2 Industrial impacts

This thesis treated the magnetic components and gallium compound power semiconductor devices to develop the miniaturization technologies. At present, AC-DC converters using GaN power semiconductor devices are commercially available, and their use is expanding. Ga_2O_3 power semiconductor devices are being attempted to be implemented in society as components of power factor correction circuits.

The technology developed in this thesis would be a driver to advance the social implementation of gallium compound power semiconductor devices. GaN power semiconductor devices are considered to be used in power conversion circuits for RF power transmission. RF power converters often use the ISM band such as 13.56 MHz. It is industrially important to have an evaluation method for magnetic components that can be used in this frequency band. Commercially available power conversion circuits must comply with noise regulations such as CISPR standards. Radiated magnetic fields can be a problem for air-core magnetic components. For this reason, there are great demands for magnetic components with magnetic cores in power conversion circuits as

industrial products. This thesis can contribute to the expansion of the application of high-frequency power conversion circuits.

This thesis showed the transient thermal characteristics evaluation of β-Ga_2O_3 power semiconductor devices. The ideality of β-Ga_2O_3 SBDs was evaluated by their temperature dependency of electrical characteristics. β-Ga_2O_3 power semiconductor devices are expected to be the next generation power semiconductor devices. In this thesis, the current problems are clarified through the evaluation of transient thermal characteristics. There is a limit to the reduction of thermal resistance of Ga_2O_3 power semiconductor devices by thinning. This suggests that improvement of crystal quality and enlargement of die size are more important for the practical application of Ga_2O_3 power semiconductor devices. This indicates a principle for future research on Ga_2O_3 power semiconductor devices.

In this thesis, the voltage dependency modeling of the output capacitance for GaN power semiconductor devices was performed using the sigmoid function. The study explained that circuit analysis using sigmoid functions was possible and simulated circuit operation accurately. The device models provided by GaN power semiconductor device manufacturers were experimental equations with many parameters. The sigmoid function model used in this thesis could express the voltage dependency of output capacitance with only four parameters. Therefore, it has the potential to realize simpler and faster simulations than presently used device models. In this thesis, the circuit analysis of class-E amplifier based on circuit equations was conducted. It is expected to be applied to the design of RF power converters such as wireless power transmission circuits. It is expected that the application of the sigmoid function model will promote front loading during circuit design.

6.3 Future prospects

Operating frequency of power conversion circuits using GaN power semiconductor devices will increase further in the future. The output capacitance of the GaN HEMT used in this thesis is less than 20 pF. The capacitance and inductance mounted in the converters are low. In this case, not only the voltage dependency of the output

capacitance, but also the parasitic component of the circuit board has significant effects on the circuit operation. It is necessary to model the parasitic components of the circuit boards and to design circuits that take the parasitic components into account. In addition, as the operating frequency becomes higher, the bandwidth and resolution of measuring instruments such as current sensor become insufficient. The frequency characteristics of probes and fixtures affect the measurement results. In the case of evaluating power conversion circuits for gallium compound power semiconductor devices with low capacitance, measurement techniques are essential.

Ga_2O_3 power semiconductor devices are expected to be put to practical use in the future. The β-Ga_2O_3 power SBDs used in this thesis have an aluminum plated anode and are electrically connected by wire-bonding. The evaluation in this thesis revealed that the thermal resistance of the substrate layer of the SBD is high. Therefore, it is considered that the reduction of thermal resistance by flip mounting is effective. Since the SBD junction is in the epilayer, flip mounting can shorten the distance from the junction to the die-attach. However, it is difficult to connect transistors in flip mounting. For Ga_2O_3 power semiconductor devices to become commercially viable in the future, crystal quality must be improved and die area must be increased. In addition to this, improvements in crystal growth process technology is important. Larger areas can reduce thermal resistance and increase current capacity. Improving the characteristics of the Ga_2O_3 power semiconductor devices will pave the way to practical applications.

The study in this thesis is still confined to the technologies for miniaturization. It does not go as far as designing circuits by combined models of magnetic components, heat dissipation, and capacitance model. In power conversion circuits, there is a trade-off between miniaturization, reduction of heat dissipation, and magnetic component losses. Combined analysis of the trade-off using the models in this study is a future work. Comprehensive design will enable the design of highly efficient and compact power conversion circuits.

References

[1] T. Mishima: “Fundamentals and Core Technologies Surrounding High-Frequency Switch-Mode Power Converters (General Review),” The Journal of The Institution of Electrical Engineering of Japan, Vol.143, No.1, pp.9-12 (2023) in Japanese.

[2] T. Yatabe: “Advancement of Demand-Side Initiatives toward Carbon Neutrality -Promotion of Electrification and Hydrogen Utilization-,” The Journal of The Institution of Electrical Engineering of Japan, Vol.142, No.5, pp.264-267 (2022) in Japanese.

[3] K. Akimoto: “Model Analysis of Scenarios for Achieving Carbon Neutrality in Japan by 2050,” The Journal of The Institution of Electrical Engineering of Japan, Vol.143, No.2, pp.71-74 (2023) in Japanese.

[4] Y.Yoshida, M. Kimura, and N. Kurita: “Development Trends in Highly Efficient Energy Conversion Technologies,” The Journal of The Institution of Electrical Engineering of Japan, Vol.143, No.11, pp.706-709 (2023) in Japanese.

[5] M. H. Rashid: Power Electronics: Circuits, Devices, and Application, Fourth edition, PEARSON Education (2014).

[6] R W. Erickson and D Maksimovic: Fundamentals of Power Electronics, Third edition, Springer (2020).

[7] K. Hiratchi: “Circuit Technologies Supporting Diversification of Power Conversion Processes,” The Journal of The Institution of Electrical Engineering of Japan, Vol.143, No.1, pp.13-16 (2023) in Japanese.

[8] S. Ikeda: “Resonant Power Conversion Circuit that Contributes to Higher Frequency Power Converters,” The Journal of The Institution of Electrical Engineering of Japan, Vol.143, No.1, pp.17-20 (2023) in Japanese.

[9] M. Bhatnagar and B. J. Baliga: “Comparison of 6H-SiC, 3C-SiC, and Si for power devices,” IEEE Transactions on Electron Devices, Vol.40, No.3, pp.645-655 (1993).

[10] E. A. Jones, F. F. Wang, and D. Costinett: “Review of Commercial GaN Power Devices and GaN-Based Converter Design Challenges,” IEEE Journal of Emerging and Selected Topics in Power Electronics, Vol.4, No.3, pp.707-719 (2016).

[11] S. M. Sze, Yiming Li and Kwok K. Ng: Physics of Semiconductor Devices, fourth edition, Wiley (2021).

[12] X. Ding, Y. Zhou, and J. Cheng: “A review of gallium nitride power device and its applications in motor drive,” CES Transactions on Electrical Machines and Systems, Vol.3, No.1, pp.54-64 (2019).

[13] K. Shiojima, *et al.*: “Mapping the interfacial reaction of α-Ga_2O_3 Schottky contacts through scanning internal photoemission microscopy,” Thin Solid Films Vol.685, pp.17-25 (2019).

[14] E. Ahmadi, and Y. Oshima: “Materials issues and devices of α- and β-Ga_2O_3,” Journal of Applied Physics, Vol.126, No.16, 160901 (2019).

[15] M. Higshiwaki, *et al.*: “Crystal Growth and Device Application of Gallium Oxide(Ga_2O_3),” Journal of the Surface Science Society of Japan, Vol.35, No.2, pp.102-107 (2014).

[16] M. Mohamed, *et al.*: “Schottky barrier height of Au on the transparent semiconducting oxide β-Ga_2O_3,” Applied Physics Letters, Vol.101, No.13, 132106 (2012).

[17] T. C. Lovejoy, *et al.*: “Band bending and surface defects in α-Ga_2O_3,” Applied Physics Letters, Vol.100, No.18, 181602 (2012).

[18] J. Yang, *et al.*: “High Breakdown Voltage (− 201) β-Ga_2O_3 Schottky Rectifiers,” IEEE Electron Device Letters, Vol.38, No.7, pp.906-909 (2017).

[19] E. G. Víllora, *et al.*: "Electrical conductivity and lattice expansion of β-Ga_2O_3 below room temperature," Applied Physics Letters, Vol.92, No.20, 202118 (2008).

[20] Z. Guo, *et al.*: "Anisotropic thermal conductivity in single crystal β-gallium oxide," Applied Physics Letters, Vol.106, No.11, 111909 (2015).

[21] M. D. Santia, *et al.*: "Lattice thermal conductivity in β-Ga_2O_3 from first principles," Applied Physics Letters, Vol.107, No.4, 041907 (2015).

[22] R. P. Joshi: "Analysis of the temperature dependent thermal conductivity of silicon carbide for high temperature applications," Journal of Applied Physics, Vol.88, No.1, pp.265ˆˆe2ˆˆ80ˆˆ93269 (2000).

[23] R. Wei, *et al.*: "Thermal conductivity of 4H-SiC single crystals," Journal of Applied Physics, Vol.113, No.5, 053503 (2013).

[24] P.D. Maycock: "Thermal conductivity of silicon, germanium, Ⅲ-V compounds and Ⅲ-V alloys," Solid-State Electronics, Vol.10, No.3, (1967).

[25] K. Irmscher, Z. Galazka, M. Pietsch, R. Uecker, and R. Fornari: "Electrical properties of β-Ga_2O_3 single crystals grown by the Czochralski method," Journal of Applied Physics, Vol.110, No.6, 63720 (2011).

[26] M. Higashiwaki, K. Sasaki, A. Kuramata, T. Masui, and S. Yamakoshi: "Gallium oxide (β-Ga_2O_3) metal-semiconductor field-effect transistors on single-crystal β-Ga_2O_3 (010) substrates," Journal of Applied Physics, Vol.100, No.1, 013504 (2012).

[27] B. J. Baliga: Fundamentals of Power Semiconductor Devices, Springer Science+Business Media (2008).

[28] K. Sato, H. Kato, T. Fukushima: "Technical Report: Development of Drive System for Shinkansen Train N700S," IEEJ Transaction on Industrial Application, Vol.140, No.8, p.8 (2020) in Japanese.

[29] K. Sato, H. Kato, T. Fukushima: “Development of SiC Applied Traction System for Next-Generation Shinkansen High-Speed Trains,” IEEJ Transaction on Industrial Application, Vol.9, No.4, pp.453-459 (2020).

[30] R. Sun, J. Lai, W. Chen, and B. Zhang: “GaN Power Integration for High Frequency and High Efficiency Power Applications: A Review,” IEEE Access, Vol.8, pp.15529-15542 (2020).

[31] T. Nagashima, *et al.*: “Analytical design procedure for resonant inductively coupled wireless power transfer system with class-E2 DC-DC converter,” 2014 IEEE International Symposium on Circuits and Systems, pp.113-116, Melbourne, VIC, Australia (2014).

[32] Y. -X. Ling and T. -H. Tsai: “A 6.78MHz Wireless Power Transfer System with Maximum Power Tracking over Wide Load Range,” 2021 International Symposium on VLSI Design, Automation and Test, pp.1-4, Hsinchu, Taiwan (2021).

[33] E. Chung and J. -I. Ha: “Impedance Matching Network Design for 6.78MHz Wireless Power Transfer System With Constant Power Characteristics Against Misalignment,” IEEE Transactions on Power Electronics, Vol.39, No.1, pp.1788-1801 (2024).

[34] H. Wen, Y. Liu, D. Jiao, C. -S. Yeh, and J. -S. Lai: “Design Principles and Optimization Considerations of a High Frequency Transformer in GaN Based 1 MHz 2.8 kW LLC Resonant Converter with over 99% Efficiency,” 2021 IEEE Applied Power Electronics Conference and Exposition (APEC), Phoenix, AZ, USA, pp.1939-1944 (2021).

[35] S. Ujita, *et al.*: “Highly-Efficient MHz-class Operation of Boost DC-DC Converters by Using GaN Transistors on GaN with Reduced RonQoss,” PCIM Europe 2019; International Exhibition and Conference for Power Electronics, Intelligent Motion, Renewable Energy and Energy Management, Nuremberg, Germany, pp.1-6 (2019).

[36] A. Hariya, *et al.*: “Influence of parasitic components on MHz-level frequency LLC resonant DC-DC converter,” IECON 2015 - 41st Annual Conference of the IEEE

Industrial Electronics Society, Yokohama, Japan, pp.4842-4847 (2015).

[37] A. Hariya, *et al.*: "Reduction technique of leakage flux effects on GaN-HEMTs in 5 MHz / 100 W isolated DC-DC converters," 2016 IEEE Applied Power Electronics Conference and Exposition (APEC), Long Beach, CA, USA, pp.2430-2436 (2016).

[38] Y. Yanagisawa, Y. Miura, H. Handa, T. Ueda and T. Ise: "Characteristics of Isolated DC-DC Converter With Class Phi-2 Inverter Under Various Load Conditions," IEEE Transactions on Power Electronics, Vol.34, No.11, pp.10887-10897 (2019).

[39] L. Shi, J. C. Rodriguez, M. J. Carrizosa and P. Alou: "ZVS Tank Optimization for Class-D Amplifiers in High Frequency WPT Applications," 2021 IEEE Applied Power Electronics Conference and Exposition (APEC), Phoenix, AZ, USA, pp.1593-1598 (2021).

[40] M. Okamoto, *et al.*: "13.56-MHz Class-E RF power amplifier using normally-on GaN HEMT," IECON 2014 - 40th Annual Conference of the IEEE Industrial Electronics Society, pp.982-987 (2014)

[41] Y. Zhang, M. Rodriguez and D. Maksimovic: "Very High Frequency PWM Buck Converters Using Monolithic GaN Half-Bridge Power Stages With Integrated Gate Drivers," IEEE Transactions on Power Electronics, Vol.31, No.11, pp.7926-7942 (2016).

[42] W. S. . -C. Li, *et al.*: "Dynamic Rdson and Vth Free 15 V E-mode GaN HEMT Delivering Low sFOM of 13.1 m Ω ·nC and over 90% Efficiency at 10 MHz for Buck Converter," 2022 IEEE 34th International Symposium on Power Semiconductor Devices and ICs (ISPSD), Vancouver, BC, Canada, pp.161-164 (2022).

[43] M. Higashiwaki, *et al.*: "Current Status of Gallium Oxide-Based Power Device Technology," 2015 IEEE Compound Semiconductor Integrated Circuit Symposium, pp.17-25 (2015).

[44] Z. Hu *et al.*: "Enhancement-Mode Ga2O3 Vertical Transistors With Breakdown Voltage >1 kV," IEEE Electron Device Letters, Vol.39, No.6, pp.869-872 (2018).

[45] J. Yang, *et al.*: "Vertical Geometry, 2-A Forward Current Ga_2O_3 Schottky Rectifiers on Bulk Ga_2O_3 Substrates," IEEE Transactions on Electron Devices, Vol.65, No.7, pp.2790-2796 (2018).

[46] N. Allen, *et al.*: "Vertical Ga_2O_3 Schottky Barrier Diodes With Small-Angle Beveled Field Plates: A Baliga's Figure-of-Merit of 0.6 GW/cm^2," IEEE Electron Device Letters, Vol.40, No.9, pp.1399-1402 (2019).

[47] A. Kuramata, *et al.*: "Optical and Electrical Device Application of Gallium Oxide Single Crystal," The Japanese Association for Crystal Growth, Vol.42, No.2, pp.130-140 (2015).

[48] J. D. Blevins, *et al.*: "Development of Large Diameter Semi-Insulating Gallium Oxide (Ga_2O_3) Substrates," IEEE Transactions on Semiconductor Manufacturing, Vol.32, No.4, pp.466-427 (2019).

[49] K. Sasaki, *et al.*: "Ga_2O_3 Schottky Barrier Diodes Fabricated by Using Single-Crystal β-Ga_2O_3 (010) Substrates," IEEE Electron Device Letters, Vol.34, No.4, pp.493-495 (2013).

[50] G. H. Jessen: "The Supercharged Semiconductor: Gallium oxide could make powerful radios and switch thousands of volts," IEEE Spectrum, Vol.58, No.4, pp.36-42 (2021).

[51] M. Higashiwaki: "Beta Gallium Oxide Devices," Applied Physics Express, Vol.90, No.5, pp.283-289 (2021) in Japanese.

[52] M. H. Wong, K. Goto, H. Murakami, Y. Kumagai, and M. Higashiwaki: "Current Aperture Vertical β-Ga_2O_3 MOSFETs Fabricated by N- and Si-Ion Implantation Doping," IEEE Electron Device Letters, Vol.40, No.3, pp.431-434 (2019).

[53] C. R. Sullivan, W. Li, S. Prabhakaran, and S. Lu: "Design and Fabrication of Low-Loss Toroidal Air-Core Inductors," 2007 IEEE Power Electronics Specialists Conference, pp.1754-1759 (2007).

[54] G. Zulauf, *et al.*: "A unified model for high-power, air-core toroidal PCB inductors," 2017 IEEE 18th Workshop on Control and Modeling for Power Electronics (COMPEL), pp.1-8 (2017).

[55] K. W. E. Cheng, *et al.*: "Leakage field modeling of spiral winding transformer for contactless power converters," 2006 12th Biennial IEEE Conference on Electromagnetic Field Computation, pp.324-324 (2006).

[56] T. Ide, *et al.*: "Nd x Fe1-x N y Magnetic Core Application for Resonance Coil of 13.56 MHz GaN Wireless Power Transmission," IEEE Transactions on Magnetics, Vol.55, No.10, pp.1-5 (2019).

[57] T. Fukuoka, *et al.*: "An 86% Efficiency, 20MHz, 3D-Integrated Buck Converter with Magnetic Core Inductor Embedded in Interposer Fabricated by Epoxy/Magnetic-Filler Composite Build-Up Sheet," 2019 IEEE Applied Power Electronics Conference and Exposition (APEC), pp.1561-1566 (2019).

[58] D. J. Nicol: "Plain and simple design details regarding the application of iron powder cores," Electrical Insulation Conference and Electrical Manufacturing and Coil Winding Conference, pp.241-247 (1999).

[59] Y. Sugawa, *et al.*: "Carbonyl-Iron/Epoxy Composite Magnetic Core for Planar Power Inductor Used in Package-Level Power Grid," IEEE IEEE Transactions on Magnetics, Vol.49, No.7, pp.4172-4175 (2013).

[60] M. Sonehara, *et al.*: "Characterization of UHF Band LC Filter With RF Spiral Inductor Using Carbonyl-Iron Powder/Epoxy Composite Magnetic and Chip Capacitor," IEEE Transactions on Magnetics, Vol.53, No.11, pp.1-5 (2017).

[61] K. Sato, *et al.*: "Fabrication of metal composite magnetic core transformer with surface-oxidized carbonyl-iron powder and its application to the flyback-type dc-dc converter," Transaction of the Magnetics Society of Japan (Special Issues), Vol.1, No.1, pp.44-52 (2017) in Japanese.

[62] D. L. Faircloth, *et al.*: "Complex permittivity and permeability extraction for

multilayered samples using S-parameter waveguide measurements," IEEE Transactions on Microwave Theory and Techniques, Vol.54, No.3, pp.1201-1209 (2006).

[63] S. Yamaguchi: "Estimation of thermal resistance of β-Ga_2O_3 Schottky barrier diode packages fabricated by flip chip bonding technique," The 67th JSAP Spring Meetng, D419-12, (2020) in Japanese.

[64] F. Raab: "Class-F power amplifiers with maximally flat waveforms," IEEE Transactions on Microwave Theory and Techniques, Vol.45, No.11, pp.2007-2012 (1997).

[65] R.-L. Lin and F.-Y. Chen: "Self-oscillating push-pull class-E/F converters", The 2004 IEEE Asia-Pacific Conference on Circuits and Systems, Vol.2, pp.649-652 (2004).

[66] J. M. Rivas, *et al.*: "A Very High Frequency DC-DC Converter Based on a Class Φ2 Resonant Inverter," IEEE Transactions on Power Electronics, Vol.26, No.10, pp.2980-2992 (2011).

[67] A. Clements, V. Vishnoi, S. Dehghani and T. Johnson: "A Comparison of GaN Class E Inverter and Synchronous Rectifier Designs for 13.56 MHz, 27.12 MHz and 40.68 MHz ISM Bands," 2018 IEEE Wireless Power Transfer Conference (WPTC), pp.1-4, Montreal, QC, Canada (2018).

[68] W. Saito, *et al.*: "Demonstration of 13.56-MHz class-E amplifier using a high-Voltage GaN power-HEMT," IEEE Electron Device Letters, Vol.27, No.5, pp.326-328 (2006).

[69] N. O. Sokal and A. D. Sokal: "Class E-A new class of high-efficiency tuned single-ended switching power amplifiers," IEEE Journal of Solid-State Circuits, Vol.10, No.3, pp.168-176 (1975).

[70] N. O. Sokal: "Class-E RF power amplifiers," QEX, No.204, pp.9-20, Jan./Feb (2001).

[71] M. Albulet: RF Power Amplifiers, SciTech Publishing (2001).

[72] F. Raab: “Idealized operation of the class E tuned power amplifier,” IEEE Transactions on Circuits and Systems, Vol.24, No.12, pp.725-735 (1977).

[73] M. K. Kazimierczuk: RF Power Amplifiers, wiley (2008).

[74] T. Suetsugu and M. K. Kazimierczuk: “Comparison of class-E amplifier with nonlinear and linear shunt capacitance,” IEEE Transactions on Circuits and Systems I: Fundamental Theory and Applications, Vol.50, No.8, pp.1089-1097 (2003).

[75] Tadashi Suetsugu, Xiuqin Wei, Marian K. Kazimierczuk: “Analysis of Power Loss of Class E Amplifier with Nonlinear Shunt Capacitance,” IEEJ Journal of Industry Applications, Vol.3, No.1, pp.68-74 (2014).

[76] M. Hayati, A. Lotfi, M. K. Kazimierczuk and H. Sekiya: “Analysis and Design of Class-E Power Amplifier With MOSFET Parasitic Linear and Nonlinear Capacitances at Any Duty Ratio,” IEEE Transactions on Power Electronics, Vol.28, No.11, pp.5222-5232 (2013).

[77] T. Suetsugu and M. K. Kazimierczuk: “Analysis and design of class E amplifier with shunt capacitance composed of nonlinear and linear capacitances,” IEEE Transactions on Circuits and Systems I: Regular Papers, Vol.51, No.7, pp.1261-1268 (2004).

[78] H. Sekiya, T. Watanabe, T. Suetsugu and M. K. Kazimierczuk: “Analysis and Design of Class DE Amplifier with Nonlinear Shunt Capacitance,” 7th International Conference on Power Electronics and Drive Systems, pp.937-942, Bangkok, Thailand (2007).

[79] H. Sekiya, R. Miyahara and M. K. Kazimierczuk: “Design of class-DE amplifier with linear and nonlinear shunt capacitances for 25 % duty ratio,” 2009 IEEE International Symposium on Circuits and Systems, pp.2870-2873, Taipei, Taiwan (2009).

[80] X. Cheng, M. Li and Y. Wang: “Physics-Based Compact Model for AlGaN/GaN MODFETs With Close-Formed I-V and C-V Characteristics,” IEEE Transactions on Electron Devices, Vol.56, No.12, pp.2881-2887 (2009).

[81] S. Khandelwal, Y. S. Chauhan and T. A. Fjeldly: "Analytical Modeling of Surface-Potential and Intrinsic Charges in AlGaN/GaN HEMT Devices," IEEE Transactions on Electron Devices, Vol.59, No.10, pp.2856-2860 (2012).

[82] J. P. Kozak *et al.*: "An Analytical Model for Predicting Turn-ON Overshoot in Normally-OFF GaN HEMTs," IEEE Journal of Emerging and Selected Topics in Power Electronics, Vol.8, No.1, pp.99-110 (2020).

[83] L. Dunleavy, C. Baylis, W. Curtice and R. Connick: "Modeling GaN: Powerful but Challenging," IEEE Microwave Magazine, Vol.11, No.6, pp.82-96 (2010).

[84] C. Hamaguchi, N. Mori: Electronic Properties -The Fundamental of electronic devices, Asakura Publishing (2014) in Japanese.

[85] H. Matsunami, M. Yoshimoto: Semiconductor Devices, Kyoritsu Publishing (2000) in Japanese.

[86] T. Ueda, *et al.*: "Polarization Engineering in GaN Power Devices," Journal of the Vacuum Society of Japan, Vol.54, No.6, pp.393-397 (2011).

[87] N. M. Shrestha, Y. Li, T. Suemitsu, and S. Samukawa: "Electrical Characteristic of AlGaN/GaN High-Electron-Mobility Transistors With Recess Gate Structure," IEEE Transactions on Electron Devices, Vol.66, No.4, pp.1694-1698 (2019).

[88] R. Wang *et al.*: "Gate-Recessed Enhancement-Mode InAlN/AlN/GaN HEMTs With 1.9-A/mm Drain Current Density and 800-mS/mm Transconductance," IEEE Electron Device Letters, Vol.31, No.12, pp.1383-1385 (2010).

[89] D. Qiao, L. S. Yu, and S. S. Lau: "Dependence of Ni/AlGaN Schottky barrier height on Al mole fraction," Journal of Applied Physics, Vol.87, No.2, 801 (2000).

[90] R. T. Tung: "The physics and chemistry of the Schottky barrier height," Applied Physics Reviews, Vol.1, No.1, 011304 (2014).

[91] M. D. Heinemann: "Oxygen deficiency and Sn doping of amorphous Ga_2O_3," Applied Physics Letters, Vol.108, No.2, 022107 (2016).

[92] S. Mahato *et al.*: "Analysis of temperature dependent current-voltage and capacitance-voltage characteristics of an Au/V_2O_5/n-Si Schottky diode," AIP Advanced, Vol.7, No.8, 085313 (2017).

[93] I. Jyothi *et al.*: "Temperature Dependency of Schottky Barrier Parameters of Ti Schottky Contacts to Si-on-Insulator," Material transactions, Vol.54, No.9, pp.1655-1660 (2013).

[94] T. Funaki *et al.*: "High temperature switching operation of a power diamond Schottky barrier diode," IEICE Electronics Express, Vol.9, No.24, pp.1835-1841 (2012).

[95] T. Funaki *et al.*: "High-temperature characteristics of SiC Schottky barrier diodes related to physical phenomena," IEICE Electronics Express, Vol.5, No.6, pp.198-203 (2008).

[96] V. Khemka, V. Ananthan and T. P. Chow: "A fully planarized 4H-SiC trench MOS barrier Schottky (TMBS) rectifier," IEEE Electron Device Letters, Vol.21, No.6, pp.286-288 (2000).

[97] M. Mehrotra and B. J. Baliga: "Trench MOS Barrier Schottky (TMBS) rectifier: A Schottky rectifier with higher than parallel plane breakdown voltage," Solid-State Electronics, Vol.38, No.4, pp.801-806 (1995).

[98] K. Sasaki *et al.*: "First Demonstration of Ga_2O_3 Trench MOS-Type Schottky Barrier Diodes," IEEE Electron Device Letters, Vol.38, No.6, pp.783-785 (2017).

[99] N. O. Sokal and F. H. Raab: "Harmonic output of class-E RF power amplifiers and load coupling network design," IEEE Journal of Solid-State Circuits, Vol.12, No.1, pp.86-88 (1977).

[100] K. Sugimura *et al.*: "Novel Method for Making Surface Insulation Layer on Fe-Based Amorphous Alloy Powder by Surface-Modification Using Two-Step Acid Solution Processing," IEEE Transactions on Magnetics, Vol.54, No.11, pp.1-5 (2018).

[101] W.G. Hurley and W.H. Wölfle: Transformers and Inductors for Power Electronics: Theory, Design and Applications, WILEY (2013).

[102] P. Poulichet, F. Costa and E. Laboure: “High-frequency modeling of a current transformer by finite-element simulation,” IEEE Transactions on Magnetics, Vol.39, No.2, pp.998-1007 (2003).

[103] W. Luo, *et al.*: “Design of Load-Independent Class-E Inverter with MOSFET Parasitic Capacitances,” 2019 IEEE 62nd International Midwest Symposium on Circuits and Systems (MWSCAS), pp.529-532 (2019).

[104] X. Wei, *et al.*: “Design of Class-E Amplifier With MOSFET Linear Gate-to-Drain and Nonlinear Drain-to-Source Capacitances,” IEEE Transactions on Circuits and Systems I (Regular Papers), Vol.58, No.10, pp.2556-2565 (2011).

[105] M. Albulet and R. E. Zulinski: “Effect of switch duty ratio on the performance of class E amplifiers and frequency multipliers,” IEEE Transactions on Circuits and Systems I: Fundamental Theory and Applications, Vol.45, No.4, pp.325-335 (1998).

[106] M. Kazimierczuk: “Effects of the collector current fall time on the class E tuned power amplifier,” IEEE Journal of Solid-State Circuits, Vol.18, No.2, pp.181-193 (1983).

[107] K. Shimura, T. Yamamoto, Y. Bu and T. Mizuno: “Examination of High- Q -Factor Conductor-Embedded Planar Transformer With Magnetic Flux-Path Control Technology,” IEEE Transactions on Magnetics, Vol.56, No.3, pp.1-4 (2020).

[108] K. Shimura, S. Kobayashi, M. Sato and T. Mizuno: “Improving Efficiency of Beyond-10 MHz LLC Resonant DC-DC Converters Using Spiral Transformers With Magnetic Flux Path Control Technology,” IEEE Transactions on Magnetics, Vol.57, No.11, pp.1-9 (2021).

[109] JEDEC51-14: “transient dual interface test method for the measurement of the thermal resistance junction-to-case of semiconductor devices with heat flow through a single path,” JEDEC (2010).

[110] V. Székelya: “Fine structure of heat flow path in semiconductor devices: A measurement and identification method,” Solid-State Electronics, Vol.31, No.9, pp.1363-1368 (1988).

[111] D. Schweitzer: “Transient Measurement of the Junction-To-Case Thermal Resistance Using Structure Functions: Chances and Limits,” 2008 Twenty-fourth Annual IEEE Semiconductor Thermal Measurement and Management Symposium, pp.191-197 (2008).

[112] H. L. Yeo and K. J. Tseng: “Modelling technique utilizing modified sigmoid functions for describing power transistor device capacitances applied on GaN HEMT and silicon MOSFET,” 2016 IEEE Applied Power Electronics Conference and Exposition (APEC), pp.3107-3114, Long Beach, CA, USA (2016).

[113] J. Dobusch, R. Schwanninger and T. Duerbaum: “Novel Approach to Model GaN-HEMT Capacitances using Sigmoid Functions,” Proceedings PCIM Europe digital days 2021; International Exhibition and Conference for Power Electronics, Intelligent Motion, Renewable Energy and Energy Management, pp.1-8, Online (2021).

[114] R. Baba, *et al.*: “Development of AlGaN/GaN FETs for power supply,” The transactions of the IEEJ. C, Vol.130, No.6, pp.924-928 (2010) in Japanese.

[115] C. Sun, Z. Niu and S. Yang: “Dynamic Gate Capacitance Model for Switching Transient Analysis in P-GaN Gate HEMTs,” 35th International Symposium on Power Semiconductor Devices and ICs, pp.135-138, Hong Kong (2023).

[116] S. Khandelwal *et al.*: “An Accurate Compact Model for GaN Power Switches with the Physics-based ASM-HEMT Model,” 2021 IEEE Applied Power Electronics Conference and Exposition (APEC), pp.2389-2392, Phoenix, AZ, USA (2021).

[117] D. Čučak *et al.*: “Physics-Based Analytical Model for Input, Output, and Reverse Capacitance of a GaN HEMT With the Field-Plate Structure,” IEEE Transactions on Power Electronics, Vol.32, No.3, pp.2189-2202 (2017).

[118] A. Abdulsalam, N. Karumuri and G. Dutta: "Modeling and Analysis of Normally-OFF p-GaN Gate AlGaN/GaN HEMT as an ON-Chip Capacitor," IEEE Transactions on Electron Devices, Vol.67, No.9, pp.3536-3540 (2020).

[119] Y. Liu, Q. Yu and J. Du: "Design Considerations of GaN GIT Devices for High Speed Power Switching Applications," 2019 IEEE 2nd International Conference on Electronics Technology (ICET), pp.339-344, Chengdu, China (2019).

[120] M. Kanamura, *et al.*: "A Normally-Off GaN HEMT with Large Drain Current," The transactions of the IEEJ. C, Vol.130, No.6, pp.929-933 (2010) in Japanese.

[121] D. D. Mahajan, S. A. Albahrani, R. Sodhi, T. Eguchi and S. Khandelwal: "Physics-Oriented Device Model for Packaged GaN Devices," IEEE Transactions on Power Electronics, Vol.35, No.6, pp.6332-6339 (2020).

[122] M. S. Nikoo, A. Jafari, N. Perera and E. Matioli: "Output Capacitance Losses in Wide-Band-Gap Transistors: A Small-Signal Modeling Approach," 2020 32nd International Symposium on Power Semiconductor Devices and ICs (ISPSD), pp.190-193, Vienna, Austria (2020).

Publications

[Published papers]

1. Shota Seki, Shuhei Fukunaga, Takaaki Ibuchi, and Tsuyoshi Funaki: "2-port Characterization and Modeling of Magnetic Components for 10 MHz Class-E Inverters Design," IEEJ Transactions on Fundamentals and Materials, Vol.141, No.5, Special Issue on Trends and Prospects on Practical Applications of High-Frequency Magnetic Materials, pp.317-326 (2021) in Japanese.

2. Shota Seki, Tsuyoshi Funaki, Jun Arima, Minoru Fujita, Jun Hirabayashi, and Kazuyoshi Hanabusa: "Transient thermal characterization of β-Ga_2O_3 Schottky barrier diodes," IEICE Electronics Express, Vol.19, No.6, pp.1-5 (2022).

3. Shota Seki and Tsuyoshi Funaki: "Analysis and Design of Class-E Amplifier with Nonlinear Output Capacitance Model Using Sigmoid Function for GaN HEMT," IEEJ Journal of Industry Applications, Vol.13, No.4, pp.437-444 (2024).

[International conference proceeding]

1. ◯ Shota Seki, Tsuyoshi Funaki, Jun Arima, Minoru Fujita, Jun Hirabayashi, and Kazuyoshi Hanabusa: "Evaluation of Thermal Resistance Reduction by Thinning Substrate of β-Ga_2O_3 SBD," 2023 International Conference on Electronics Packaging (ICEP2023), FD3-2, pp.193-194, Kumamoto, Japan (2023).

[Domestics conference proceedings]

1. Tsuyoshi Funaki, ◯ Shota Seki, and Shuhei Fukunaga: “A Study on High Frequency Operation of Power Conversion Circuit for Onboard Power Supply Miniaturization,” The papers of Joint Technical Meeting on Motor Drive/Rotating Machinery/Vehicle Technology, IEEJ, MD-19-85/RM-19-53/VT-19-13, Chiyoda-ward, Tokyo (2019) in Japanese.

2. ◯ Shota Seki, Tsuyoshi Funaki, and Shuhei Fukunaga: “An Experimental Study on Class-E2 Isolated DC-DC Converter with GaN GIT,” The papers of Domestic Conference, IEEJ, 4-053, Adachi-ward, Tokyo (2020) in Japanese.

3. ◯ Shota Seki and Tsuyoshi Funaki: “Fabrication and performance evaluation of 13.56MHz class E inverter with SiC MOSFET,” The papers of Domestic Conference, IEEJ, WEB18-A3, On-line (2021) in Japanese.

4. ◯ Shota Seki and Tsuyoshi Funaki: “An experimental study on isolated class-E_2 DC-DC converter with RF power transformer and GaN GIT,” The papers of Joint Technical Meeting on Power Engineering/Power Systems Engineering/Semiconductor Power Converter, IEEJ, PE-21-040,PSE-21-053,SPC-21-092, On-line (2021) in Japanese.

5. ◯ Shota Seki and Tsuyoshi Funaki: “An Experimental Study on 40MHz Class-E Inverter with GaN Transistor,” The papers of Domestic Conference, IEEJ, On-line (2022) in Japanese.

6. ◯ Shota Seki, Takaaki Ibuchi, and Tsuyoshi Funaki: “The Probing Influences on Measured Voltage in 50 MHz Driven Power Conversion Circuit,” The papers of Joint Technical Meeting on Semiconductor Power Converter/Motor Drive, IEEJ, SPC-22-168,MD-22-103, Tanegashima, Kagoshima (2022) in Japanese.

7. ◯ Shota Seki and Tsuyoshi Funaki: “A Study on Parasitic Inductance Reduction with 3D Mounted Capacitors in High Frequency Rectifier Circuit,” The papers of Domestic Conference, IEEJ, 4-119, Nagoya, Aichi (2023) in Japanese.

[Article]

1. Shota Seki: “Verification of the power semiconductors of new materials! Fabrication of 40kVA-class high-frequency inverter,” Tragi Jr., Vol.49, pp.26-28 (2022) in Japanese.

[Award]

1. IPEC2022 Student Poster Competition Excellent Presentation Award (2022).